THE PROCESSING OF POROUS Ni-RICH TiNi ALLOYS VIA POWDER
METALLURGY AND THEIR CHARACTERIZATION

A THESIS SUBMITTED TO
THE GRADUATE SCHOOL OF NATURAL AND APPLIED SCIENCES
OF
MIDDLE EAST TECHNICAL UNIVERSITY

BY

GÜL İPEK NAKAŞ

IN PARTIAL FULFILLMENT OF THE REQUIREMENTS
FOR
THE DEGREE OF DOCTOR OF PHILOSOPHY
IN
METALLURGICAL AND MATERIALS ENGINEERING

SEPTEMBER 2012

Approval of the thesis:

THE PROCESSING OF POROUS Ni-RICH TiNi ALLOYS VIA POWDER METALLURGY AND THEIR CHARACTERIZATION

submitted by **GÜL İPEK NAKAŞ** in partial fulfillment of the requirements for the degree of **Doctor of Philosophy in Metallurgical and Materials Engineering, Middle East Technical University** by,

Prof. Dr. Canan Özgen
Dean, Graduate School of **Natural and Applied Sciences**   _____

Prof. Dr. Hakan Gür
Head of Department, **Metallurgical and Materials Engineering**   _____

Prof. Dr. Şakir Bor
Supervisor, **Metallurgical and Materials Engineering, METU**   _____

Examining Committee Members

Prof. Dr. İbrahim Günal
Department of Physics, METU   _____

Prof. Dr. Şakir Bor
Metallurgical and Materials Engineering, METU   _____

Prof. Dr. Rıza Gürbüz
Metallurgical and Materials Engineering, METU   _____

Assoc. Prof. Dr. Nuri Durlu
Mechanical Engineering, TOBB ETU   _____

Assoc. Prof. Dr. Arcan Dericioğlu
Metallurgical and Materials Engineering, METU   _____

Date :   28.09.2012

I hereby declare that all information in this document has been obtained and presented in accordance with academic rules and ethical conduct. I also declare that, as required by these rules and conduct, I have fully cited and referenced all material and results that are not original to this work.

Name, Last name: Gül İpek Nakaş

Signature   :

ABSTRACT

THE PROCESSING OF POROUS Ni-RICH TiNi ALLOYS VIA POWDER METALLURGY AND THEIR CHARACTERIZATION

Nakaş, Gül İpek

Ph.D., Department of Metallurgical and Materials Engineering

Supervisor: Prof. Dr. Şakir Bor

In the scope of this study, TiNi foams with porosities in the range of 39-64 vol% were processed from prealloyed powders by Mg space holder technique. Porous TiNi alloys displayed homogeneously distributed spherical pores with interconnections, which is suitable for bone ingrowth.

Porous Ti-50.8 at%Ni alloys were processed by sintering at 1200 °C for 2 h to analyze the microstructure as well as mechanical behavior. SEM, TEM and XRD studies were conducted for the characterization of microstructure and phase analyses in addition to the mechanical characterization performed by monotonic and superelasticity compression tests as well as compressive fatigue tests. It was observed that stress required to trigger martensitic transformation was decreased via increasing porosity. The monotonic compression test results also indicated that altering the porosity content of TiNi foams leads to different monotonic compression behaviors. It was observed that the foams display more bulk deformation like behavior as a composite structure composed of TiNi and macropores when the porosity content was low. As the porosity content has increased, the struts became

more effective and deformation proceeds by the collapse of favorable struts. On the other hand, cyclic superelasticity tests results indicated that maximum achieved and recovered strain values at the end of fifth cycle increase while the fraction of strain recovered at the end of fifth cycle decreases with decreasing porosity content. Furthermore, the fatigue lives of the processed foams were observed to vary within a band which has a width decreasing with decreasing σ_{max} / σ_y yielding an endurance limit ranging in between 26-89 MPa or 0.5-0.6 σ_y. Fractography studies on the failed foams after fatigue testing revealed that the failure occurs by the coalescence of micro-cracks initiated from pore walls leading to macro-cracks aligned at 45° with respect to the loading axis.

In addition to the mentioned characterization studies, the effects of sintering temperature and time on TiNi foams with 58 vol% porosity as well as heat treatment on the microstructure and the mechanical behavior of TiNi foams with 49 vol% porosity were analyzed with SEM and compression tests. Aging of TiNi foams with 49 vol% porosity at 450 °C for 1.5 h has shown that the presence of Ti_3Ni_4 precipitates improve the superelastic response.

Keywords: Space Holder Technique, TiNi Foam, Compression, Superelasticity, Fatigue

ÖZ

GÖZENEKLİ NİKELCE ZENGİN TiNi ALAŞIMLARININ TOZ METALURJİ YÖNTEMİYLE ÜRETİLMESİ VE KARAKTERİZASYONU

Nakaş, Gül İpek

Doktora, Metalurji ve Malzeme Mühendisliği Bölümü

Tez Yöneticisi: Prof. Dr. Şakir Bor

Eylül 2012, 129 sayfa

Bu araştırma kapsamında, alaşımlanmış TiNi tozlardan Mg boşluk yapıcı kullanılarak hacimce %39-64 aralığında değişen gözenek oranına sahip TiNi köpükler üretilmiştir. Bu TiNi köpüklerin kemik büyümesine uygun, birbirleriyle bağlantılı ve homojen dağılımlı gözeneklere sahip olduğu görülmüştür.

1200 °C sıcaklıkta 2 saat sinterlenerek üretilen gözenekli Ti-50.8 at%Ni alaşımlarının mikroyapısal özellikleri ve mekanik davranışı incelenmiştir. İç yapı ve faz analizleri için yapılan SEM, TEM ve XRD incelemelerine ek olarak mekanik davranış analizi için basma testleri ve basma yönünde süperelastisite ve yorulma testleri yapılmıştır. Martensitik dönüşümü başlatmak için gereken gerilim değerinin artan gözenek oranı ile düştüğü gözlemlenmiştir. Basma testleri sonucunda değişen gözenek miktarının farklı basma davranışlarına sebep olduğu görülmüştür. Gözenek miktarı düşük olduğunda TiNi köpüklerin hacimli metallere benzer şekilde, TiNi ve makro gözeneklerden oluşan kompozit bir yapı gibi davrandığı gözlemlenmiştir. Gözenek miktarı arttığında ise sinterleme duvarlarının davranışının önem kazanması

sonucunda deformasyon uygun durumdaki sinterleme duvarlarının çökmesi yoluyla gerçekleşmiştir. Öte yandan, döngüsel süperleastisite testleri, beşinci döngü sonunda ulaşılan azami gerinim ve geri kazanılan gerinim değerlerinin azalan gözenek oranı ile arttığını, ancak beşinci döngü sonunda kazanılan gerinim oranının düştüğünü göstermiştir. Ayrıca, üretilen köpüklerin yorulma ömürlerinin, genişliği düşen σ_{max} / σ_y değerleri ile daralan bir bant aralığında değiştiği ve dayanma sınırlarının 26-89 MPa ya da 0,5-0,6 σ_y aralığında değiştiği görülmüştür. Yorulma testi sonucunda kırılan köpüklerde yapılan kırık yüzey analizleri ise kırılmanın gözenek duvarlarından başlayan mikro-çatlakların birleşmesiyle oluşan ve yük eksenine 45° açı ile uzanan makro-çatlaklar ile gerçekleştiğini göstermiştir.

Bahsi geçen karakterizasyon çalışmalarına ek olarak, hem sinterlenme sıcaklığı ve süresinin hacimce %58 gözenekli TiNi köpüklerin, hem de ısıl işlemin hacimce %49 gözenekli TiNi köpüklerin içyapı ve mekanik davranışına etkileri SEM ve basma testleri ile incelenmiştir. Hacimce %49 gözeneğe sahip TiNi köpüklerde yapılan 450 °C'de 1,5 saat yaşlandırma işlemi, Ti_3Ni_4 çökeltilerinin süperelastik davranışı iyileştirdiğini göstermiştir.

Keywords: Boşluk Yapıcı Yöntem, TiNi Köpük, Basma, Süperelastisite, Yorulma

To My Family

ACKNOWLEDGEMENTS

TABLE OF CONTENTS

xi

CHAPTER 1

INTRODUCTION

TiNi alloys, which were first developed by Naval Ordinance Laboratory, USA, in1961, have attracted considerable attention due to their distinct shape memory and superelasticity properties. Moreover, they have very low elastic anisotropy resulting in higher ductility. Having good corrosion and abrasion resistance in addition to the mentioned outstanding properties make TiNi alloys commercially used as flap in air-conditioner, coffee maker, brassiere, antenna for mobile phones, medical applications such as orthodontic wire, guide wire and stent etc. Furthermore, there are ongoing studies to employ TiNi in the other fields of engineering as seismic dampers, micropumps, microvalves, etc.

While the wide range of applications of TiNi alloys make them highly appealing, production of TiNi in the porous form further enlarges their application fields. Processing of TiNi alloys in porous form enables close control of their mechanical properties along with an architecture suitable for the transport of body fluids, which has vital importance in medical applications. Moreover, porous TiNi alloys have been studied extensively for biomedical applications due to their elastic modulus similar to that of bone since the elastic response of the implant material has to be considered cautiously to prevent the so called "stress-shielding effect". This mainly corresponds to the resorption of the bone and loosening of the implant because of the mismatch between the elastic module of implant material and bone, which is generally valid for implant materials much stiffer than bone.

Processing of porous TiNi alloys are generally conducted with powder metallurgical techniques due to their high melting point and highly reactive nature. There are several methods reported in literature for the processing of porous TiNi alloys including hot-isostatic pressing (HIP), self-propagating high-temperature synthesis (SHS), spark plasma sintering (SPS), metal injection molding (MIM), conventional sintering (CS), sintering with space holder, etc. The main drawback of the methods such as SHS, which employ elemental powders for processing TiNi foam, is the formation of secondary intermetallics and oxide phases. The secondary intermetallics as well as oxide phases degrade the mechanical response as well as increase the possibility of Ni release during implant applications. The methods such as HIP, MIM and SPS, on the other hand, require high cost equipment for manufacturing. Among the mentioned methods, sintering with space holder technique from prealloyed powder seems to be best for the prevention of unwanted phases in addition to the close control of the shape, size and distribution of pores.

The main aim of this research is processing and characterization of porous TiNi that can be used in structural and functional applications. The processing method, which was first reported by Esen *et.al.* [1] for porous Ti-6Al-4V alloy production, was improved in the scope of this study. The optimization of the processing conditions according to the mechanical properties and altering the microstructure with different heat treatment procedures to investigate their effects are the primary interests of this study. Furthermore, the fatigue behavior of TiNi foams, which is quite scarce in the literature, especially important for their structural applications was analyzed in detail.

In the present study, theoretical background about TiNi alloys including characteristic properties, heat treatment and application fields as well as processing porous TiNi alloys with different techniques were presented in Chapter Two. The experimental method employed in processing porous TiNi alloys and the characterization methods used were given in Chapter Three. The effects of processing parameters in addition to applied heat treatment on the obtained

microstructure and mechanical behavior of TiNi foams were discussed in Chapter Four. Finally, Chapter Five was a summary of the conclusions derived from this study.

CHAPTER 2

THEORETICAL BACKGROUND

2.1. Titanium and Titanium Alloys

Titanium (Ti) has high specific strength relative to its low density making it attractive in structural applications. Its excellent corrosion resistance further enlarges the field of applications despite its higher cost. Its superb corrosion resistance is due to the protective TiO_2 oxide layer that forms at the surface of Ti and its alloys even at room temperature [2].

Pure titanium (Ti) has hcp (α) crystal structure with lattice parameters a = 2.95 Å and c = 4.68 Å at room temperature. However, upon heating, α transforms into bcc (β) crystal structure with lattice constant of a = 3.32 Å at ~882 °C [2-4]. Although being the high-temperature phase in pure Ti, β phase can be obtained at room temperature via alloying element addition. Accordingly, Ti alloys are generally classified as α, β and $\alpha+\beta$ alloys. Among other Ti alloys, β-Ti alloys have higher fatigue strength, good hardenability and lower elastic modulus, which made them attractive for biomedical applications. On the other hand, TiNi, which is classified as β-Ti alloy, has unique properties such as shape memory and superelasticity that further increases the interest for utilization in biomedical applications.

2.2. TiNi

TiNi alloys were first found at 1961 and named as Nitinol by Naval Ordinance Laboratory, USA [5]. After the invention, TiNi alloys became quite popular due to

their shape memory and superelasticity properties, which will be explained in detail later. Moreover, they have very low elastic anisotropy, which is defined as the proportion of resistance to shear in basal plane with respect to {110} <110> shear, resulting in higher ductility. Having good corrosion and abrasion resistance in addition to the mentioned outstanding properties make TiNi alloys commercially used as flap in air-conditioner, coffee maker, brassiere, antenna for mobile phones, medical applications such as orthodontic wire, guide wire and stent etc. [6].

2.2.1. Phase Diagram and Crystallography

TiNi is an intermetallic compound having B2 (CsCl) type ordered structure with a lattice constant of 3.015 Å at room temperature. B2 transforms into BCC at 1090 °C, which is the order-disorder transformation temperature. At Ti-rich side of the phase diagram TiNi is in equilibrium with Ti_2Ni phase, which has cubic unit cell (space group: Fd3m) with a lattice parameter of 11.320 Å, as given in Figure 2.1. Ti_4Ni_2O, which is the commonly observed oxide form of TiNi, also has a structure similar to that of Ti_2Ni.
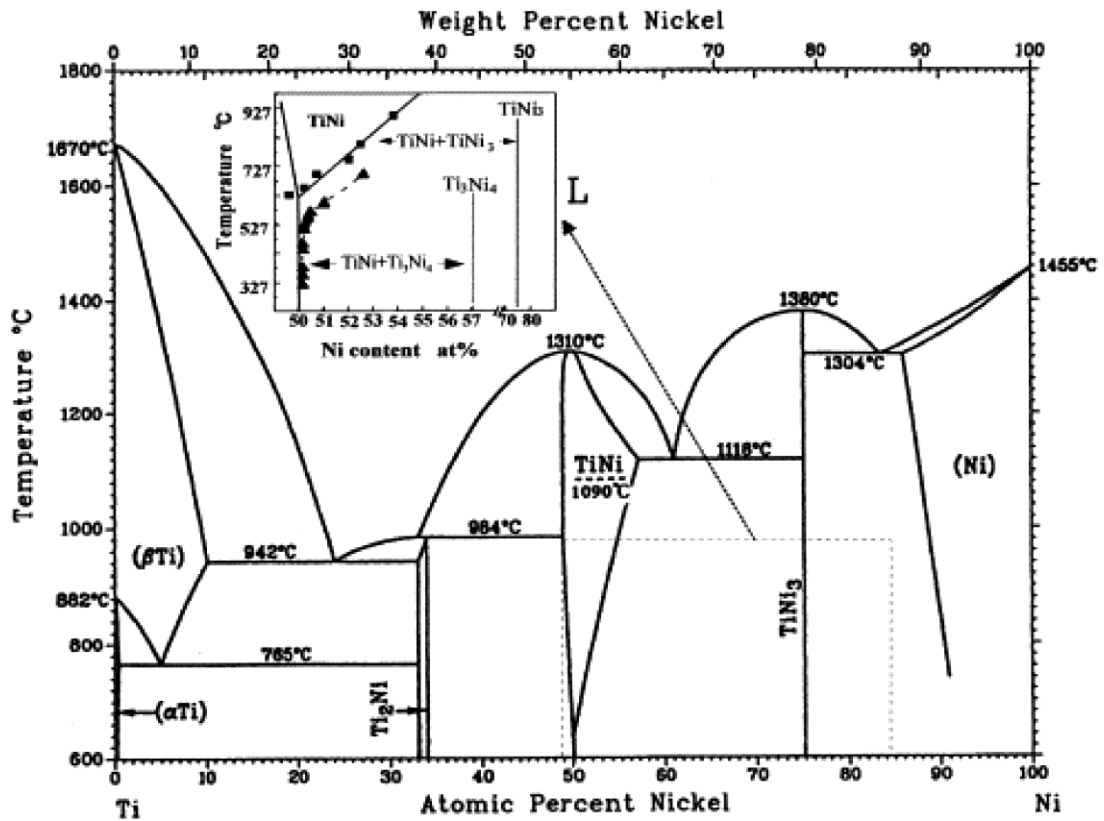
Figure 2.1 Phase diagram of Ti-Ni with a representative portion of the Ni-rich side of TiNi.

TiNi is in equilibrium with TiNi$_3$ on the Ni-rich side of the phase diagram. TiNi$_3$ has a DO$_{24}$ type ordered structure with lattice constants of a = 5.101 Å and c = 8.307 Å, respectively [6]. Although the only phase that was in equilibrium with TiNi is TiNi$_3$ according to the phase diagram, there are intermediate phases that are observed upon aging of TiNi. Ti$_3$Ni$_4$ phase, which has an important contribution to transformation mechanisms and mechanical properties, can be detected at lower aging temperatures for shorter times. As the temperature increased or aging is continued for prolonged time Ti$_2$Ni$_3$ phase forms as Ti$_3$Ni$_4$ phase is dissolved in the matrix. The same situation is applicable to TiNi$_3$ formation at higher temperatures and/or longer time as can be understood from the time-temperature-transformation (TTT) diagram given in Figure 2.2.
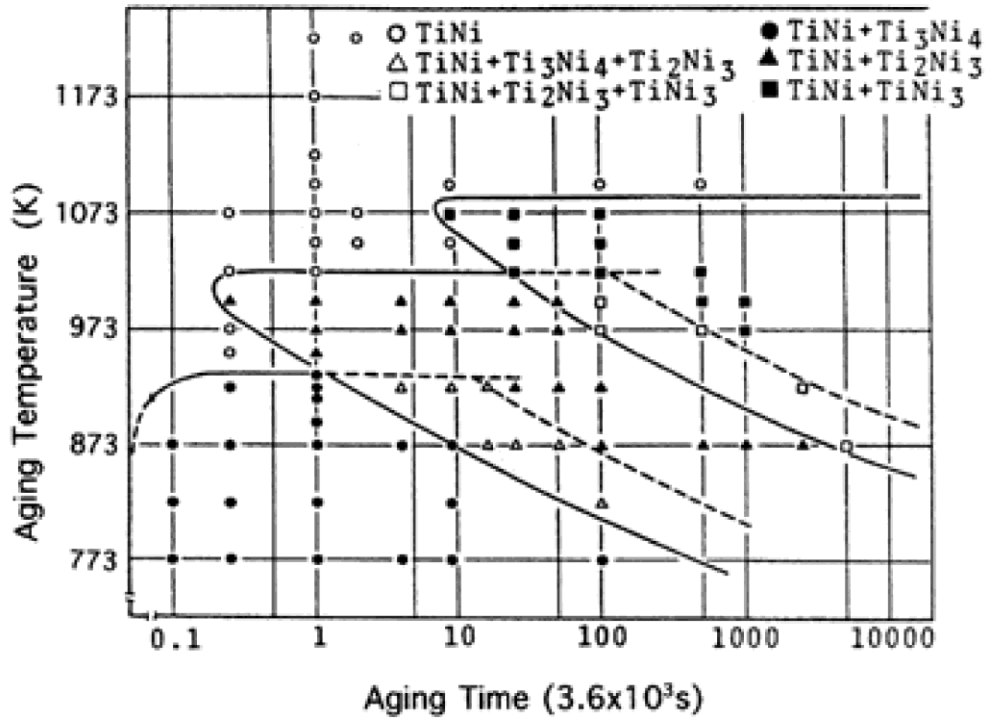
Figure 2.2 A representative TTT diagram describing aging behavior of Ti–52 at% Ni alloy [7].

The structure of Ti_2Ni_3 precipitate was found to be dependent on the aging treatment. Aging at higher temperature results in a tetragonal structure while orthorhombic structure will be formed at lower temperatures. Also one phase transforms into the other martensitically by changing the temperature [6]. On the other hand, Ti_3Ni_4 phase has a rhombohedral unit cell with lattice parameters of a = 6.70 Å and α = 113.8° (Figure 2.3 (a)). The shape of Ti_3Ni_4 precipitates is lenticular with a habit plane parallel to (111) of B2 type TiNi phase (Figure 2.3 (b)).
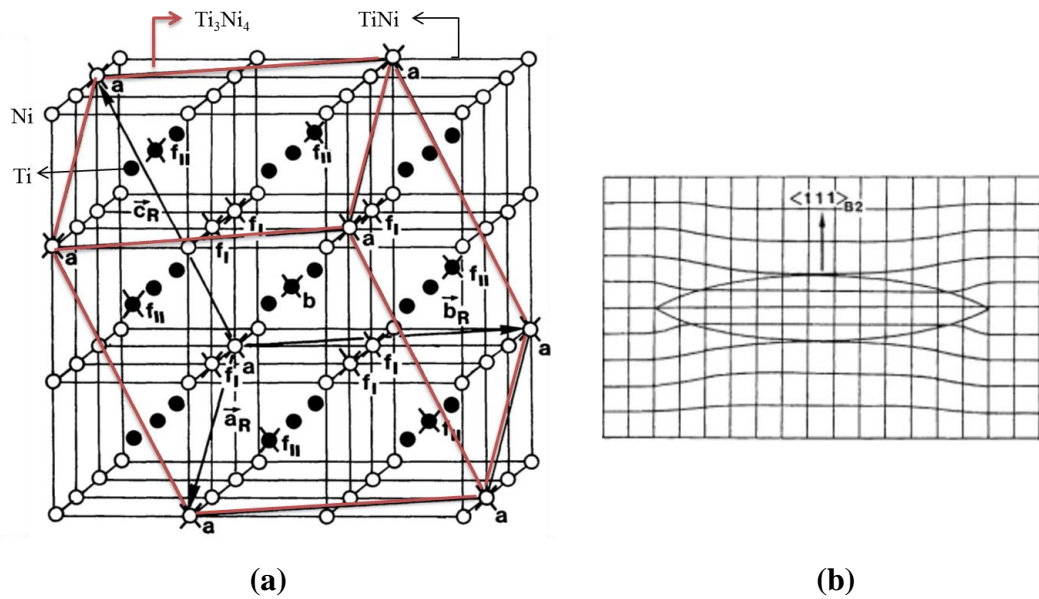
Figure 2.3 The schematic illustration of (a) relationship between the crystal structures of TiNi and Ti_3Ni_4 [8], (b) the lattice distortion of the matrix surrounding Ti_3Ni_4 precipitate [6].

Ti_3Ni_4 phase, due to its small dimensions, was first detected by Transmission Electron Microscope (TEM) studies from the diffraction patterns. As it is given in Figure 2.4, the presence of Ti_3Ni_4 precipitates can be differentiated by the reflections located at 1/7 positions along <123>* reciprocal vectors of the B2 type matrix phase.

Under normal aging conditions, only precipitation of Ti_3Ni_4 phase will occur, which leads to the change of martensitic transformation mechanisms as well as transformation temperatures.
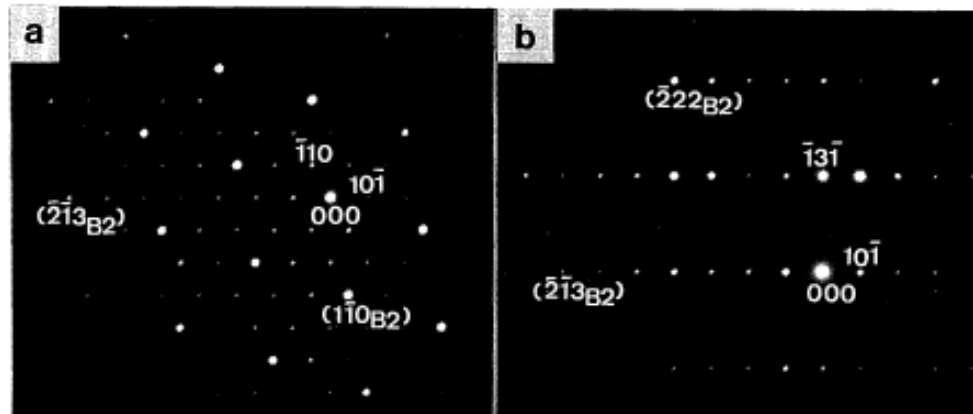
Figure 2.4 Diffraction patterns of Ti_3Ni_4 precipitates: (a) [111] zone, (b) [323] zone (reproduced from [8]).

2.2.2. Martensitic Transformations in TiNi

There are 3 types of martensitic structures, namely R, B19 and B19', that are observed upon quenching of TiNi alloys. If TiNi was solutionized, quenching results in the formation of B19' martensite. However, if aging was applied to form Ti_3Ni_4 precipitates or high density of rearranged dislocations were introduced via thermomechanical treatment, B2 structure will first transform to R phase followed by B19' formation. R phase was also observed in TiNi alloys, which contain a few percent of iron (Fe) or aluminum (Al).

The change in the transformation route arises from the distortion of the matrix by precipitates, dislocations, and tertiary elements making martensitic transformation harder. Although formation of both R and B19' phases are affected, R phase will form first since distortion created by B2 $\rightarrow$ R transformation is less than that of B2 $\rightarrow$ B19'. R phase, which has a triclinic crystal structure, will be formed as given in Figure 2.5. The monoclinic B19' phase, on the other hand, will be formed as given in Figure 2.6. The formation of B19 martensite, which is generally observed in TiNi-Cu alloys, is also given in Figure 2.6 (b). As it is obvious from the figure, formation of B19 martensite is also easier than direct transformation of B2 to B19'.

(a)   **(b)**
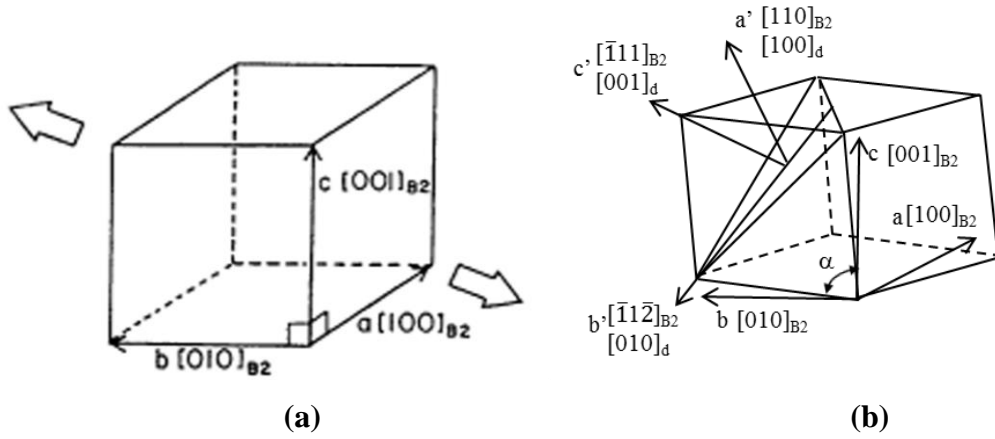
Figure 2.5 Schematical drawing showing the structural change from (a) B2 to (b) R
phase with decreasing temperature (reproduced from [6]).

(a)   **(b)**

(c)
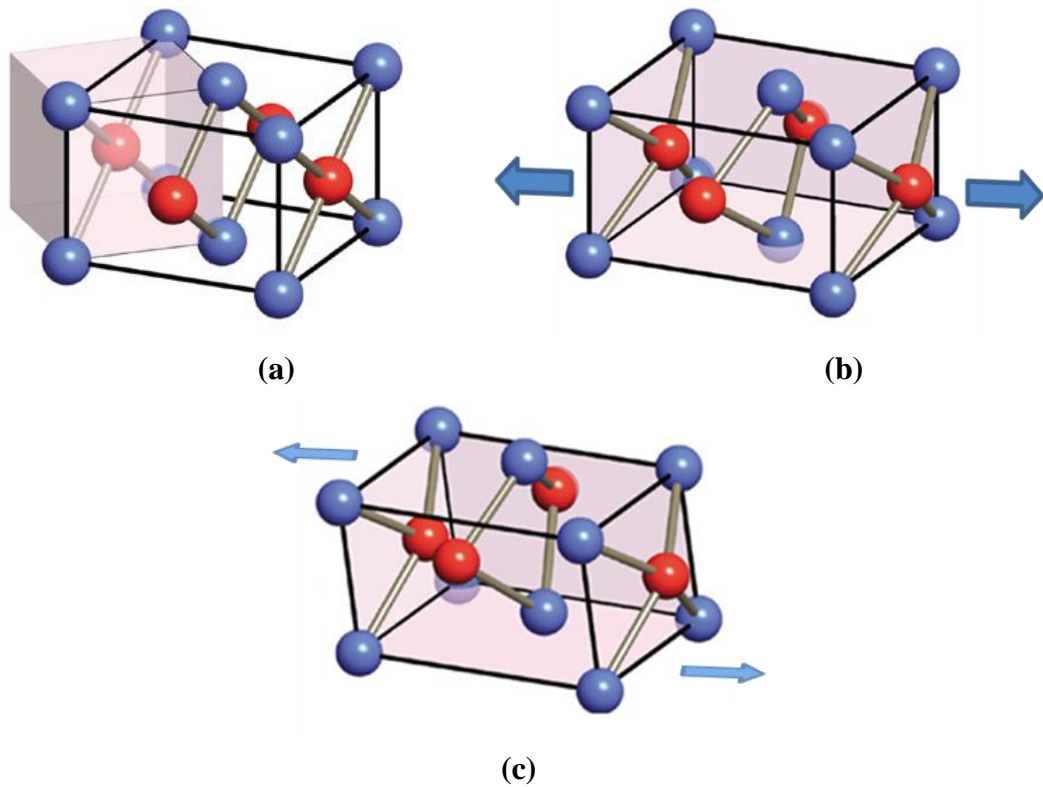
Figure 2.6 The illustrations of atomic arrangements in (a) B2, (b) B19 and (c) B19'
indicating the structural changes that occur during transformation (reproduced from
[11]).

The change in transformation route is accompanied by the change of transformation temperatures since martensitic transformation temperatures are highly dependent on composition of TiNi. The alloying element additions will increase or decrease the transformation temperatures according to the type of alloying element since tertiary elements will replace either Ti or Ni atoms resulting in a change of Ti:Ni ratio. As Ni concentration increases the transformation temperatures will drastically decrease, i.e., as given in Figure 2.7 for martensite start temperature (M_s).
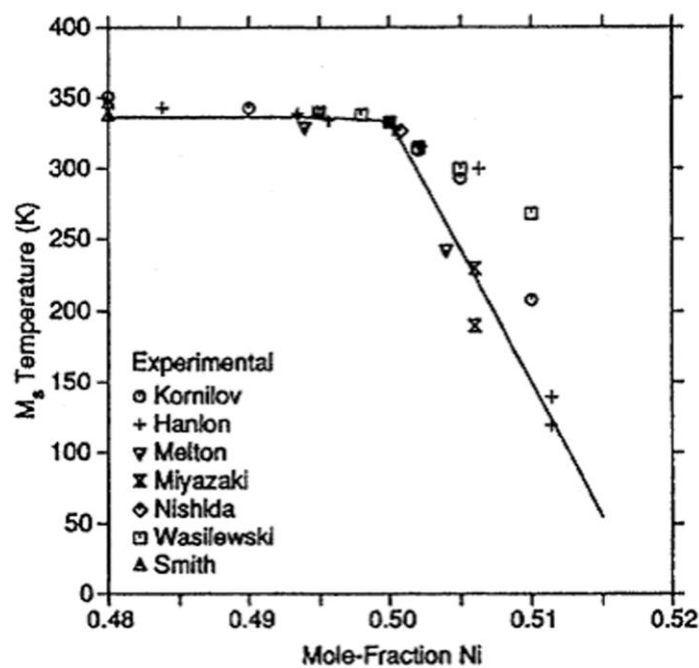
Figure 2.7 The relation of M_s temperature with Ni concentration of TiNi [6].

Aging also have a similar effect due to the precipitation of Ti_3Ni_4, Ti_2Ni_3, or $TiNi_3$ which lead to a decrease in Ni concentration. Accordingly, transformation temperatures will increase in proportion to the alteration in nickel concentration, which is in correlation with the aging temperature and time. Among the three precipitates, which are observed in age hardenable TiNi alloys, Ti_3Ni_4 has the

outmost important since it has drastic effects on shape memory and superelasticity properties.

2.2.3. Shape Memory and Superelasticity

To understand the mechanism lying under shape memory and superelasticity, martensitic transformations have to be considered. Martensitic transformations are explained as diffusionless transformations where transformations from parent phase to martensite takes place by cooperative movement of atoms. Martensite phase, which has a lens-shaped morphology, will form as a result of shearing deformation. The shearing deformation usually occurs parallel to the habit plane between parent and martensite phases that is kept undistorted during transformation. As the result of the cooperative movement of atoms under that shearing deformation, one-to-one correspondence, which is called as lattice correspondence, will be formed between parent and martensite phase. The distortion created by the shearing deformation will be reduced by the complementary slip or twinning deformations, which are called as lattice invariant strains [12].

Most familiar martensitic transformation in metallurgy is the one that is observed in steels. Martensitic transformation in steels needs large driving force for austenite to martensite transformation since entrapped interstitial carbon atoms in the structure create profound distortions. In addition, this irreversible martensite crystal will grow quickly once nucleated and further transformation will occur by the nucleation of new martensite crystals, which is triggered by further temperature drop. However, reversible martensitic transformations in TiNi have thermoelastic nature, which acquires small driving forces for forward and reverse transformations. The thermoelastic martensitic transformations take place by the growth of nucleated martensite plates in a very narrow temperature range. On the contrary to martensite phase that is observed in steels, thermoelastic martensite in TiNi will shrink with the increase in temperature. Typical heating-cooling curves representing the critical transformation temperatures is given in Figure 2.8. As the material is cooled below

the M_s temperature, martensitic transformation starts to take place and transformation proceeds with decreasing temperature till M_f temperature, where all of the structure becomes martensitic, is reached. The reverse transformation occurs in the same manner after increasing temperature up to A_s, which is usually higher than M_s. The hysteresis of the transformation, which will be defined as the temperature difference between forward and reverse transformation curves that is measured from the mid-point of forward transformation curve, reflects the energy requirement for the transformation to occur.
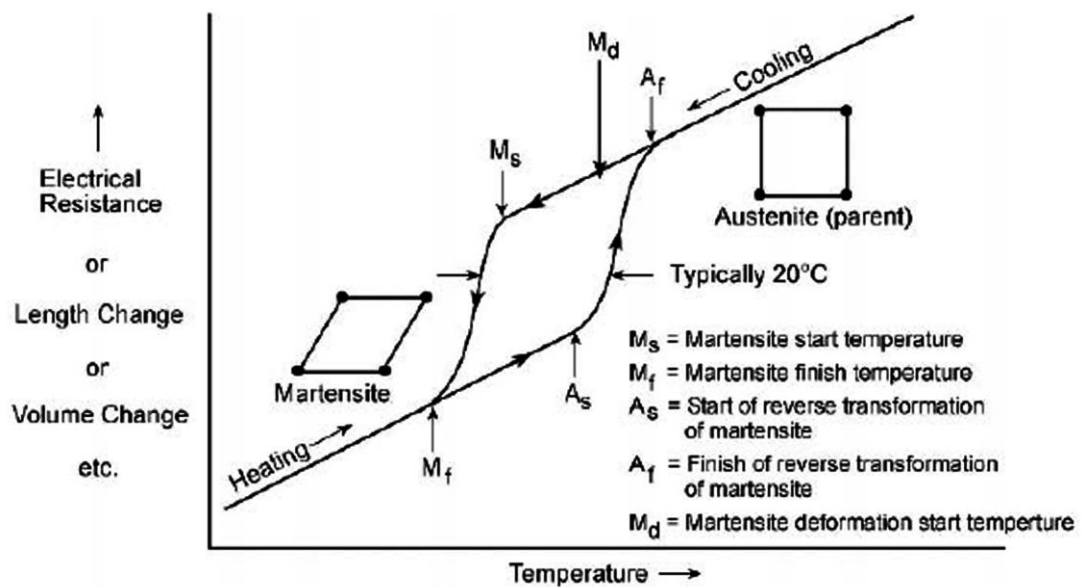
Figure 2.8 Representative diagram for the austenite-martensite transformation of the shape memory alloys [13].

Hamilton *et.al.* have clarified the parameters that affect hysteresis in shape memory alloys (SMAs). They proposed that there need to be a local balance between the chemical and non-chemical contributions of the total Gibbs free energy to maintain thermoelastic equilibrium during martensitic transformation. Chemical contribution was defined as energy difference between the parent and martensite phases while the non-chemical constituents was seperated into two groups according to being

reversible or not. The reversible constituent is composed of elastic strain energy stored during deformation and the irreversible component is the sum of frictional work, which is attributed to interface motion, and dissipation of elastic strain energy, which is observed due to the relaxation of coherency strains between parent and martensite phases. They also gave a schematic explanation for the change of martensitic transformaiton behavior with the addition of each parameter as given in Figure 2.9.
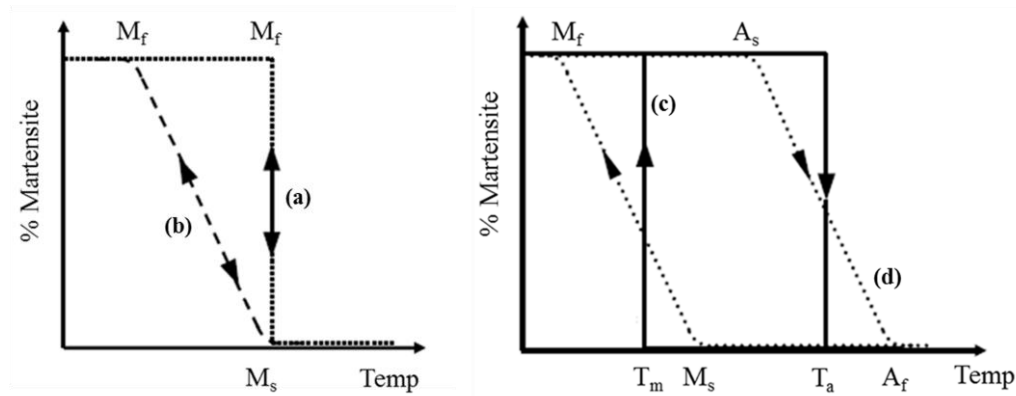
Figure 2.9 The roles of different parameters on martensitic transformation behavior of SMAs: (a) chemical constituent, (b) elastic strain energy in combination with (a), (c) energy dissipative mechanisms considered with chemical constituent, (d) total effects of all 4 parameters (reproduced from [14]).

Figure 2.9 (a) represents the fully reversible martensitic transformation that occurs at a definite temperature since there is no non-chemical constituent operative whereas the system requires undercooling to complete transformation as the elastic energy stored is preventing the transformation to proceed. On the other hand, stored elastic energy assists the reverse transformation, which follows the same path due to the lack of energy dissipating mechanisms (Figure 2.9 (b)). In the presence of energy dissipative mechanisms, part of the driving force created by chemical constituent will be used and additional undercooling and overheating is needed for the transformation to occur. If all parameters were taken into account, the hysteresis will be as given in Figure 2.9 (d) since variable elastic strain energy that is stored during

transformation will be dissipated as frictional work and further chemical energy will be required for further transformation. Accordingly, the difference between the start and finish temperatures will be large while the hysteresis will be small as the stored energy increases. In addition, as the energy dissipative mechanisms became more operative the hysteresis will be larger [14].

The hysteresis of the martensitic transformation of shape memory alloys is narrow due to the thermoelastic nature of the transformation. Thermoelastic martensitic transformations are characterized by mobile and reversible boundary (interphase between parent and martensite phases) movement. Reversibility of the transformation is attained by twinning that is introduced as lattice invariant shear, which results in formation of correspondence variants [6]. Moreover, the structural changes need to be low during transformation and there will be good coherency between parent and martensite lattices. During the transformation, dislocations should not be activated and sufficient number of variants should be present. These conditions will be met if the parent phase has an ordered structure [12].
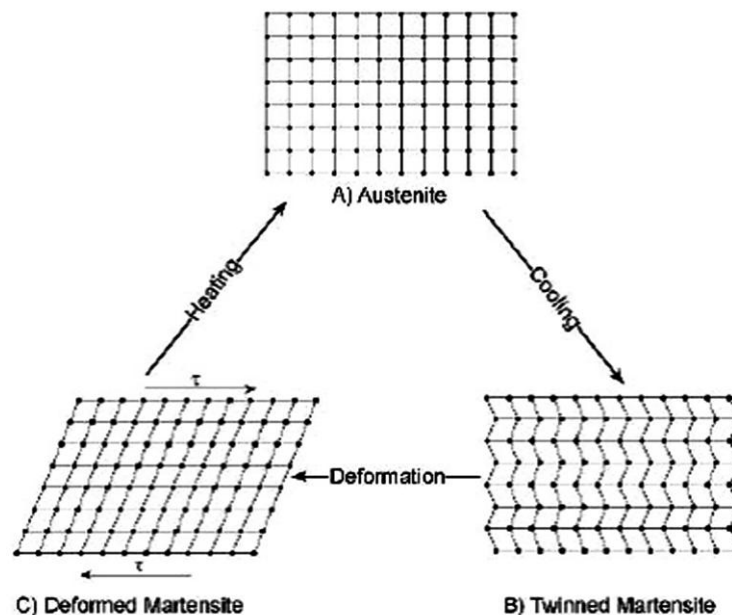

Figure 2.10 Schematic representation of the shape memory effect [15].

15

Shape memory effect can be defined as the ability of the plastically deformed structure to retain its original shape by heating. This behaviour is observed due to the deformable nature of martensite as given in Figure 2.10. During cooling, martensite plates that are formed by shear deformation self-accommodate to retain the original shape of the material. As the martensite deforms, deformation proceeds by the twin boundary motions resulting in a single variant martensite, which is the most favorable variant among 24 habit plane variants for the applied stress condition. Upon heating to a temperature above A_f, the martensite transforms back to austenite in the original orientation, because of the lattice correspondence [2, 6, 9, 10].

Due to its shear-like nature, austenite to martensite transformation can be attained by deformation as well. If a stress is applied to the same material in the temperature range between M_s and M_d, martensite can be stress-induced. This behavior, which is called as superelasticity or pseudoelasticity, is observed due to the fact that energy required for martensitic transformation can be compensated by the deformational energy. Figure 2.11 demonstrates martensitic transformation of TiNi single crystal under applied stress. TiNi single crystal elastically deforms during Figure 2.11 (a) while martensitic transformation starts when the critical stress level is attained. Transformation starts from the most favorably oriented martensite plate, which has the highest resolved shear stress acting across its habit plane, among 24 martensite plate variants. The martensite plate has an internally twinned martensitic structure (Figure 2.11 (b)) and generally called as corresponding variant pair since it is composed of two twin related martensite single crystals. If deformation proceeds, the detwinning occurs (Figure 2.11 (c)) with the growth of favorably oriented martensite variant among its twin related neighbor to create single crystal martensite. During detwinning elastic strains are accumulated due to distortion of the habit plane. If deformation continues, single crystal of martensite will deform elastically as given in Figure 2.11 (d) [16]. However, if the applied stress was

removed before the last stage, the martensitic structure cannot be retained since the stable phase at this temperature range is austenite.
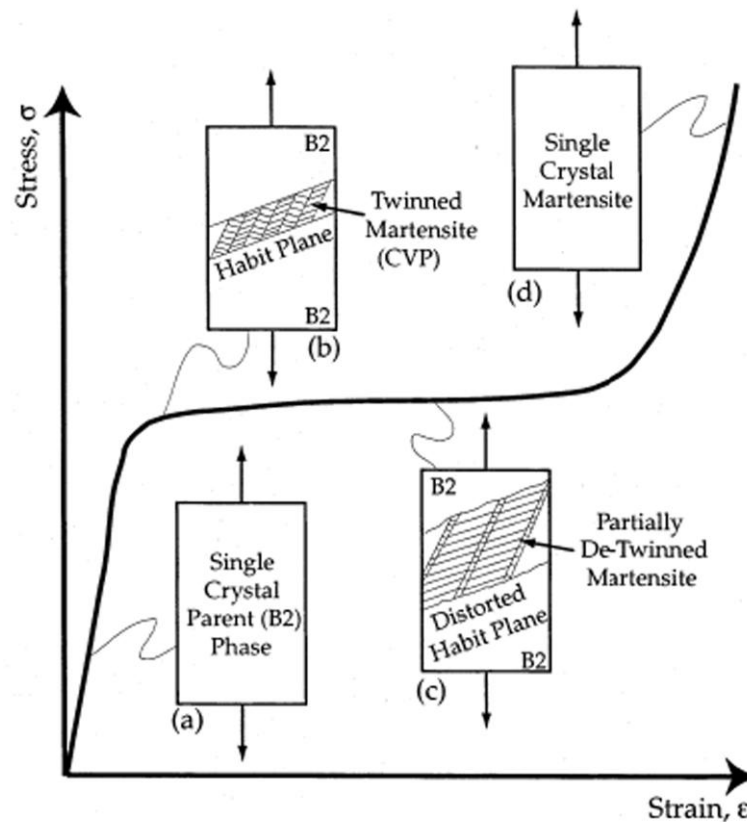
Figure 2.11 Idealized martensitic transformation of single crystal under applied stress [16].

Both shape memory and superelasticity were explained in a simplified manner and it is obvious that both properties can be observed in the same material according to the test temperature as given in Figure 2.12. However, the slip resistance of the material needs to be high for shape memory and superelasticity to be observed. If the critical stress to induce slip is as low as in the case of (B), there will be less or no superelasticity since slip is an irreversible process.
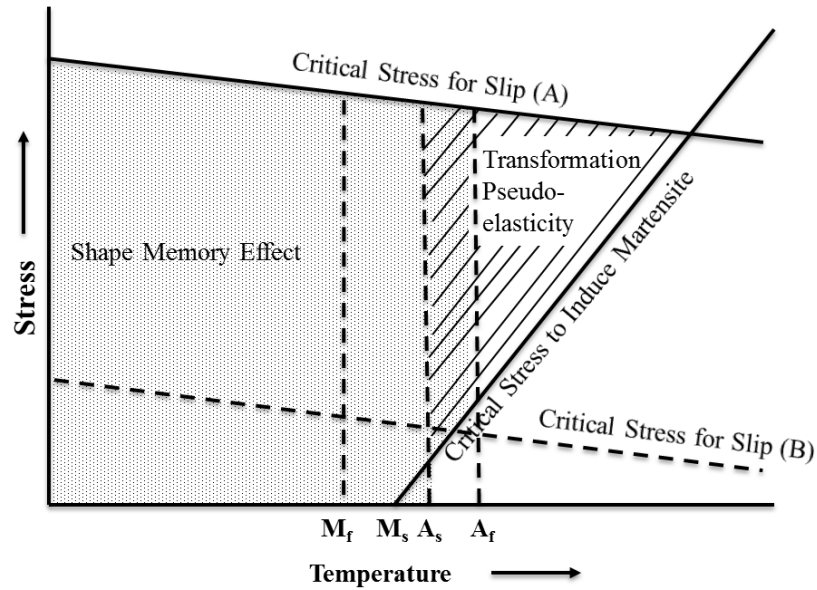
Figure 2.12 Schematic representation of stress-temperature regions that shape memory effect and superelasticity is observed (reproduced from [17]).

In order to clarify the microstructural changes of TiNi alloys during deformation at different temperatures, tensile stress-strain behavior of polycrystalline Ti-50.5 at%Ni alloy during both shape memory and superelastic ranges given by the addition of temperature scale in Figure 2.13 [18]. At point "0" of Figure 2.12, TiNi has completely martensitic structure since temperature is below M_f. If TiNi is deformed at this temperature, the twinned martensite will be detwinned by the application of load and detwinned martensite will be preserved after the removal of load. The only way to recover the microstructure is application of heat till A_f temperature is reached. The detwinned martensite will transform into austenite upon the system reaches A_s temperature and become fully austenitic after A_f temperature exceeded. If this fully austenitic temperature is deformed at a temperature in the range of $A_f - M_d$, martensitic transformation will take place after a critical stress level. However, martensitic structure is not stable at this temperature unlike to the first case and austenitic transformation will take place upon removal of load.
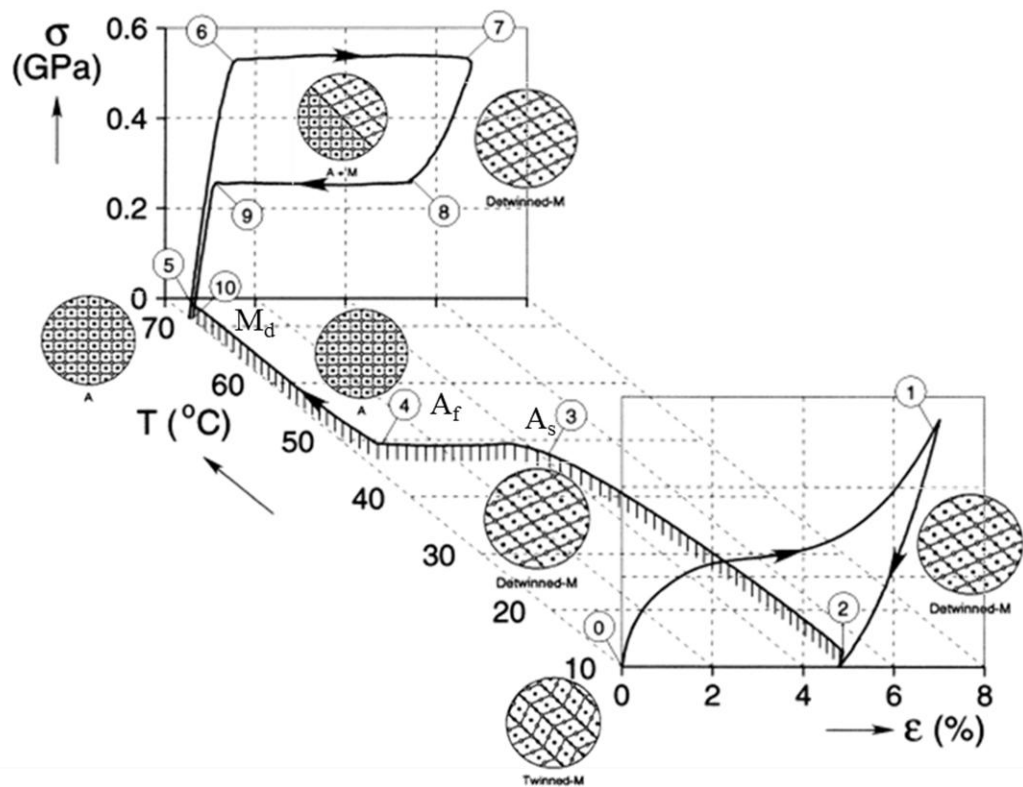
Figure 2.13 Thermomechanical behavior of TiNi alloys (reproduced from [18]).

As it is obvious from Figure 2.13, the deformation behavior of superelastic TiNi is different from generally observed stress-strain response in metallic materials. The region between points 5-6 in the figure, parent phase elastically deforms as usual. However, the parent phase transforms into martensite phase from point 6 to 7 instead of plastic deformation. This is the reasoning behind high recoverable strains obtained by superelastic TiNi alloys. In fact, the plateau region of superelastic transformation in polycrystalline TiNi is not always totally horizontal as given in Figure 2.13 since different crystallographic orientations result in different deformation characteristics. As proposed by Şehitoğlu *et.al.* crystallographic orientations like [001], [111], etc. that lie on a symmetry boundary exhibit more than one favorable martensite plate while less symmetric orientations like [148] can only have one favorable martensite plate upon deformation. Two or more martensite variant formation result in the interaction of the variants, which is similar to that

19

observed in strain hardening, leading to an increase in the slope of the stress-strain curves [19]. These differences also contribute to the commonly observed tension-compression asymmetry in TiNi alloys. If a polycrystalline TiNi alloy sample is deformed under monotonic tension, the stress required for martensitic transformation will be higher, the transformation plateau will be more linear and recoverable strain after removal of stress will be higher than it will be under monotonic compression deformation [16]. The mentioned asymmetry was attributed to the difference in martensite variants, which will be active in compression and tension, leading to distinct transformation strains. In other words, Gall *et.al.* claimed that during compression, critical stress for martensitic transformation will be lower since martensite variants will be more favorably oriented to deform under compression than in tension. They also proposed that the inequality between the tension and compression behaviors will be smaller if texture formation is prevented [20].

The diversity in deformation characteristics of different crystallographic orientations also leads to the common occurrence of martensitic transformation and austenite yield during deformation of TiNi as given in Figure 2.14. As explained before, applied stress will cause elastic deformation of the austenite during Stage I. Increasing the stress in Stage II will yield stress-induced martensitic transformation to occur. In this stage, slip deformation of austenite will also occur partially depending on the orientation of the slip planes with respect to the loading axis. If deformation was continued up to Stage III, the stress-strain diagram exhibits a downward curvature when the martensite yield point, which is ~60% higher than that of austenite, is reached. If the load was removed before the fracture of specimen, the elastically deformed martensite will be recovered first. Afterwards, the reversed transformation will be observed in pseudoelastic regime. The remaining strain after full unloading will be recovered by heating the specimen above A_f+80 K. There will be residual strain even after this treatment depending on the amount of maximum strain applied during loading.
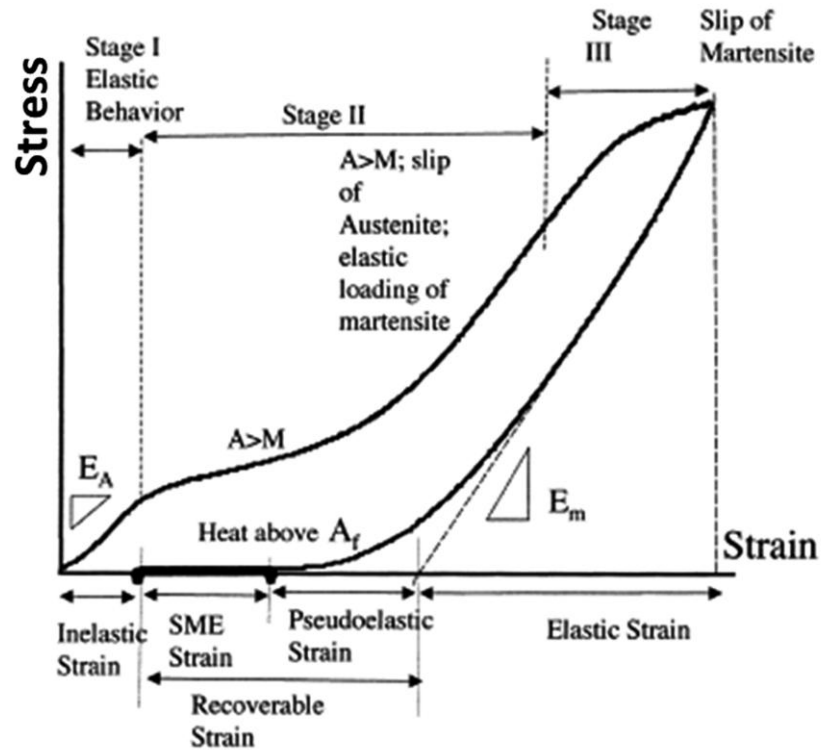
Figure 2.14 Representative stress–strain curve of TiNi alloys indicating the compressive deformation behavior [19].

Even if the stress induced martensite totally recovers upon removal of the load for the first cycle, it was observed that cycling at constant stress/strain results in the accumulation of residual strains as well as the changes in the stress-strain behavior [3, 17, 21, 22]. It was observed that both the critical stress, which is required to trigger martensitic deformation and hysteresis of strain under constant stress cycling (or stress hysteresis under constant strain cycling) decrease when the number of cycling increases. Moreover, it was determined that the degree of change in accumulated residual strain, critical stress and hysteresis tend to attenuate with the increasing number of cycles reaching to a point where the stable pseudoelastic behavior was attained.
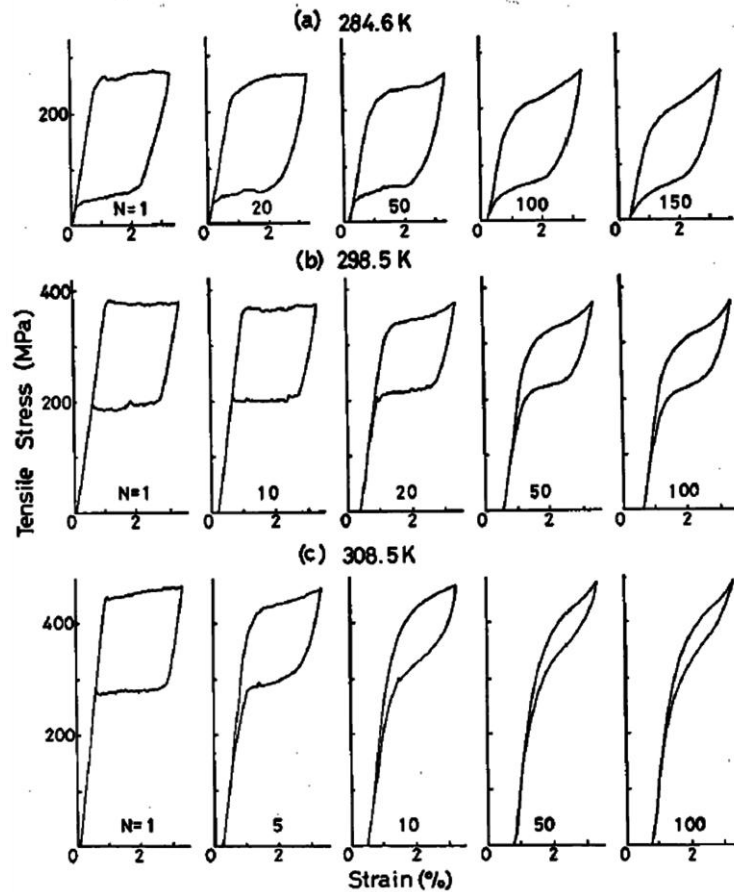
Figure 2.15 The effect of cycling on stress-strain response of superelastic TiNi [21].

Miyazaki *et.al.* have proposed that the residual stress accumulation was introduced by the compound effect of activated slip deformation and presence of residual martensite. The slip deformation originates from the martensite-martensite interfaces during reorientation of martensite under applied load while residual martensite will be formed as a consequence of dislocations acting as obstacles for reverse transformation [21]. Correspondingly, the internal stress field created by slip deformation assists the martensitic transformation leading to a decrease in critical stress to introduce martensite. The created internal stress also results in strengthening of the matrix and results in a resistance to the strains caused by martensitic transformation. Accordingly, the hysteresis becomes narrower as given in Figure 2.15 [17]. It is also obvious from the figure that the changes observed

become more severe when the level of applied stress has increased. The role of test temperature is also evident from this figure; as the test temperature increases stress required to trigger the martensitic transformation also increases. It was an expected result since deviation from the critical temperature, under which martensite phase is stable, increases requiring more driving force for the transformation. Another effective parameter in cyclic response of TiNi alloys is the composition of the alloy. The strength is directly proportional to the Ni-content in TiNi alloys and consequently as the Ni-content increases, amount of the width of hysteresis and residual stress accumulation decrease while the critical stress for martensitic transformation increases [14].

The effect of temperature on deformation mechanisms also need to be considered when the rate of deformation was increased. Shaw has proposed that the heat generated during martensitic transformation will affect the deformation behavior if the rate of deformation is not slow enough to permit the generated heat to be released [23]. He claims that local self-heating was occurred during higher rates of loading and this results in the surpass of the nucleation barriers of new martensite fronts. On the other hand, Namet-Nasser *et.al.* conducted a more detailed research on the effect of loading rate on deformation behavior [24]. They determined that critical stress of transformation gradually increases with increasing strain rate with a break point at a strain rate around 1000/s, after which a rapid increment in critical stress was observed. It was also found that only plastic deformation is operative at very high strain rates like 17000/s. Huang *et.al*, additionally investigated the effects of dynamic deformation on shape of loading-unloading cycles and indicated that the hysteresis diminishes, residual strain decreases and superelastic strain increases for a constant stress level [25]. In addition, they observed that the martensitic transformation stress become less distinctive resulting in a more linear deformation behavior as given in Figure 2.16.
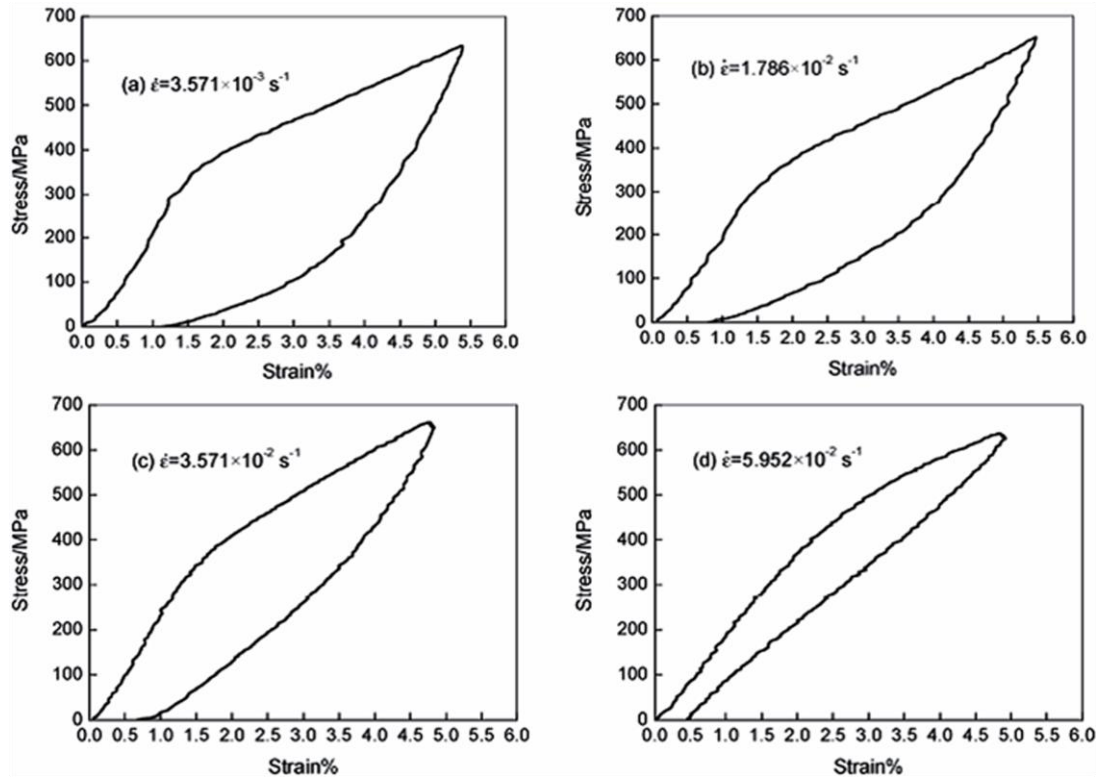
Figure 2.16 The effect of deformation rate on stress-strain behavior of
Ti-50.9 at%Ni [25].

2.2.4. Heat Treatment

The martensitic transformation characteristics and accordingly the mechanical
properties are closely related to the microstructure and accordingly the heat
treatment history of the material. Heat treatment applications are generally
performed with two basic objectives; one of which is the rearrangement of
dislocation structure that was introduced during previous cold-working and the
second one is the precipitation hardening, which both lead to improvement of
mechanical characteristics.

Saburi *et.al.* conducted a series of experiments on cold-rolled Ti-50.2 at%Ni alloy to
determine the effect of heat treatment on superelastic properties. They have found
that at least 25 % deformation prior to annealing at 673 K is required for complete

24

superelastic recovery. The amount of recovery for a given annealing temperature is directly proportional to the amount of prior cold-work since cold-working induces dislocations, which are rearranged during annealing, resulting in the improvement of slip resistance. In addition, they have found that superelasticity degrades if annealing was performed at 873 K since recrystallization temperature of Ti-50.2 at% Ni lies between 773 - 873 K [26].

There is only one precipitate phase that can be obtained by aging Ti-rich TiNi alloys, which is Ti_2Ni. However, Ti_2Ni precipitates generally segregate at grain boundaries as indicated by Ishida *et.al.* [4] and accordingly they cannot be used to improve shape memory or superelasticity characteristics [6].

On the other hand, three different precipitates can be formed by aging Ni-rich TiNi alloys, which are Ti_3Ni_4, Ti_2Ni, and $TiNi_3$, in the order of increasing Ni-content. However, Ti_3Ni_4, which is the only precipitate obtained under normal aging conditions on the contrary to being metastable, is the most convenient one in terms of their effect on transformation mechanisms and mechanical properties. Ti_2Ni and $TiNi_3$ phases, which precipitate as large particles, are detrimental to shape memory characteristics [27].

The effects of Ti_3Ni_4 precipitation (from this point "precipitate" and "precipitation" will be used to mention Ti_3Ni_4 phase unless otherwise specified) on martensitic transformations can be investigated by taking two parameters into account; change of matrix composition and creation of strain fields. As the consequence of precipitation, composition of the matrix changes (Ni-concentration decreases) resulting in an increase of R_s and M_s (Figure 2.7). Ni-concentration at equilibrium conditions depends on the aging temperature due to the equilibrium attained between TiNi matrix and Ti_3Ni_4 precipitates. The change in M_s temperature caused by the alternative aging done between two temperatures is shown in Figure 2.17.
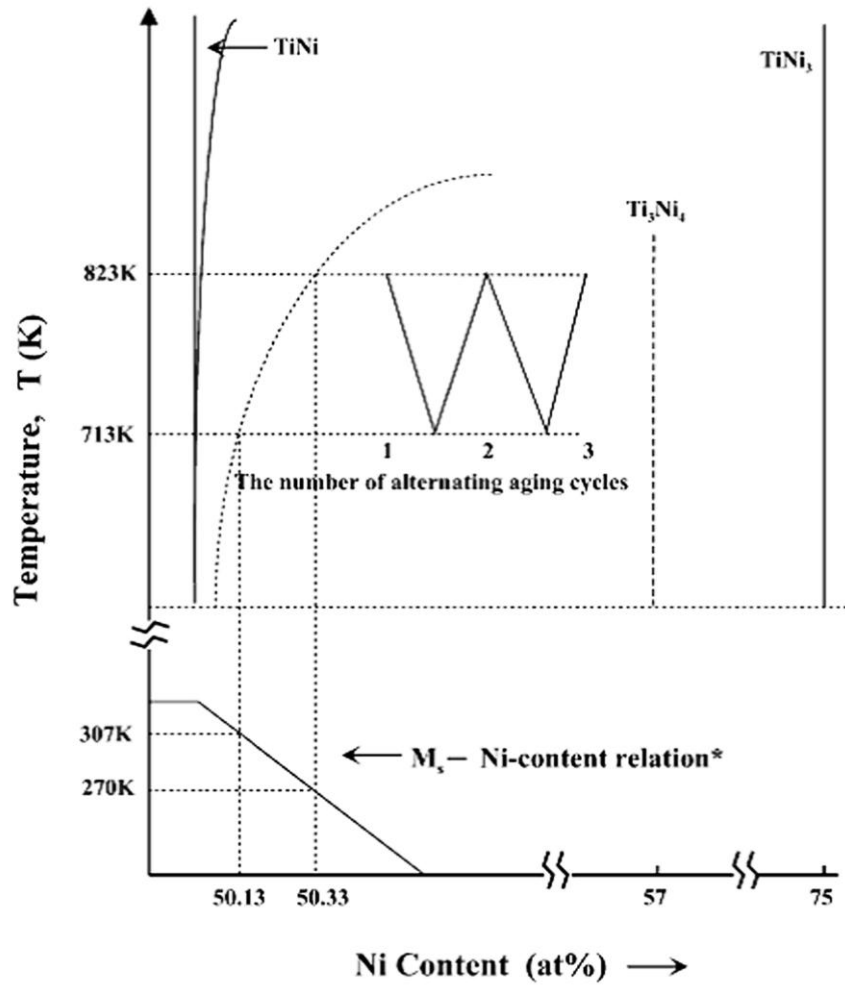
Figure 2.17 Schematic drawing of the solubility line representing the equilibrium between Ti_3Ni_4 precipitates and TiNi matrix, and the resulting transformation temperatures [6].

Huang and Liu have investigated the effects of annealing temperature on superelastic behavior of TiNi alloys by conducting tensile tests on Ti-50.85 at%Ni alloy that has been annealed at varying temperatures in the range of 573-973 K and comparing the results with that of as-received wire [28]. They have found that all transformation temperatures increase with increasing annealing temperature up to 673 K, and then decrease. At the test temperature (room temperature) TiNi alloy consists of both austenite and martensite (R-phase) phases, ratio of which depends on the transformation temperatures, and increase of martensite content leads to

decay of the transformational strain. Although, it was not mentioned in the study, the change in the transformation temperatures as well as the transformation sequence is closely related with the Ti_3Ni_4 precipitation as it is obvious from TTT diagram, which is given in Figure 2.2.

Strain fields of the precipitates have the similar effect on martensitic transformation with that of applied stress. Accordingly, precipitate coherency plays a key role in martensitic transformations. If the coherent precipitate maintains its coherency during transformation under applied stress, stored elastic energy increases resulting in a narrower transformation hysteresis and easier reverse transformation. On the other hand, if precipitate becomes incoherent as the transformation front passes through, martensite-austenite interphase relaxes resulting in a decrease of elastic strain energy [14].

Chumlyakov *et.al.* have found that small coherent precipitates (~30 nm), which were obtained by aging Ti-51 at%Ni alloy at 623 K for 1 hour, result in better superelastic properties over a wider range of temperature than the same alloy containing large (~430 nm) incoherent precipitates that were formed by aging at 823 K for 1.5 h [29]. Şehitoğlu *et.al.* determined the peak-aging conditions for Ti-50.8 at%Ni alloy as 723 K and 1.5 h at which coherent precipitates of size ~50 nm are formed [22]. However, Gall *et.al.* found that incoherent precipitates, which were formed by aging Ti-50.8 at%Ni alloy at 823 K for 1.5 h (~400 nm), result in better performance under cyclic loading up to fracture since their formation causes more Ni-depletion in the matrix and lower Ni-content provides more ductility [30].
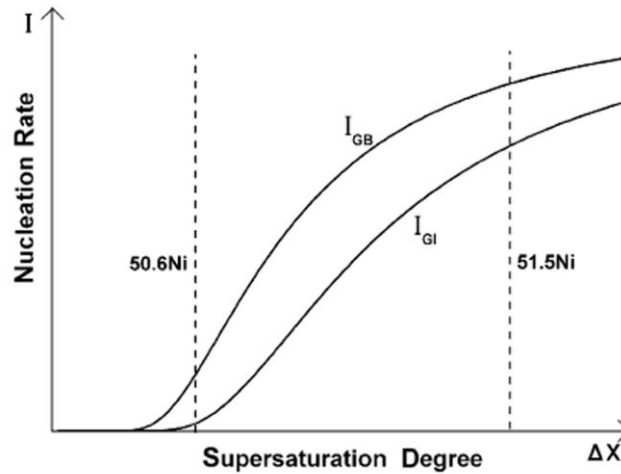
Figure 2.18 The relation in between the nucleation rate and deviation from equilibrium before precipitation [31].

On the other hand, Hamilton *et.al.* have aged TiNi alloys, with four different compositions varying in the range of 50.1-51.5 at%Ni, at 873 K for 1.5 hours and found that Ti_3Ni_4 prefers to precipitate inhomogeneously, being segregated along grain boundaries for the alloys with a Ni-content of 50.1 at% and 50.4 at% while precipitation occurs homogeneously for the alloys containing 50.8 at%Ni and 51.5 at%Ni [14]. As it is well known, supersaturation (deviation from equilibrium state for that temperature) is needed for precipitation and as the degree of supersaturation increases, the driving force for nucleation of the precipitates will also be increased. This parameter in combination with the grain boundary effect, which has a smaller nucleation barrier for the precipitate, leads to the mentioned change in precipitate distribution by altering alloy composition. Fan *et.al.* have given a schematic diagram (Figure 2.18) indicating the relation between the precipitate nucleation rate and Ni-content for TiNi alloys with Ni-concentrations of 50.6 at% Ni and 51.5 at% Ni, which were aged at 723 K for 1 h [31].

The alteration of precipitation behavior also leads to a change in martensitic transformation behavior from two-step to three-step (B2→R→B19'), which has caused a debate about its origin in the past. However, it was finally agreed that

three-step transformation arise from the difference in the martensitic transformation behavior of the precipitate free matrix (B2→B19') and precipitate segregated grain boundary regions (B2→R→B19') [31, 32].

Moreover, localized precipitation results in inhomogeneous deformation behavior since precipitate-free grain interior transforms by self-accommodating martensites under the influence of applied stress while precipitate containing grain boundaries will transform according to the combined effect of precipitate strain field and applied stress [14].
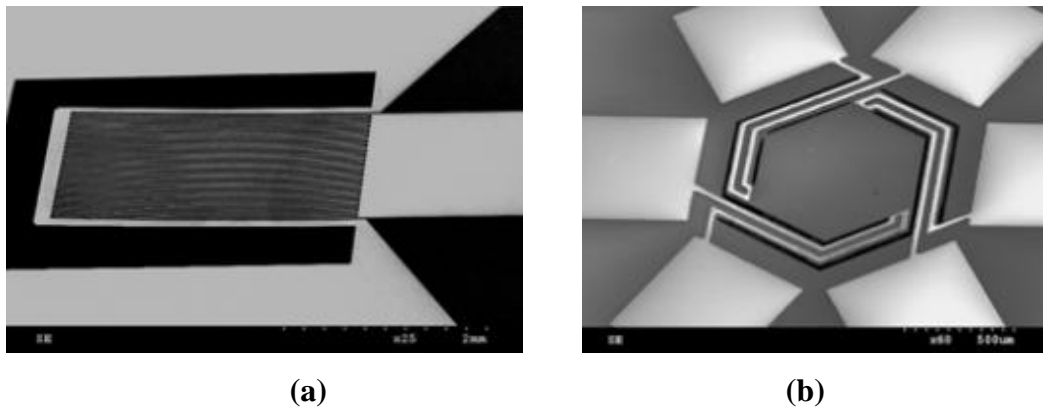
2.2.5. Applications of TiNi Alloys

The mentioned applications of TiNi alloys in this part constitute only a small part of the literature. There are several studies that are still ongoing to improve the properties of TiNi alloys to fulfill the requirements of the determined applications. This part only gives a brief idea about common applications of these alloys.

As mentioned before, unique properties such as superelasticity and shape memory extend the application fields of TiNi alloys among other Ti-alloys. Eijk *et.al.* have proposed that combined effect of shape memory and superelasticity can be utilized as seismic dampers if wrapped bundle of TiNi wires, which are composed of two different composition, one is in superelastic and the other in shape memory range were employed [33].

Another application field for TiNi that is in progress is MEMS (micro-electro-mechanical-systems) applications, which are generally utilized by the integration of mechanical systems on a silicon substrate. As reported by Kahn *et.al.* TiNi thin films were employed in microvalves and micropumps almost 15 years ago [34]. In addition, Fu *et.al.* have reviewed more recent advances in application of TiNi alloys in MEMS and mentioned the problems in exploitation of TiNi alloys in MEMS [35]. They have indicated that TiNi alloys are mainly utilized in microactuators and

presented some example photographs of TiNi alloys employed in microcantilever and micromirror (Figure 2.19).

(a)　　　　　　　　　　(b)

Figure 2.19 Examples of MEMS applications for TiNi alloys: (a) microcantilever, (b) micromirror [35].

On the other hand, TiNi alloys are widely used in biomedical applications due to its similar deformation behavior with that of bone (Figure 2.20) (in addition to superelasticity and shape memory) and consequently the lower elastic modulus compared with the other metallic materials.
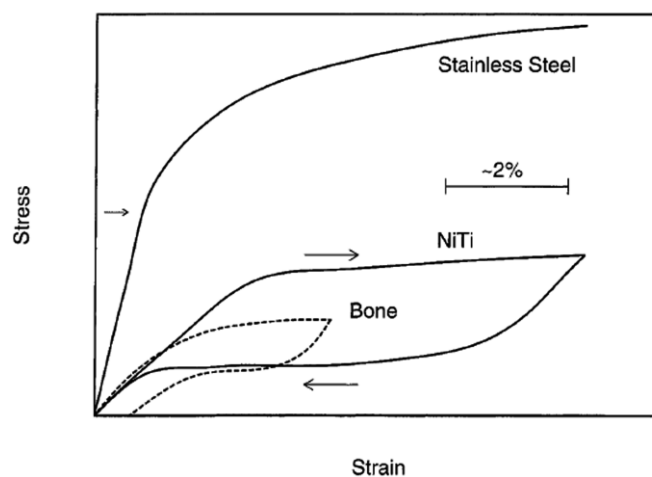

Figure 2.20 Schematical comparison of stress-strain behavior of TiNi, bone and steel [36].

Petrini and Migliavacca have also reviewed the applications of TiNi alloys according to the property of the alloys leading to the employment in this field (Table 2.1) [37]. Photographs of some applications are given in Figure 2.21.

Table 2.1 Main applications of TiNi alloys in biomedical field [37].

Application Field	Property	
	Superelasticity	Shape Memory
Orthodontic	Wires, palatal arches, distractors, endodontic files	Wires
Orthopedic	Intraspinal implants, intramedullary nails	Staples or plates, devices for correcting scoliosis, spinal vertebrae spacer, intramedullary nails, devices for physiotherapy
Vascular	Venous filters, devices for closing ventricular septal defects, self-expandable vascular stents, stent-graft, percutaneous devices to treat valvular diseases	Venous filters, devices for closing ventricular septal defects
Neurosurgical	Coils, stents, microguidewires	
Surgical		Mini-invasive surgical instruments
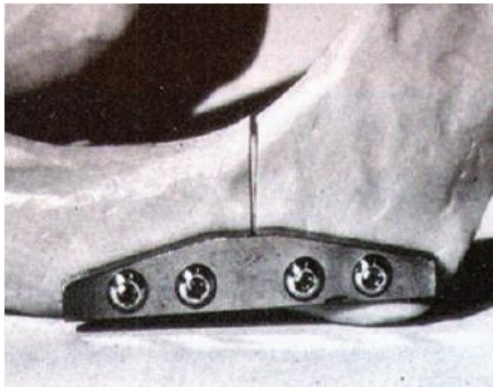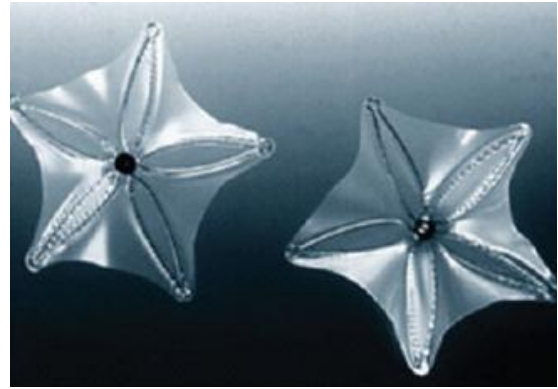
Figure 2.21 Examples of TiNi parts in biomedical applications: (a) plate for mandible fracture, (b) device to close ventricular septal defects, (c) spinal vertebrae spacer, (d) staple for fixing a frontozygomatic fracture (indicated by white circle), (e) example of SMA stents: (top right) coronary stent, (top left) carotid stent, (bottom left) femoral stent (f, g) gloves with SMA wires at low and high temperatures, respectively [37].

2.3. Porous TiNi Alloys

As it was mentioned, its good corrosion and abrasion resistance in addition to the unique properties such as shape memory and superelasticity make TiNi alloys commercially applicable in various engineering applications. Processing of TiNi alloys in porous form, on the other hand, enabled close control of its mechanical properties along with an architecture suitable for transportation of body fluids, which has vital importance in medical applications.

2.3.1. Processing Techniques

There are several methods reported in literature for the processing of porous TiNi alloys including hot-isostatic pressing [38, 39], self-propagating high-temperature synthesis [40, 41], spark plasma sintering [42], metal injection molding [43], sintering with space holder [44], etc. The details of commonly used processing techniques for TiNi foam production in literature is given in this part with their advantages and disadvantages with respect to other methods.

2.3.1.1. Hot-Isostatic Pressing

Elemental powders of Ti and Ni are used for the processing of porous TiNi alloys by hot-isostatic pressing (HIP) method. In this method, the composition of the final product is adjusted by the relative proportion of the powders that will be blended by ball-milling. There are two different approaches in HIPing. The green sample, which was cold pressed, can be placed in a container (capsule) before HIPing [45, 46] or directly sintered without capsule wrapping [39]. The porosity of the final product is determined by the sintering temperature and time as well as the pressure of the Ar gas (Figure 2.22).
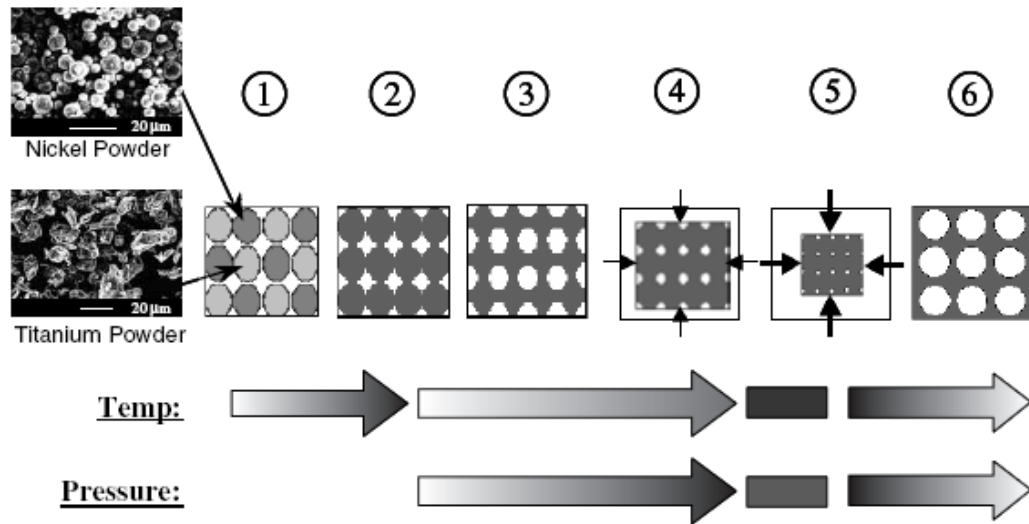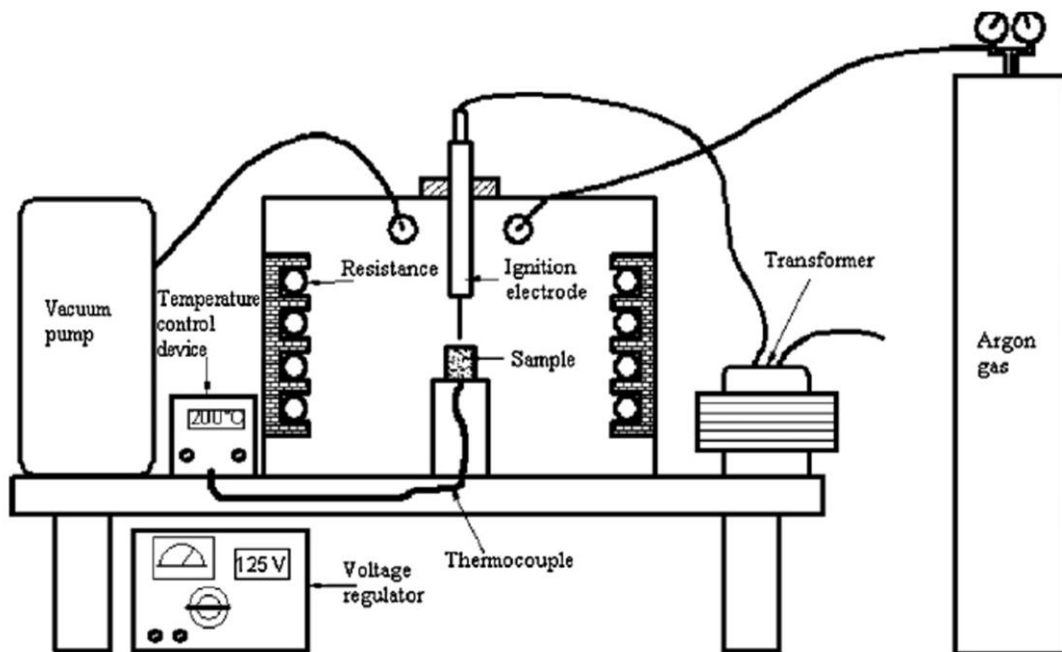
Figure 2.22 Schematical drawing of HIP process showing the steps of processing [46].

The isostatic conditions achievable by HIP in addition to the control of the geometry of the final product, which also enables to processes complex shaped products that are large in size, are the advantages of HIP. In addition, the porosity can be adjusted by varying the pressure of gas. However, the close control of pore size and distribution is a challenging process since there is a complex system which is also affected by sintering temperature and time. Moreover, secondary intermetallic formation also seems to be inevitable due to the use of elementary powders. Higher cycle cost of HIP system in combination with the requirement of suitable container design is another drawback of this method.

2.3.1.2. Self-Propagating High-Temperature Synthesis

Self-propagating high-temperature synthesis (SHS) method, which is also called as ignition or combustion synthesis, is based on the exothermic reaction of Ti with Ni. If an ignition is induced to the powders of Ti and Ni, a self-sustaining combustion reaction will take place. Accordingly, elementary powders are used for this method. As in the case of HIP, powders are mixed by ball-milling before cold-pressing. In

order to achieve the self-sustaining conditions, the green compacts are preheated to a determined temperature under protective gas, which is generally Argon. The ignition required to start the reaction was supplied by the electrical discharge pulse with the help of a coil attached to the one end of the specimen. Upon ignition, sintering takes place in a very short time by the combustion waves propagating along the specimen. The sintering is also takes place under protective gas atmosphere [41]. Schematical drawing of SHS device is given in Figure 2.23.

Figure 2.23 Schematical drawing of SHS device [47].

The main advantage of this method is obviously the ability to rapid processing of TiNi foams. However, the formation of secondary intermetallics such as Ti_2Ni, $TiNi_3$, etc., which degrades the mechanical properties, is inevitable for this method. In addition, the pores are longitudinal in shape as a result of the directionality of the propagated combustion wave front (Figure 2.24) causing inhomogeneity of the porosity. Although high porosity levels can be attained by this method, most of the

pores are not interconnected [41, 48], which is a drawback for biomedical applications, since it prevents the transportation of body fluids and tissues.
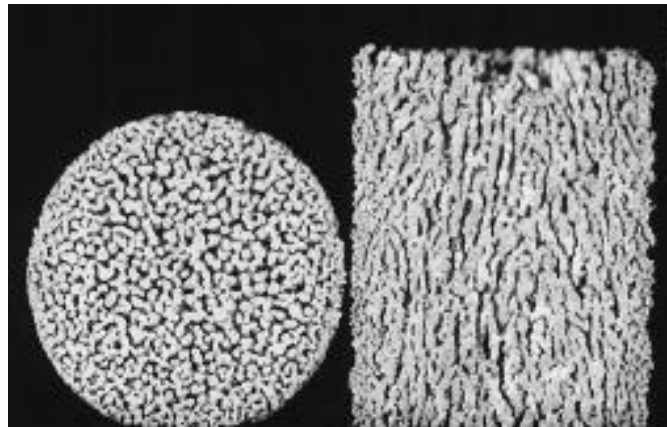
Figure 2.24 The pore shape and distribution of TiNi foam that was processed by SHS method (reproduced from [48])

2.3.1.3. Spark Plasma Sintering

Spark plasma sintering (Figure 2.25) is one of the methods in literature that was not gain much interest as a processing technique of porous TiNi alloys. Pre-alloyed powders, which were pressed in a graphite die, are heated by the application of a pulsed current to the die. Zhao *et al.* stated that sintering conditions maintained by this method shortens the sintering time besides resulting in better surface conditions [42]. However, it was obvious from the results presented in manuscript that the sintering was not homogeneous and achieved only at the edges of the specimen that is in contact with the die. Moreover the maximum porosity content that was achieved by this method was only 25 vol%.
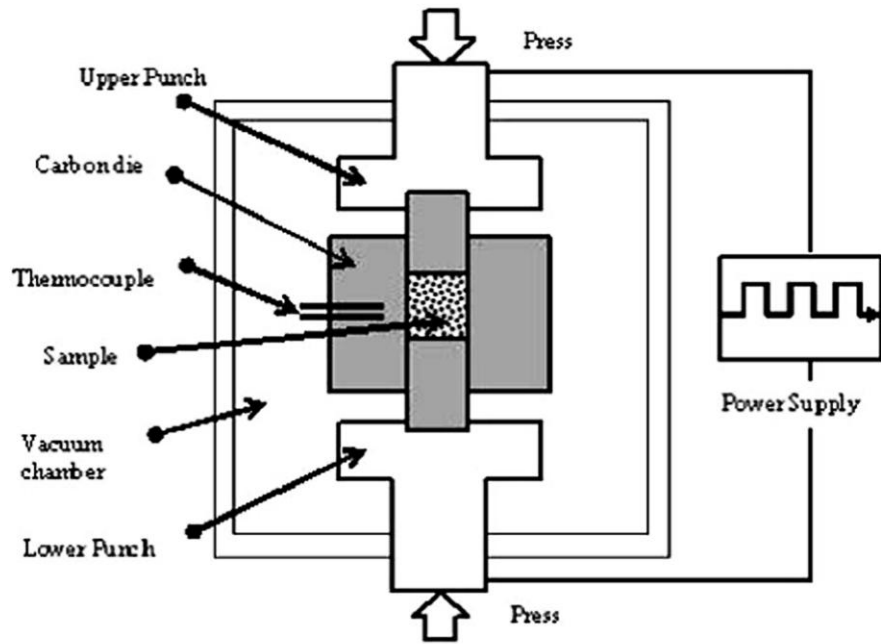
Figure 2.25 Schematical drawing of SPS device [42].

2.3.1.4 Metal Injection Molding

Metal injection molding (MIM) consists of mainly four steps; feedstock preparation, injection molding, binder removal, and sintering (Figure 2.26). Both elemental powders and prealloyed powders can be used for feedstock preparation. If elemental powders are used, they are ball-milled before the addition of the binder mixture, which will be removed by heating the injection molded sample. Sintering can be performed at atmosphere controlled furnaces as well as SHS method [49].
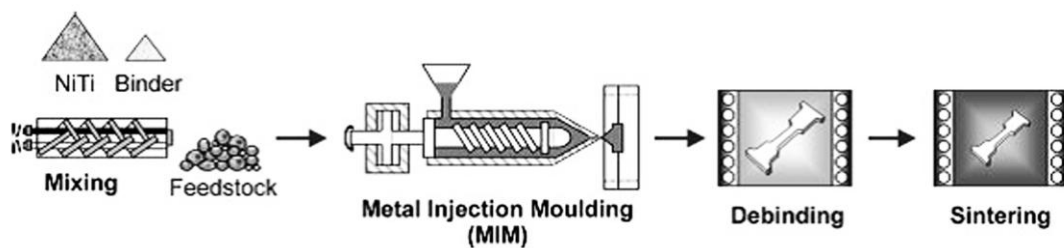
Figure 2.26 Schematic drawing of MIM process [50].

The main advantage of MIM is to process complex shaped products with high rate of production. When the porous TiNi alloys were considered, however, only simple shaped products were found in literature. Accordingly, MIM process was not seem to add any benefits on SHS or sintering with space holder techniques, especially the additional steps such as binder removal and injection molding, included by this process.

2.3.1.5. Conventional Sintering

Conventional sintering (CS) technique, which is widely employed in powder metallurgy, is not a preferred method in porous TiNi alloy processing due to both higher oxygen affinity of Ti, which prevents sintering at elevated temperatures, and lower porosity content that can be obtained by this method. Lower sintering temperatures result in degraded mechanical properties even at low porosity content [51]. Elementary powders are used for this method, which is another drawback since secondary intermetallic formation becomes unavoidable [52].

On the other hand, Bertheville *et.al.* has processed porous TiNi alloys with CS method in a similar way to the space holder technique [53]. They used TiH_2 and Ni powders instead of Ti and Ni to promote pore formation by decomposition of TiH_2 during sintering. However, the above mentioned problems cannot be overcome.

2.3.1.6. Sintering with Space Holder

Sintering with space holder technique is in fact the addition of space holder material to the powder mixture before sintering by one of the above mentioned processing methods. As an example, Wu *et al.* have added NH_4HCO_3 as space holder material after ball-milling of Ti and Ni powders and remove the space holder from the green compact by sintering in tube furnace before HIPing [38]. In addition, Bansiddhi *et al.* has mixed NaF and prealloyed TiNi powders before HIPing [54]. Another sintering with space holder technique was reported by Li et.al. for low pressure

sintering of elemental powders with the addition of $TiH_{1.5}$ as space holder [44]. On the other hand, Bram *et.al.* added NaCl space holders to the feedstock in their research on processing highly porous TiNi with MIM [43]. The space holder was also removed during debinding step before sintering under vacuum atmosphere. The space holder can be removed from the sample during or after sintering either by evaporation or chemical dissolution.

Among the aforementioned methods, pore size and distribution can be controlled more closely and easily by sintering with space holder technique. The selection of the space holder material directly affects the properties of TiNi foam since the size and shape of the macropores created after sintering is determined by that of space holder material. On the other hand, the contamination of TiNi, which will result in degradation of mechanical properties, is also possible due to the reaction of TiNi with space holder or the solution that is used for removal of space holder material if present. When the space holder materials reported in literature was analyzed, magnesium was found to offer many advantages over other space holder materials because of its relatively low boiling temperature that enabled the rapid removal of space holder during sintering [55]. In addition, being highly affinitive to oxygen, magnesium vapor had prevented the oxidation of titanium during sintering.

There are several advantages of sintering with space holder technique such as close control of size and distribution of porosity, ability to obtain high open-porosity content, as mentioned above. However, the main drawback of this method is the lack of batch processing.

2.3.2. Characteristics of Porous TiNi Alloys Processed with Different Techniques

There are several characterization methods applied to foams: particle size distribution (PSD), differential scanning calorimetry (DSC), scanning electron microscopy (SEM), X-ray diffraction (XRD), mechanical testing, and porosity

measurements like Archimedes', mercury porosimetry, etc. The common characteristics of TiNi foams processed with different techniques are summarized in this part.

2.3.2.1. HIP Technique

Elemental powders are generally preferred for this technique as mentioned before. Accordingly powder size gains importance since it determines the diffusion distance of Ti and Ni. There are two general approaches in literature in terms of powder size determination. The first one is to use Ti and Ni powders with similar size while the second one is to employ relatively larger sized Ti powders (50-75 μm) in combination with very low sized Ni powders (4-7 μm) [39,44,46,51]. Whatever the approach is the formation of secondary intermetallics such as Ti_2Ni and $TiNi_3$ cannot be avoided for the reported sintering temperatures and times. Moreover, residual Ti and Ni regions were also reported by Lagoudas and Vandygriff [46]. Another approach was reported by Greiner *et.al.* that they have employed prealloyed TiNi powder in combination with Ni powders to obtain higher Ni content [56]. However, no data was reported on the phase analysis of the processed Ti-51 at%Ni foams.

The porosity values obtained by this technique display a wide distribution in the range of 0.6-53.3 vol% depending mainly on the pressure applied during processing. Accordingly, the mechanical behavior, which was determined by compression tests, also varies in a wide range. The lowest porosity range (0.6-18.8), which was reported by Greiner *et.al.*, results in higher strength and stiffness as expected [56]. The as-processed Ti-51 at%Ni foams with 16% porosity display an elastic modulus of 24 GPa, yield strength of 450 MPa while aging at 400 °C for 4 hours result in a decrease of both properties (E = 15 GPa, σ_y = 300 MPa). The recoverable strain values obtained from compressive superelasticity tests were also outstanding due to lower porosity content. It was reported that 6.8 % strain was recovered when TiNi foam with 16 % porosity (aged at 400 °C for 4 hours) was subjected to a maximum

strain of 11 % at a stress level of 980 MPa. On the other hand, TiNi foams with porosity contents in the range of 42-50 vol% displays 3.25-3.4% recovery when subjected to 4% maximum strain at corresponding stress levels in the range of 110-245 MPa [44, 46].

Another mechanical characterization method reported in literature for HIP processed TiNi foams is the impact loading test, which was applied with split Hopkinson bar apparatus at 298 K [46]. Lagoudas and Vandygriff reported that Ti-50.6 at%Ni foams with 42 vol% porosity displays a 4% superelastic recovery in addition to 3-6% shape memory for the maximum strain values varies in the range of 8-17%.

2.3.2.2. SHS Technique

Elementary powders are used for processing TiNi foams with this technique to obtain the exothermal reaction. The powder size is extremely important for this technique since it determines the diffusion distance to maintain homogeneous structure. The powder sizes given in literature displays a wide distribution in the range of 15-75 μm for Ti powders and 4-44 μm for Ni powders [47, 48, 57-61]. However, the formation of secondary intermetallics seems such as $TiNi_3$, Ti_2Ni, and Ti_3Ni_4 to be inevitable even powders with average particle size of 15.2 and 18 μm are used for Ti and Ni respectively [48,59]. The general aim in literature is to mix powders in equiatomic ratio so the processed TiNi foams generally contain both B2 and B19' at room temperature as revealed by both XRD and DSC analyses [47, 48, 57-61].

On the other hand, porosity values obtained with this technique varies in the range of 42-68 vol% depending on the preheating temperature. However, Zhang *et.al.* reported that Ti-50.8 at%Ni foams, which were processed with SHS, have 27 vol% porosity [58]. They have also applied compression superelasticity tests on heat treated (450 °C, 0.5 h) TiNi foams and measured a maximum of 6.8% strain recovery when the foams were loaded upto 8% maximum strain. On the contrary,

Guo *et al.* reported higher superelastic recovery values for Ti-50 at%Ni foams with 64 vol% porosity [61]. They have conducted compression superelasticity tests at three different temperatures and concluded that increasing temperature above A_f results in higher recoverable strain values due to the change of phase constituents. Although they have reported as high as 9.5 % strain recovery for the specimen that was loaded up to 11 % maximum strain, the maximum strength values attained (98 MPa) were very low compared with the results (maximum compressive strength of 890 MPa) reported by Zhang *et.al*.

The mechanical behavior of TiNi foams that are in as-sintered condition is also generally determined by compression tests. The reported data on monotonic compression behavior of TiNi foams processed with this technique is limited since the general aim is to characterize the superelasticity. The most detailed study on monotonic mechanical characterization of these foams is given by Sevilla *et.al.* [57]. They have reported that Ti-50 at%Ni foams with porosity in the range of 63-68 have elastic modulus of 1.21 GPa, compressive yield strength of 101.3 MPa, and maximum compressive strength of 142.5 MPa while they displayed 171.3 MPa yield and 192.3 MPa maximum strength when subjected to bending. They have also reported on fatigue behavior under compression, which is quite scarce in literature. The compression fatigue tests were conducted at 310 K in a simulated body fluid environment with a frequency of 2 Hz and it was found that the endurance limit, which was determined at the end of 10^8 cycles, of these foams is 7.5 MPa. On the other hand, Guo *et.al* also reported that they have conducted low-frequency fatigue tests under compression at 293 K [61]. However, the so-called fatigue tests, which were conducted by a frequency of 1 Hz within the interval of 12-120 MPa compressive stress, actually reflects the long term superelastic behavior since only the strain recovered at the end of 180 cycle of deformation was measured instead of an endurance limit.

2.3.2.3. SPS Technique

There is only one study that can be found in literature on this processing technique. Zhao *et.al.* employed prealloyed Ti-50.9 at%Ni powders with the average size of 150 μm for processing TiNi foams with two different porosity contents as 13 and 25 vol%. The processed foams were heat treated at 320 °C for 30 min before characterization by compression tests. There is no data on phase analyses of processed and/or heat treated foams but from the combined analyses of composition with given DSC results, B2, B19' and other secondary intermetallic phases need to be present since the transformation temperatures are very high for TiNi with 50.9 at%Ni content. The elastic modulus and yield strength values of TiNi foams with 13 vol% porosity, which were obtained from the given graphical data of superelasticity tests, are 25 GPa and 300 MPa at 298 K while 35 GPa and 350 MPa at 331 K, which is ~20 K above A_f. These foams have fully recovered 5.4 % maximum strain applied at 700 MPa. The maximum strain and correspondingly recovered strain (the maximum applied strain fully recovered) decreased to 4.6 % when deformation applied at 331 K although the test conducted at 925 MPa maximum stress. On the other hand, TiNi foam with 25 vol% porosity displayed 7.5 GPa elastic modulus and 120 MPa yield strength at 298 K. The superelasticity test of TiNi foams with 25 vol% porosity only conducted at 298 K and 2.1% full recovery was attained at 160 MPa. The superelastic recovery values are low when compared to TiNi foams with similar low porosity content (16 vol%) that was processed by HIP technique [56].

2.3.2.4. MIM Technique

There are also limited studies on processing of porous TiNi by MIM. Accordingly, characterization of these foams is limited in literature. Guoxin *et al.* reported that they have processed Ti-50 at%Ni foams with 75 vol% porosity from elemental powders [49]. However, the characterization methods employed includes density measurement, XRD and SEM, which indicates the presence of B2, B19' and Ti_2Ni phases for TiNi foams with pore size distribution up to 1370 μm.

On the other hand, Ismail *et.al.* processed Ti-50.9 at%Ni foams with varying porosity contents in the range of 39.4-42.5 vol% [62]. They have reported that B2, B19', Ti_3Ni_4, Ti_2Ni and/or $Ti_4Ni_2O_x$ phases are present in processed TiNi foams. One of the reasons behind the presence of higher amount of secondary intermetallics and/or oxide phase will be the larger particle size employed in this study. On the contrary to the previous study [49], at which Ti and Ni powders with 3 and 2 μm average sizes respectively are used, Ismail et. al. employed Ti and Ni powders with 32 and 15 μm respectively.

Ti-50.9 at%Ni foams were mechanically characterized with compressive superelasticity tests in combination with the analyses of shape memory affect by heating the specimen after unloading. Accordingly it was found that TiNi foams with 39.4 vol% porosity can recover maximum 7 % strain when it was subjected to 14 % maximum strain. In addition, 3.64 % strain can be recovered by shape memory affect leading to 3.36 % residual deformation. The strain recovered by superelasticity and shape memory for TiNi foams with 39.8 vol% porosity was reported as 7 and 3.64% respectively while the same values that was measured for TiNi foams with 42.5 vol% porosity was 8.12 and 2.8% respectively. The corresponding stress level at 14% deformation was given only for TiNi foam with 42.5 vol% porosity as ~350 MPa. Accordingly, it can be said that the superelasticity values obtained by this method are promising when the porosity content is considered. However, it is obvious that the formation of secondary intermetallics needs to be prevented to obtain better results.

2.3.2.5. CS Technique

As in the case of HIP and SHS, elemental powders are generally used for processing TiNi foams with conventional sintering. The average powder sizes display a wide distribution between 4-75 μm. The sintering was generally conducted under either vacuum or protective gas atmosphere to prevent oxidation. Argon gas was the generally used protective gas but Bertheville used Ca vapor in combination with Ar

gas during both dehydrogenation of TiH_2 powder, which was used instead of Ti powder, and sintering in his research [53, 63]. However, he was reported that CaO was formed on the surface of TiNi foam. Another study of Berteaville on sintering TiNi foams under vacuum from TiH_2 and Ni powders include also HIP after sintering [53]. The porosity content of TiNi foams were decreased from 29-34 to 7 vol% after HIPing. On the other hand, XRD results of sintered and heat treated (500 °C for 1 h) TiNi foams indicate the presence of B2, Ti_3Ni_4, $TiNi_3$, $Ti_4Ni_2O_x$, Ni, and even $TiC_{0.7}N_{0.3}$ although the powder sizes of TiH_2 and Ni were decreased to 6.97 and 6.35, respectively. Post-HIP process only eliminates the presence of Ni. Bertheville *et.al.* use constant load shape memory tests to characterize the processed and heat treated TiNi foams. The shape memory behavior was characterized by the application of tension load to the sample at a temperature above A_f and monitoring the change of strain by altering temperature. Accordingly, they have found that both the conventionally sintered and HIPed TiNi foams display 1.6 % recovery under the tensional stress of 120 MPa after the heat treatment.

The researches on conventional sintering of TiNi foams from elemental Ti and Ni powders reported porosity contents in the range of 33-45 vol% [10, 44, 51, 52]. Among TiNi foams with different compositions, which were processed with different sintering parameters, the most promising result was reported by Yuan *et.al.* for Ti-50.8 at%Ni foams with 43 vol% porosity [51]. They reported that these foams, which have elastic modulus of 4 GPa, display 3.2 % strain recovery when loaded up to 4 % maximum strain. Accordingly, it is obvious that superelasticity of conventionally sintered TiNi foams is not good enough to compete with that of TiNi foams processed with other techniques. However, Zhu *et.al.* reported that they measured a compressive yield strength of 685 MPa and flexural yield strength of 300 MPa for Ti-50 at%Ni foams with 45 vol% porosity [52]. Although being promise in terms of monotonic mechanical behavior, no data was presented on superelasticity of the processed TiNi foams, which also contain secondary phases as $TiNi_3$ and Ti_2Ni in addition to residual Ni.

Another method for conventional sintering, which was applied by Tang *et.al.* for processing Ti-50 at%Ni alloys from elemental powders with maximum sizes of 44 and 74 for TiNi respectively, is microwave sintering [64]. TiNi foams with varying porosity contents in the range of 27-48 vol% were heat treated at 450 °C for 30 min after sintering under Ar gas atmosphere. XRD analyses results given in study indicated that presence of $TiNi_3$ and Ti_2Ni phases cannot be avoided. Among TiNi foams sintered at different temperatures, the optimum mechanical results were obtained by sintering at 900 °C for 1 h. The compression superelasticity tests, which were conducted by loading up to 200 MPa and full unloading, revealed that 8.6% maximum recovery was measured for 9 % maximum strain applied while the maximum applied and recovered strain value decreased to 6.5 after third cycle of loading-unloading. The superelastic recovery values are promising but considering that TiNi foam, which was sintered at 900 °C for 1 h, has a porosity content of 37.9 vol%, the maximum strength that can be achieved seems to be low compared to other methods such as SHS, HIP, etc.

2.3.2.6. Space Holder Technique

Both elemental and prealloyed powders are used for processing TiNi alloys with this technique [10, 38, 43, 65-71]. There are several space holder materials in literature as urea (CH_4N_2O), ammonium bicarbonate (NH_4HCO_3), sodium chloride (NaCl), sodium fluoride (NaF), titanium hydride (TiH_2), steel, and magnesium. The most extensive work on space holder technique in literature is reported on sintering under vacuum or argon gas atmosphere. The size of space holder material, which strongly affects the final pore size, changes in the range of 200-900 μm except in the case of TiH_2. Rong and Li have employed TiH_2 powders with maximum diameter of 44 μm to process TiNi foams with 30-40 vol% porosity. Since all reported work on conventional sintering of TiNi foams with space holder technique was conducted by elementary powders, TiNi foams with porosity in the range of 23-87 vol%, consist of secondary intermetallics as well as residual Ti and Ni depending on the processing parameters and/or Ti and Ni powder sizes. The only exception is the

magnesium space holder technique, which employs prealloyed powders [55, 72]. Among these techniques, the maximum porosity content reported by Xiong *et.al.* as 87 vol% for Ti-50.5 at%Ni foams, which was sintered under vacuum with ammonium bicarbonate as space holder [71]. However, the monotonic compression test results indicate that the foams with porosity contents in the range of 71-87 have very low compressive strengths and elastic moduli values due to their high porosities. However, the measured strain values, which were recovered by superelasticity and shape memory under 7% maximum applied strain are promising since maximum total recovery of 6.3% strain could be achieved.

When the results of several studies reported in literature were investigated, it was observed that porosity contents generally vary in the range of 35-50 vol%. When the mechanical properties obtained from these studies were investigated, it was found that the sintering with magnesium space holder technique is the most promising one.

Other sintering methods that are applied together with space holder technique are HIP, MIM and hot pressing. Both prealloyed and elemental powders were employed in sintering of TiNi foams by HIP technique. Among these works, Bansiddhi and Dunand reported that Ti-50 at%Ni foams with 19.6 and 39.5 vol% porosity contents were processed by NaF space holder [67]. They have conducted compression tests on heat treated (160 °C for 5 min) TiNi foams and measured elastic moduli as 15 and 6.5 GPa, maximum compressive strength as 482 and 135 MPa for 19.6 vol% and 39.5 vol% porosity contents, respectively. Also TiNi foams with 19.6 vol% displayed superelastic recovery of 3% and shape memory recovery of 2.2% when they have been subjected to 8% of maximum deformation. On the other hand, TiNi foams with 39.5 vol% recovered only 1.3% strain by superelasticity and 3.46% strain by shape memory when subjected to 6% maximum strain. Another study on space holder technique with HIP sintering was conducted by Wu *et.al.* to process Ti-50 at%Ni foams with porosity content varying in the range of 21-48 vol% [38]. They have employed ammonium bicarbonate as space holder and heat treated (450 °C for 30 min) TiNi foams before characterization for compressive behavior.

The elastic moduli of TiNi foams were found to change in the range of 6.3 to 9.7 GPa with varying porosity content. On the other hand, maximum recovered strain was measured as 4.3% for TiNi foam with 21 vol% porosity at the end of five cycles of training at 410 MPa. When compared with the results obtained by Bansiddhi and Dunand, the mechanical tests results obtained by Wu *et.al.* are seemed to be more promising.

MIM, which is another method of sintering for space holder technique, was applied by Bram *et.al.* [43]. They have used prealloyed TiNi powders in combination with NaCl as space holder material. They have applied heat treatment at 500 °C for 2 h after sintering to remove the binder system, which is composed of amide wax and polyethylene. However, XRD results indicate the presence of secondary intermetallic (TiNİ$_3$), oxide phase (Ti$_4$Ni$_2$O$_x$), and carbide phase (TiC). Moreover, the compressive yield strength measured as 80 MPa at 310 K, is low for TiNi foam with 51.4 vol% porosity. On the other hand, the superelastic recovery is also not promising since maximum recovered strain was measured as 6.7% when TiNi foam was subjected to a strain as high as 30%. Moreover, they have found that the superelastic recovery decreases to 1% when TiNi foam was subjected to cyclic loading of 4% maximum strain for 230000 cycles with a frequency of 1 Hz. Another interesting research on processing TiNi foams with space holder technique was employing steel meshes as space holder [70]. The sintering was done by hot-pressing of TiNi powders and steel mesh. The resultant pore structure was two-dimensional network as expected and porosity contents (23.7 and 33.5 vol%) obtained by this method is low. Although having low porosity content, only a maximum of 100 MPa compressive yield strength can be achieved for TiNi foam with 23.7 vol% porosity. On the other hand, the maximum strain recovered by superelasticity and shape memory was determined as 2 and 3.6% respectively for TiNi foam with 23.7 vol% porosity while 2.3 and 3.2% respectively for TiNi foam with 33.5 vol% porosity when the foams were subjected to maximum applied strain of 6%.

2.3.3. Fatigue of Porous Metals

As it can be seen above, porous TiNi alloys have been widely characterized in terms of their various mechanical properties; however, their fatigue properties have not been well studied, even though, the strength of the materials decrease by the formation and development of small cracks due to cyclic loading. As well as the amount and direction of loading, the material properties like the pore ratio, the amount of sintering and the orientation of the cell walls to direction of loading affects the amount of this decline. Although there are researches on the fatigue life determination of bulk TiNi alloys under different loading systems [73-75], the fatigue tests of porous metals are concentrated on aluminum alloys [76, 77-80].
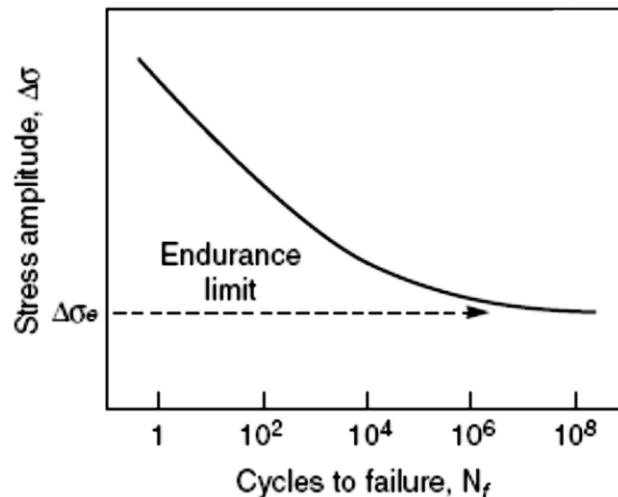
Figure 2.27 Typical S-N graph indicating the fatigue limit [80].

Similar to the bulk metals, fatigue characterization of porous metals can be performed under different loading systems such as tension-tension, compression-compression, tension-compression, etc. considering the requirements of application field. The general approach in fatigue characterization of porous metals is the determination of maximum applied load as a proportion of yield strength of the material since this practice makes it possible to compare the fatigue limits of

different materials. Accordingly, fatigue limit is generally determined by testing the porous metal with maximum loads in the interval of $0.5\sigma_y \leq \sigma_{max} \leq \sigma_y$ and obtaining a graph similar to that given in Figure 2.27. The ratio of minimum load to the maximum load, R, is generally taken to be 0.1 for porous materials in the literature to prevent the formation of stepwise failure due to overloading.

The deformation of porous metals during fatigue testing generally displays three stages of deformation [76, 77, 81]. Inelastic strains (Stage I) observed initially are followed by the accumulation of the minimal strains (Stage II), which displays a plateau in strain versus number of cycles diagram, leading to the sudden failure when critical number of cycles was attained (Stage III). Another important point in characterization of fatigue behavior is the determination of fatigue life. The determination of fatigue life is easier under tension-tension loading since porous metal was observed to be failed by the formation of a macroscopic crack after some plastic deformation (Figure 2.28). Accordingly, the failure of the specimen is the general criterion that is used in determination of fatigue life during tension-tension fatigue tests.
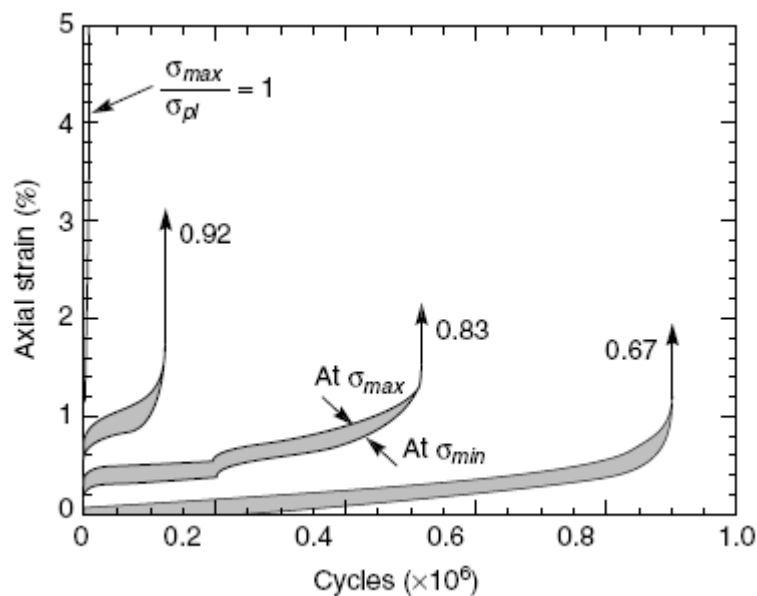
Figure 2.28 The results of tension-tension fatigue tests applied on Alporas foams [80].

On the other hand, several cracks were observed to be formed at the walls of pores leading to collapse of the structure during compression-compression tests. As a result, different deformation behaviors can be observed during compressive-compressive fatigue tests as given in Figure 2.29. Consequently, there are several criteria reported in literature to evaluate the fatigue life as knee-formation point [77], the failure of the specimen [73] or the point where a certain percentage of overall deformation has been observed [82].
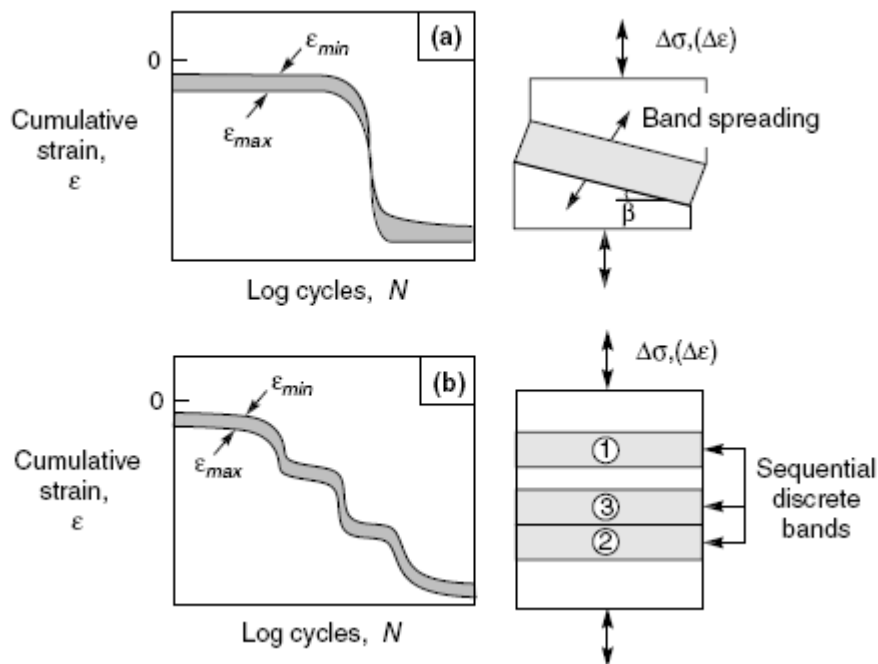
Figure 2.29 Commonly observed failure types of porous metals under compression-compression fatigue: (a) spreading of a single deformation band, (b) formation of multiple deformation bands [80].

There are very limited studies on fatigue-life estimation of porous TiNi alloys in literature. The studies conducted by Barrabes *et.al.* and Sevilla *et.al.* are the only researches that can be found in literature other that this study. They have employed compression-compression testing, which is the most commonly preferred type of

loading in fatigue analysis of porous metals, to find fatigue life of TiNi foams with porosities in the range of 62-68% [82, 83].

CHAPTER 3

# EXPERIMENTAL PROCEDURE

3.1. Powders Used

In the present study, spherical Ni-rich TiNi powder (Ti-50.8 at%Ni, 99.9% purity, Nanoval GmbH & Co. KG, Berlin, Germany) was used as the raw material for TiNi foam production. Prealloyed powder was used to prevent the formation of secondary intermetallics such as Ti_2Ni and $TiNi_3$, which degrades the mechanical properties.

Magnesium (99.82% purity, TangShanWeiHao Magnesium Powder Co. LTD., Tangshan, Hebei Province, China), was selected as the space holder material due to its higher oxygen affinity, which prevents the oxidation of TiNi during sintering, in addition to its lower boiling point than the melting point of TiNi that enables to obtain sintered and porous structure with a single step processing. Moreover, Mg has negligible solubility in both Ti and Ni. As the size of the magnesium powders determines the final pore size achieved, it was sieved to a particle size range of 250-600 μm that yields pore sizes suitable for biomedical applications.

All of the powders used in this research were processed by gas atomization technique and have displayed Gaussian distributions as given in Figure 3.1. The average particle sizes were found to be ~19 and ~357 μm for Ti-50.8 at%Ni and Mg powders, respectively. The spherical shape of the powders as well as the dendritic structure formed as the result of gas atomization process could be observed in scanning electron microscope (SEM) (JSM 6400, Jeol LTD, Tokyo, Japan) micrographs that are given in Figure 3.2.
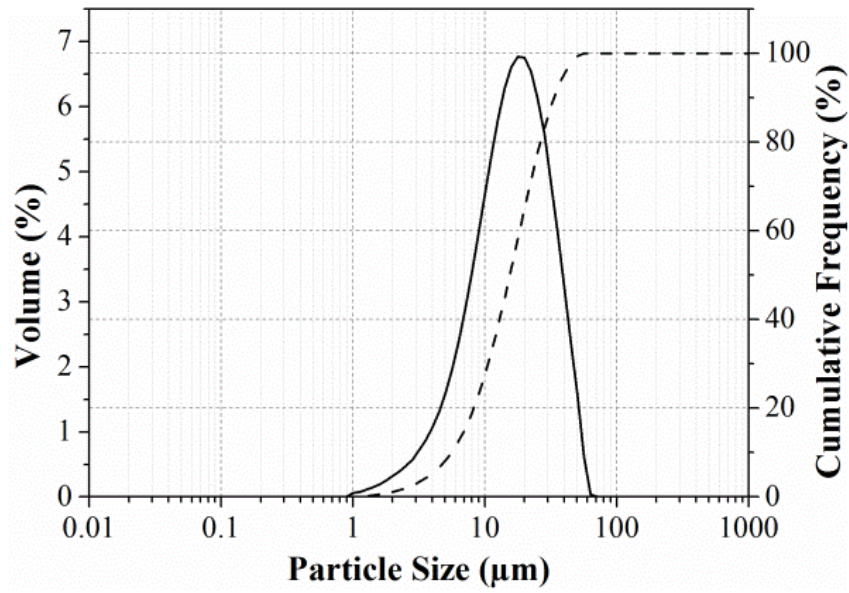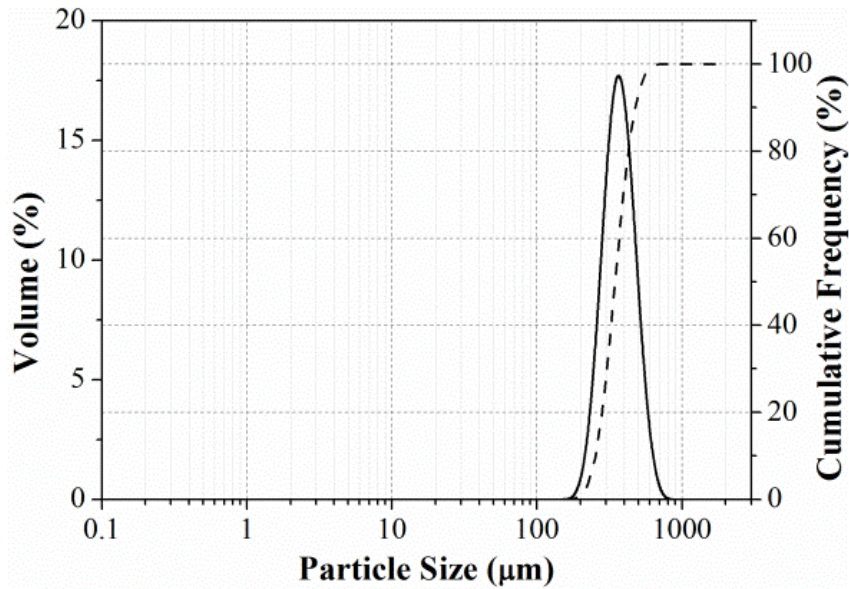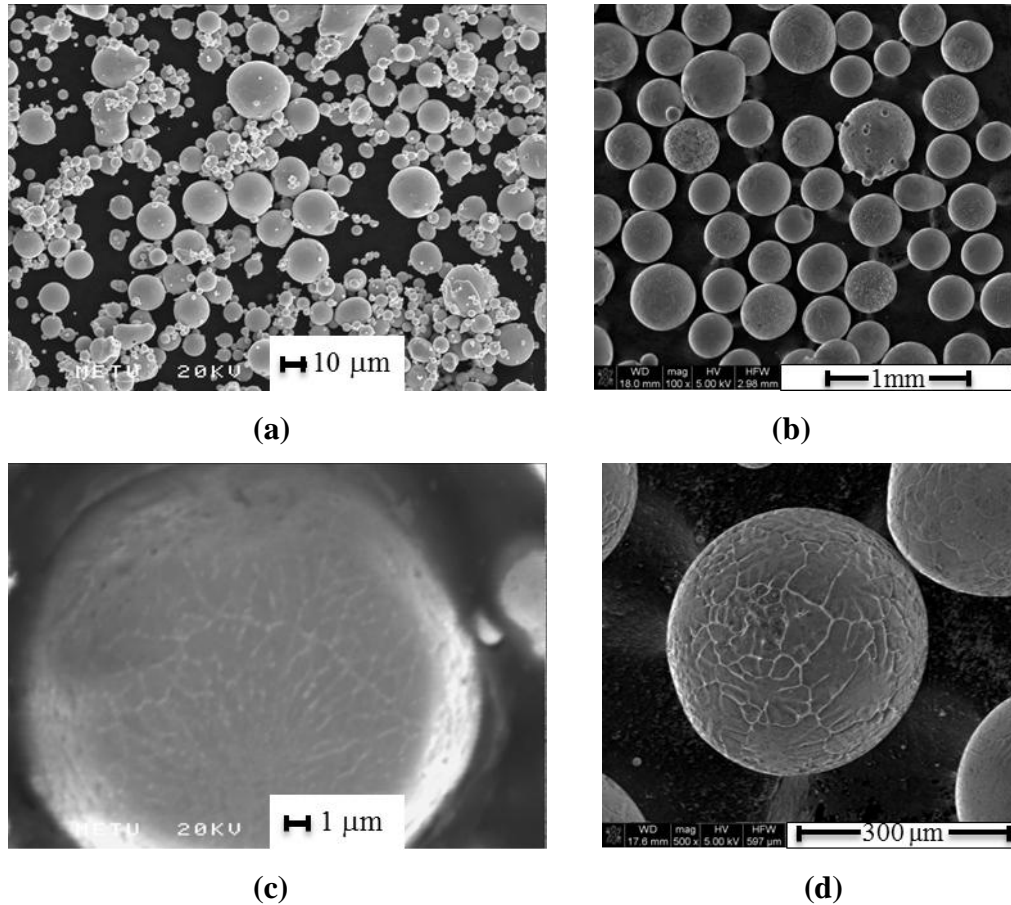
Figure 3.1 Particle size distributions of (a) Ti-50.8 at%Ni, (b) Mg powders (Solid lines represent the particle distribution while the dashed lines display cumulative distribution.).

(a)

(b)

(c)

(d)

Figure 3.2 SEM micrographs revealing the morphology and the dendritic microstructure of (a) and (c) Ti-50.8 at%Ni, (b) and (d) Mg powders.

The transformation temperature of Ti-50.8 at%Ni powder was determined by Perkin Elmer DSC 8000 Differential Scanning Calorimeter (DSC) with 10°C/min heating and cooling rates. As it was given in Figure 3.3, austenite start (A_s), austenite finish (A_f), martensite start (M_s) and martensite finish (M_f) temperatures were measured to be -30°C, 15°C, -28°C and -8°C, respectively.

The double peak (which were indicated by the arrows in Figure 3.3) observed during martensitic transformation, although seems to indicate R-transformation, was attributed to the inhomogeneity in the composition of the powders as a consequence of rapid cooling during gas atomization process since R-transformation could only be observed in TiNi alloys that have aged or alloyed with tertiary elements [5]. This

prediction was corroborated by the X-ray analysis results (Figure 3.4) that indicate the presence of only TiNi austenite peaks at room temperature.
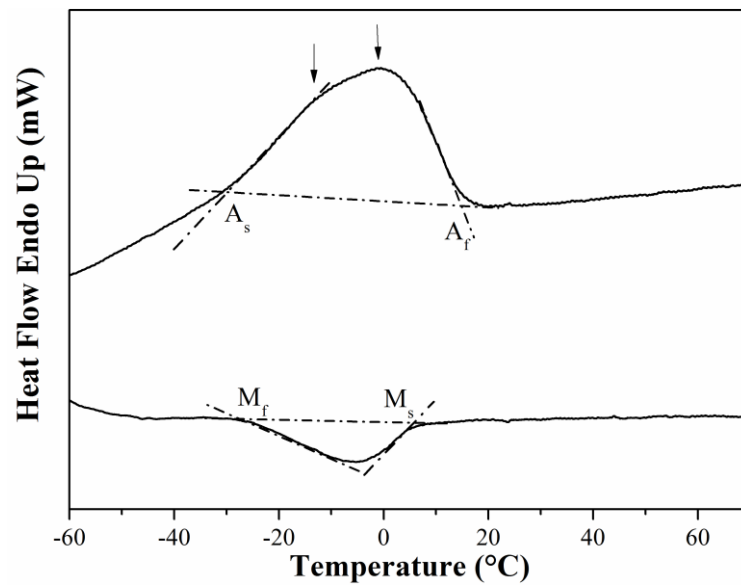

Figure 3.3 The result of differential scanning calorimetry measurement indicating the transformation temperatures of Ti-50.8 at%Ni powder.
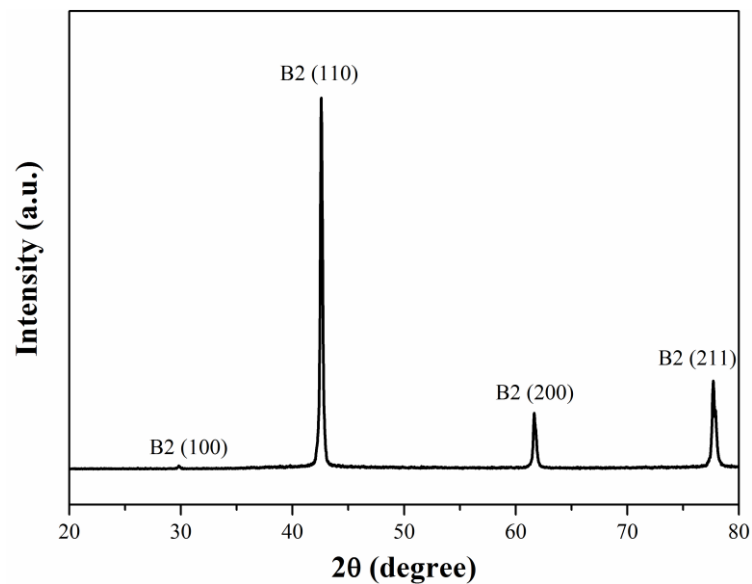
Figure 3.4 XRD analysis of prealloyed Ti-50.8 at%Ni powders.

3.2. Processing of Porous TiNi Alloys

Conventional sintering with space holder technique was applied for the processing of the porous TiNi alloys. The porosity of TiNi alloys was adjusted by varying the amount of magnesium powder mixed with TiNi powder. TiNi and magnesium powders were blended in the presence of 5 wt% polyvinyl alcohol solution (2.5 wt% PVA+ distilled water) as binder, prior to compaction via hydraulic press under 400 MPa pressure. PVA was chosen as binder among other chemical substances such as methyl cellulose due to its lower viscosity and stickiness. The lower viscosity is important to assure mixing of particles homogeneously while the lower stickiness is important for reducing the friction between the compact and die wall. Zinc stearate powder was used as die lubricant during compression. Different concentrations of PVA and various compaction pressures were experienced till the optimum values were achieved. The amount of PVA added was adjusted to be the minimum enough to achieve homogeneous coverage of Mg powders with TiNi powders.

| (a) | (b) |
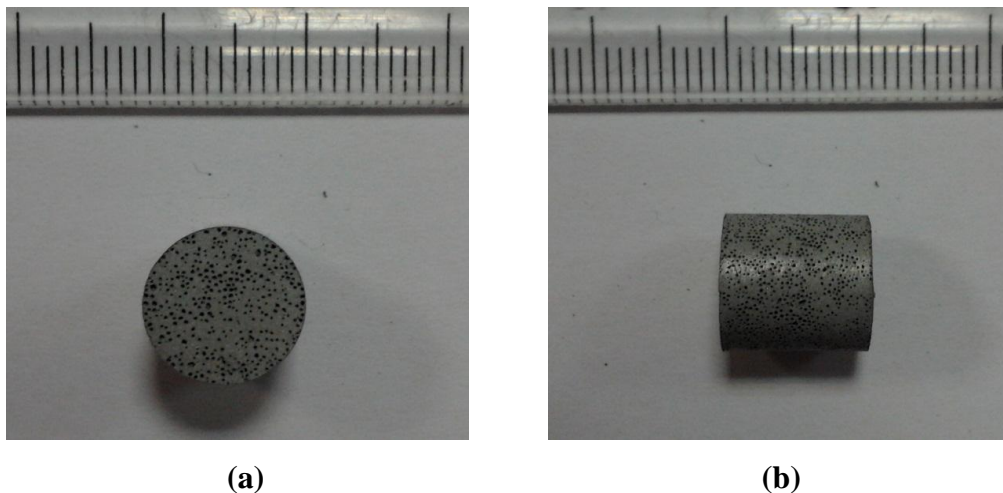
Figure 3.5 (a) Top and (b) side view of the processed TiNi foams.

Ti-50.8 at%Ni - Mg powder mixtures were pressed with a double-ended steel die to attain specimens having 10 mm diameter and aspect ratio of 1 (Figure 3.5).

Compaction pressure was optimized to obtain enough green strength without deforming Mg powders.

Despite the homogeneous distribution of the deformation applied, radial crack formation was observed during pressing of the powder mixtures (Figure 3.6). The effects of several parameters like the alignment of the press heads, the pressure applied, the amount of binder evaporated before compaction was checked and the reason of the crack formation was found to be something else: the superelasticity of Ti-50.8 at%Ni powder. It was observed that part of the deformation applied to the powder during compaction was recovered during the removal of the load. Consequently, the load application and removal rates were reduced to overcome the cracking problem.


Figure 3.6 The radial cracks formed vertical to the direction of pressing.

Due to the problems faced during the cold pressing using hydraulic press, alternative methods were also investigated. Among these, cold isostatic pressing was preferred due to more homogeneous deformation that could be attained. Silicon molds with different shore hardness values in the range of 30-70 were used for the compaction of TiNi powders under a hydrostatic pressure of 400 MPa. However, the required green strength could not be achieved due to the superelastic nature of the powders

used, despite the different binder types and mixing ratios examined. Consequently, hydraulic press was employed for powder compaction.

The compacts were sintered in an atmosphere controlled vertical tube furnace. High purity (99.999% purity, N_2: 6.2 vpm, O_2: 2.2 vpm, humidity: 2vpm) Argon gas was used for atmosphere control during sintering in order to prevent oxidation. Ti-6Al-4V crucibles which do not react with the magnesium vapor were used for suspending the specimen into the furnace without contacting the walls. Since TiNi compacts also react with Ti-6Al-4V, magnesia (MgO) pellets were placed in between the crucible and the specimen. These pellets were processed from MgO powders via compacting at 100 MPa followed by sintering at 1200 °C for 1 hour.

MgO was selected among other ceramic materials such as alumina titanate, mullite, etc. as the separator between TiNi and Ti-6Al-4V crucible since oxide of most ceramic compounds was reduced by Mg vapor causing the contamination of TiNi (Figure 3.7). As given in Figure 3.7 (a), when mullite was used as separator, TiNi foam was found to be coated in addition to the oxidation at the top surface and distortion at the bottom end. According to SEM analysis (Figure 3.7 (b) and (c)), a needle-like structure containing considerable amount of Al and Si was detected at the distorted region. It was considered that the reaction of Mg with mullite resulted in $MgAl_2O_4$ (spinel) formation, as evident from X-ray analysis of mullite (Figure 3.8), and caused the free Si to react with TiNi to form Ti-SiC structure. On the other hand, aluminum (Al) was detected due to the reduction of Al_2O_3 by Mg vapor followed by evaporation of Al due to the elevated temperature.
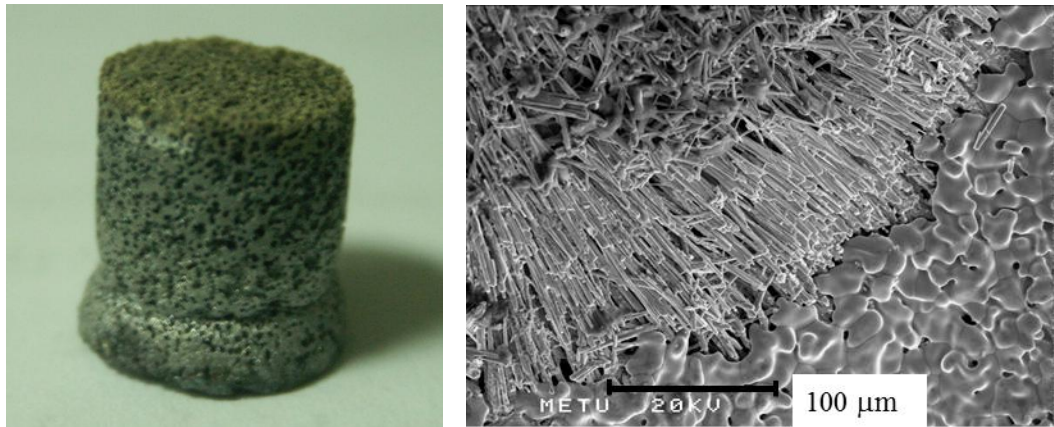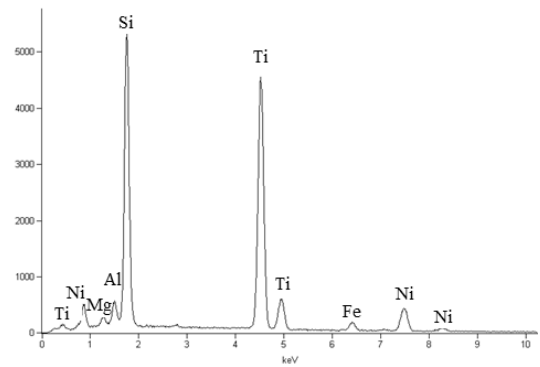
(a)   **(b)**
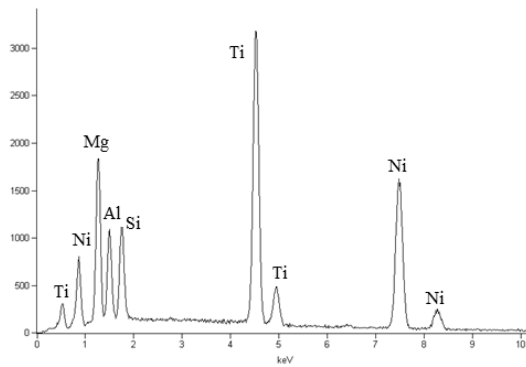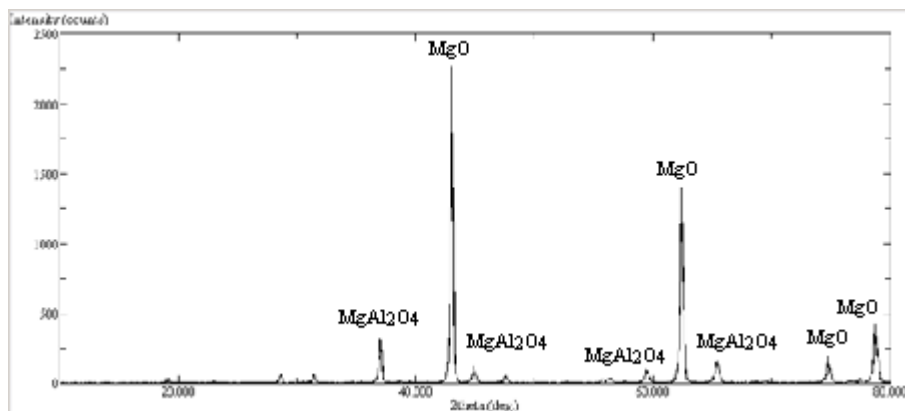


(c)   **(d)**

Figure 3.7 (a) TiNi foam processed using mullite, (b) SEM image of the coating layer formed at the bottom of the foam, EDS results of (c) coating layer, (d) region with needle-like structure.

Figure 3.8 XRD analysis of mullite pellet.

The lay-out of the crucible is given in Figure 3.9. As it is shown in the figure, a TiNi foam pellet was placed beneath the specimen to prevent the accumulation of molten Mg at the bottom of the compact. In addition, Ti-sponge particles were placed on top of the specimen to prevent the reaction of trace amount of oxygen, which is present in Ar, with specimen. Ti-sponge particles were placed on Ti-6Al-4V separator to inhibit the contact with TiNi.
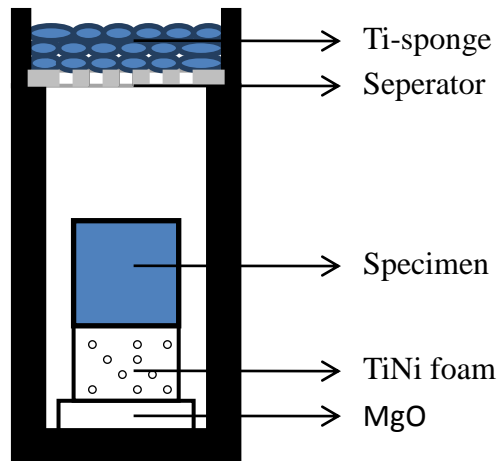

Figure 3.9 The schematic cross-sectional view of the crucible.

The amount of sintering before melting and evaporation of magnesium is of crucial importance for preventing the collapse of the structure. Therefore, powder compacts were sintered at 1200 °C for 2 hours subsequent to heating at a rate of 6.5 °C/min to assure sufficient sintering that would prevent the collapse of the compact upon melting and evaporation of magnesium. When the temperature exceeded 650 °C, the rate of oxygen removal in the chamber has increased by the melting of magnesium which gradually drains off the TiNi compacts. Oxygen that stem from argon gas as well as the oxide layers on the surface of the raw materials has been removed more effectively following the evaporation of magnesium at 1091 °C.

After lowering the specimen in hot zone of the furnace, it was purged with argon gas for 10 minutes to sweep away the oxygen in the furnace. Since continuous passage

of Ar gas during sintering would carry away the Mg vapor, which prevents the oxidation of the specimen, continuous Ar supply was interrupted after 10 minutes of purging by placing an oil bubbler in front of the furnace gateway as shown in Figure 3.10. By the application of this method, positive pressure was obtained without continuous gas flow and Ar entrance was observed only if there is a pressure drop in the furnace due to leakage.

Although it is well known that sintering ratio increases according to a power law t^n, where n is usually ½, with increasing time and exponentially with increasing temperature due to its diffusional nature, to examine their effect on the microstructure as well as mechanical behavior, sintering temperature and time were independently changed and Ti-50.8 at%Ni foams were also processed at 1250 °C for 2 hours and at 1200 °C for 4 hours.
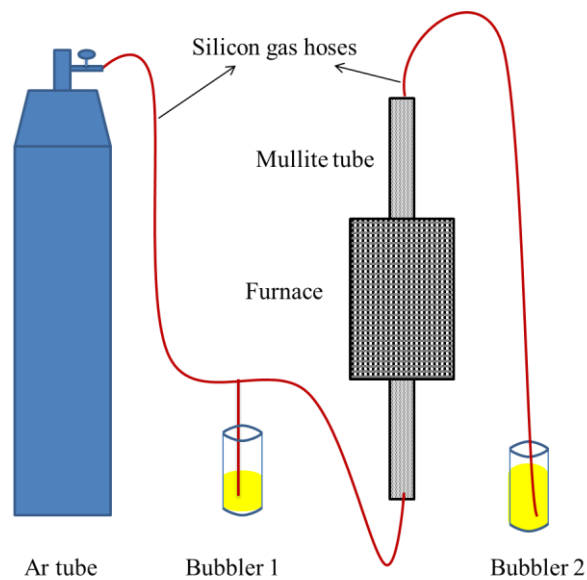
Figure 3.10 Schematic representation of the gas system used for processing porous TiNi specimens.

3.3. Heat Treatment

Although $TiNi_3$ is the only phase on Ni-rich side of Ti-Ni phase diagram that was in equilibrium with TiNi, there are intermediate phases that are observed upon aging of TiNi. Ti_3Ni_4 phase, on the contrary to being metastable, is the only precipitate observed under normal aging conditions, which leads to important contributions to transformation mechanisms and mechanical properties. Accordingly, a group of Ti-50.8 at%Ni foams were subjected to aging treatment after sintering.

TiNi foams were homogenized at 1000 °C for 15 minutes and quenched in water to assure fully austenitic microstructure before aging. Two different aging temperatures and times were applied on TiNi foams having 49 vol% porosity (Table 3.1). Since the aging temperatures are lower than the melting point of magnesium, the oxidation of TiNi was prevented via encapsulation of the foams in quartz tubes. Before sealing, the tubes were flushed with Ar and vacuumed with rotary pump repeatedly for 5 times to ensure the elimination of oxygen in the tube. Sealing was performed under vacuum. All of the foams were quenched in water after aging treatment. Quartz tube was broken with hammer after completion of aging treatment.

Table 3.1 Applied aging temperatures and times.

Temperature (°C)	Time (hours)	Temperature (°C)	Time (hours)
450	1.5	450	10
550	1.5	550	10

3.4. Characterization Studies

3.4.1. Particle Size Distribution

The particle size distribution of both Ti-50.8 at%Ni and Mg powders used was measured with Malvern Mastersizer 2000 Particle Size Distribution (PSD) Analyzer, which is capable of measuring particle sizes in the range of 0.02- 2000 μm with an accuracy of ± 1%. The operation principle of the analyzer is scattering of a laser beam, red laser (He-Ne) or blue light (solid-state light source), by the particles flowing through a cell. Since scattering occurs at an angle that is inversely proportional to their size, particle size distribution is measured from the angular intensities of transmitted and scattered light that is detected by multiple photosensitive detectors.

3.4.2. Density and Porosity Measurements

The density of the processed TiNi foams as well as their open and closed porosity contents were measured according to the Archimedes principle, which states that the weight of the displaced fluid by the immersed object is directly proportional to the volume of the displaced fluid. Precision balance (CP224S-0CE, Sartorius, Goettingen, Germany) equipped with a density measurement kit was employed for the measurements conducted by the procedure given below:

1. The processed foams were weighted (W_{dry}) and dipped to the xylene ($C_6H_4(CH_3)_2$) solution.
2. Vacuum was applied for 1.5 hours to the beakers containing TiNi in xylene solution to fill all the pores with xylene.
3. The measuring container of the density measurement kit was filled with xylene.
4. The weight of TiNi foams (W_{xyl}) was measured in the xylene solution while suspended.

5. Another weight measurement (W_{sol}) was applied to the foams after the excess xylene on them was wiped off.

The bulk density of TiNi foams was calculated according to Equation 3.1 where the density of xylene is 0.861 g/cm^3.

$$\frac{\rho_{foam}}{\rho_{xylene}} = \frac{W_{dry}}{W_{sol} - W_{xyl}} \tag{3.1}$$

The amount of total porosity (P_{tot}) was calculated with the equation:

$$P_{tot} = 1 - \frac{\rho_{foam}}{\rho_{TiNi}} \tag{3.2}$$

For the determination of the open (P_{open}) and closed (P_{cls}) porosity Equation 3.3 and 3.4 were utilized.

$$P_{open} = \frac{\frac{W_{sol} - W_{dry}}{\rho_{xyl}}}{\frac{W_{sol} - W_{xyl}}{\rho_{xyl}}} = \frac{W_{sol} - W_{dry}}{W_{sol} - W_{xyl}} \tag{3.3}$$

$$P_{cls} = P_{tot} - P_{open} \tag{3.4}$$

3.4.3. Differential Scanning Calorimetry Analysis

The transformation temperatures of TiNi powders and foams were determined by Differential Scanning Calorimeter (DSC 8000, Perkin Elmer Inc., Massachusetts, USA) with 10 °C/min heating and cooling rates. Indium was used as the reference material. The analyses were performed under nitrogen atmosphere in a temperature range of -100°C to 150°C. Transformation temperatures were determined according to the procedure given in ASTM F2004-05 [84] from the second heating and cooling

cycles, which were performed after waiting 10 minutes after the end of first heating-cooling cycle. This procedure was applied to avoid the influence that will originate from possible residues on the samples.

TiNi powder was put into the aluminum sample holder and compressed for the analysis while TiNi foams were cut with a linear precision cutter (IsoMet 5000, Buehler LTD, Illinois, USA) using a diamond coated copper disc to produce DSC samples with a diameter of approximately 3 mm.

3.4.4. X-Ray Diffraction Analysis

The phases present at room temperature in as-received TiNi powder as well as processed porous TiNi alloys were determined via X-ray Diffraction (XRD) analyses using a conventional diffractometer (Rigaku D/Max 2200/PC, Rigaku Corporation, Tokyo, Japan) with Cu-Kα radiation operating at 40 kV and 40 mA. The measurements were performed at 2θ interval of 20°-90° with a scanning speed of 2°/min. X-ray analyses were also helpful in the determination of the reasoning behind the reactions that were observed during optimization of processing technique as mentioned before.

3.4.5. Scanning Electron Microscopy

The conformation of powder shape in addition to the microstructural analyses that were carried on both powders and processed TiNi foams was utilized by Jeol JSM 6400 scanning electron microscope (SEM) equipped with Noran System 6 X-ray microanalysis system. Carbon tape was used to handle powders during shape and size distribution analyses while the pore shape and size of the processed foams were analyzed directly from surfaces without any pretreatment.

On the other hand, both powders and porous TiNi alloys were embedded in epoxy resin (Epofix cold-setting embedding resin, Electron Microscopy Sciences LTD,

Hatfield, England) for the sample preparation to microstructural examination. After grinding and polishing steps, all TiNi samples were etched with 10% HF + 10% HNO_3 +80 % glycerin ($C_3H_8O_3$) solution for approximately 2 minutes.

Fracture surfaces that contain features beyond the resolution limit of Jeol JSM 6400 SEM and the heat treated TiNi foams were examined with a field emission SEM (Nova Nano 430, FEI Co. LTD., Eindhoven, Holland).

3.4.6. Transmission Electron Microscopy

Although, the results of both XRD and SEM examinations indicate that the processed TiNi foams are in fully austenitic state without the presence of any other intermetallic phases, transmission electron microscope (TEM) was also utilized since Ti_3Ni_4 phase, which would have been formed during processing of porous TiNi alloys, could only be detected by TEM.

The preparation of TEM samples were done with the following procedure:

1. Slices with a thickness of 200 μm were obtained from TiNi foams sliced with a linear precision cutter (IsoMet 5000, Buehler LTD, Illinois, USA) using a diamond coated copper disc,
2. Discs with a diameter of 3 mm. were obtained from those slices with TEM punch,
3. The discs obtained were ground to a thickness of 50 μm using silicon carbide (SiC) emery papers with grids through the range of 600 to 3000,
4. The further thinning was obtained by ion-milling with the following parameters:
   a. 5.5 kV / 5 mA / 15° / until collapse of the central part
   b. 5.5 kV / 5 mA / 10° / 4 h
   c. 2.0 kV / 5 mA / 10° / 1 h

The prepared specimens were examined by JEOL JEM2100F TEM operating with a 200 kV accelerating voltage.

3.4.7. Mechanical Characterization

Porous TiNi alloys were subjected to monotonic compressive testing in order to characterize their mechanical behavior under quasi-static conditions, especially towards biomedical applications. In addition, superelasticity and fatigue tests were applied to TiNi foams according to the feedback gained from monotonic compression tests. All of the mechanical test samples were 10 mm in diameter and height. The top and bottom surfaces, which will be in contact with the mechanical test system, were mechanically grinded to have parallel and planar surfaces using 1200 grid emery paper.

3.4.7.1. Monotonic Compression Tests

Monotonic compression tests were conducted with a 100 kN capacity screw driven mechanical tester (Instron 5582, Instron Co. LTD., Norwood, USA) by measuring the stress with respect to the strain at a constant crosshead speed of 0.1 mm/min. At least five specimens were tested for each porosity level since the porous structure has scattered the test results. Strain measurements were done with video extensometer (Instron 2663-821, Instron Co. LTD., Norwood, USA).

The accuracy of the test system was evaluated by testing pure aluminum bulk sample and it was found that the deviation was less than 2 MPa, which was found to be insignificant for the evaluation of the test results. Elastic moduli were determined from the linear portion of the stress-strain diagram by applying least squares curve fitting method whereas yield strength values were determined via 0.2%-offset method. In fact, yield strength of TiNi foams indicates the stress level of austenite-to-martensite transformation in addition to the slip deformation of austenite unlike to that generally observed in metallic materials. However, the term "yield strength"

was utilized for the sake of simplicity. On the other hand, ultimate strength values were determined as the maximum stress level that could be achieved before the collapse of the structure. All of the tests were carried at room temperature $(25° \pm 2°)$ unless otherwise stated.

3.4.7.2. Superelasticity Tests

The mechanical test system, which was used for monotonic compression tests, was also employed for the superelasticity tests. Superelasticity of porous TiNi alloys were characterized under compression with load controlled tests via the application of loading-unloading cycles to predefined stress levels with a stress rate of 10 MPa/min. All of the specimens were initially loaded to a stress level of $0.75 \ \sigma_{yield}$ to ensure that the specimen do not contain any defect that will result in a scatter in the obtained data. The tests were applied till full recovery of strain is achieved for a given stress level.

3.4.7.3. Fatigue Tests

According to the results of monotonic compression tests, load controlled compression-compression fatigue tests were applied to the porous TiNi alloys via a servohydraulic mechanical testing system (Dartec M9500, Dartec Co. LTD., Stourbridge, West Midlands, England) with a frequency of 5 Hz. The stress ratio $(\sigma_{min}/\sigma_{max})$ was kept constant at 0.1, and applied stress levels were determined relative to the yield strength of the TiNi foam with corresponding porosity level. S-N curves were obtained from the specimens tested within the maximum stress interval of $0.5 \ \sigma_y \leq \sigma_{max} \leq \sigma_y$, where σ_y corresponds to the yield strength of the porous alloy determined by the monotonic tests.
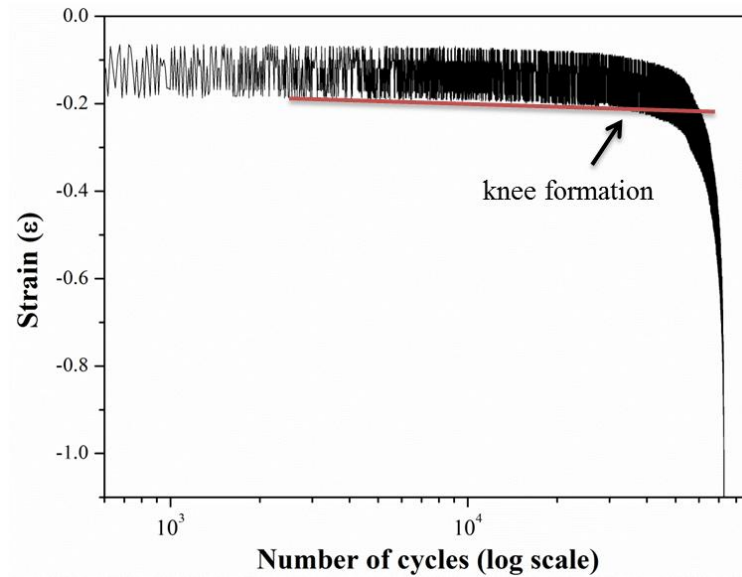
Figure 3.10 Representative strain versus number of cycles applied during fatigue test diagram indicating the knee formation point, which was taken as the criteria of failure (serrations are due to the limited capacity of data collection system).

In constructing the S-N curves, failure criterion was chosen as the knee formation in strain versus number of cycles diagrams (Figure 3.10) rather than the failure of the specimen [73] or the point where a certain percentage of the overall deformation has been observed [82], which are some failure criteria used in literature, since it was found to be more definitive and reproducible. Knee formation point was determined from strain versus number of cycles (in logarithmic scale) diagram as the deviation of maximum compressive strain values from linearity. The fatigue limit was considered to be achieved beyond 10^6 cycles and if failure has not occurred, tests were terminated at this value and those samples were considered to be fatigue immune.

CHAPTER 4

RESULTS AND DISCUSSION

4.1. Microstructural Characteristics of Processed TiNi Foams

Ti-50.8 at%Ni powder was processed by sintering at 1200 °C for 2 hours to obtain foams having porosities in the range of 39-64 vol%. Both total porosity and open porosity values of porous Ti-50.8 at%Ni alloys are given in Table 4.1.

Table 4.1 The change in total porosity with the amount of Mg added for porous Ti-50.8 at%Ni alloys sintered at 1200 °C for 2 hours.

Mg added (vol%)	Porosity (vol%)	Open Porosity (vol%)
40	39	38
50	49	48
60	58	57
70	64	63

Total porosity measured was found to be lower than amount of magnesium added (Table 4.1). Moreover, ~5 % shrinkage both in radial and longitudinal directions was observed for Ti-50.8 at%Ni foams after sintering. Total porosity values given in Table 4.1 indicate the amount of macropores, which were created by the evaporation of Mg during sintering, in addition to the micropores, which were retained between TiNi powders due to insufficient sintering. Although the total porosity, which consists of macropores in addition to the micropores, is expected to be more than the magnesium added to form the macropores by an amount equal to the micropores, the

opposite is observed. The lower total porosity attained was attributed to the decrease in microporosity in the walls during sintering after the evaporation of magnesium. Elimination of the micropores in the walls cause the walls to shrink in length as well as in the width resulting in the shrinkage of the macropores they surround. This assertion was also corroborated by SEM micrographs indicating the decrease in microporosity after sintering (Figure 4.1(a)).

(a)   **(b)**
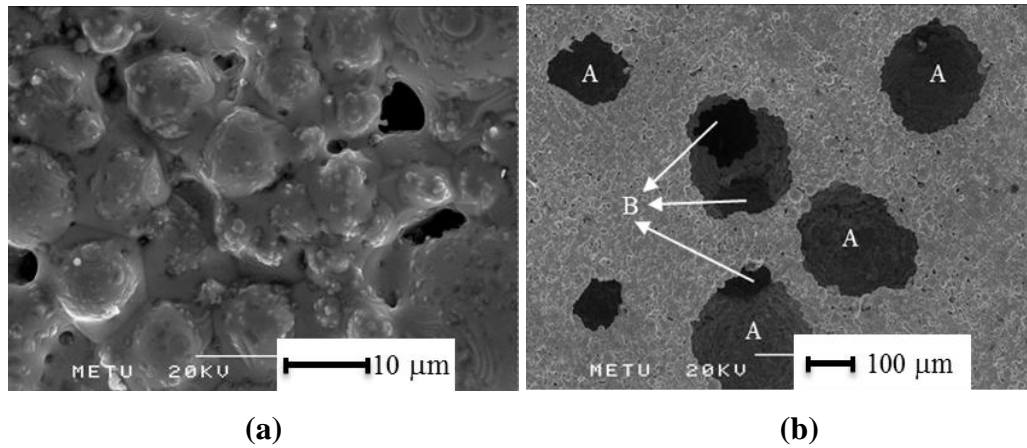
Figure 4.1 SEM micrographs indicating (a) microporosity, (b) general view for porous Ti-50.8 at%Ni alloys sintered at 1200 °C for 2 hours.

Furthermore, as it is obvious from Table 4.1, it was determined that most of the measured porosity is open porosity, which enables transportation between pores. The open porosity was defined as the amount of interconnected pores. Interconnection was established by both the contact regions between the macropores as given in Figure 4.1(b) and the micropores (Figure 4.1(a)) that connect macropores. The macropores located at the surface were labeled with "A" and the interior macropores were labeled with "B" to indicate the interconnections. The equiaxed morphology of these macropores (which will be addresses by the term "pore" from hereafter) resulting from the spherical morphology of the spacer magnesium is also apparent in Figure 4.1 (b). SEM analysis also has revealed that relatively homogeneous distribution have been achieved by sintering with Mg space

holder technique, as shown by the polished cross sectional SEM micrographs given in Figure 4.2.
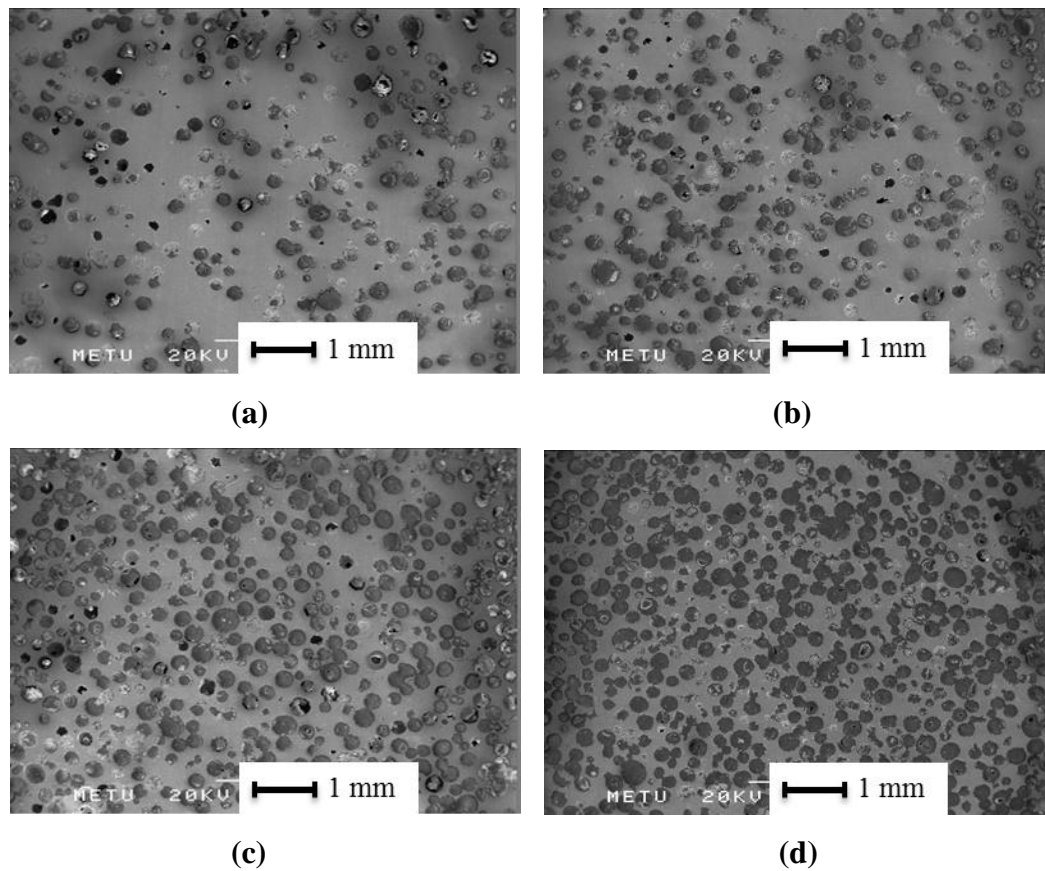
Figure 4.2 The distribution of pores for TiNi foam with (a) 39, (b) 49, (c) 58, (d) 64 vol% porosity.

All of the processed TiNi foams were found to be in fully austenitic state after sintering, while oxidation and/or formation of secondary intermetallics have been found to be prevented as revealed by the results of the XRD analysis (Figure 4.3). In addition to B2 austenite peaks, quite small MgO peaks were also observed due to the residual MgO particles, which were formed as the result of oxidation of Mg during sintering. The trace amount of residual MgO particles could have been eliminated by dilute HCl treatment after sintering without impairing TiNi; however, as they have no effect on mechanical properties of the porous alloys it has not been attempted.
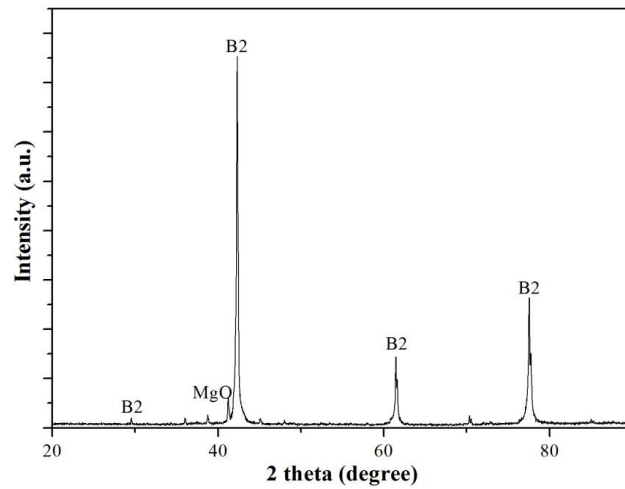
Figure 4.3 Representative XRD analysis result of sintered Ti-50.8 at%Ni foam.

The presence of MgO residuals was also revealed by SEM micrographs given in Figure 4.4. Austenitic microstructure of processed TiNi foams was also confirmed by SEM analysis. The scratch-like patterns that appear in Figure 4.4 (b) are present due to the deformation induced during the preparation of the sample. No indication of secondary intermetallic formation was found neither in secondary electron nor in back scattered electron imaging modes.

(a)   **(b)**
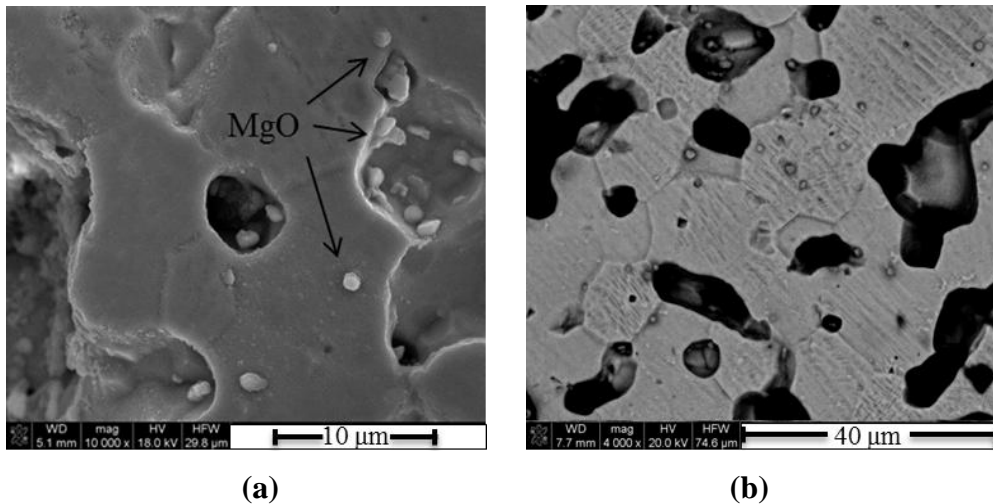
Figure 4.4 SEM micrographs of porous TiNi alloy showing the fully austenitic structure: (a) secondary electron, (b) back scattered electron imaging modes.

DSC analysis results (Figure 4.5) indicate that the transformation temperatures of the processed foams are higher than that of TiNi powder used as given in Table 4.2. The increase in transformation temperatures can be attributed to the precipitation of Ti_3Ni_4 phase, which decreases the Ni-concentration of the matrix. However, a clear evidence of two-step transformation, $B2 \rightarrow R \rightarrow B19'$, is not present for TiNi foams.

Table 4.2 DSC analysis results for TiNi powder and foam.

TiNi	Phase Transformation Temperatures (K (°C))						Latent Heat of Transformation (J/g)	
	M_f	M_p	M_s	A_s	A_p	A_f	$-\Delta H_{forw}$	ΔH_{rev}
powder	245	265	279	243	272	288	0.98	9.18
	(-28)	(-8)	(6)	(-30)	(-1)	(15)		
foam	255	291	320	268	298	328	1.76	1.27
	(-18)	(18)	(47)	(-5)	(25)	(55)		
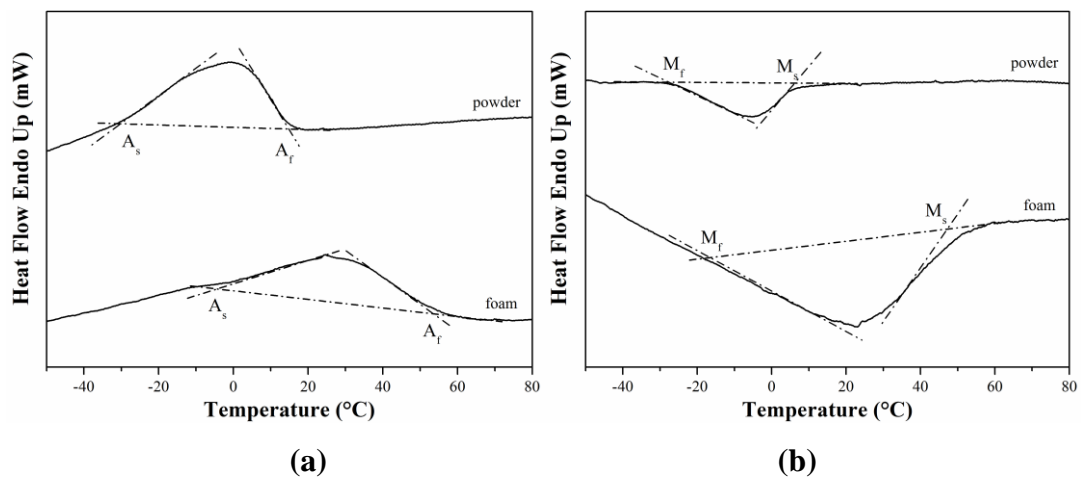
Figure 4.5 DSC analysis results for (a) as-receved TiNi powder, (b) processed TiNi foam.

Another reason of the increase in the transformation temperatures may be the removal of oxide layer, which was present on the surface of as-received TiNi powders, during sintering due to the reducing effect of Mg vapor. Because, that oxide layer, which was found to be mainly consist of TiO_2 [85, 86], decreases the ratio of Ti:Ni, and reduction of the oxide layer indirectly increases the Ti ratio leading to the increase of the transformation temperatures.

4.2. TEM Characterization of Processed TiNi Foams

Although, the results of XRD analysis (Figure 4.3) and SEM examinations (Figure 4.4) indicate that the processed Ti-50.8 at%Ni foams are in fully austenitic state, foams were also examined by TEM since precipitates such as Ti_3Ni_4 can be formed even at cooling rates as high as the ones applied in the present case and the presence of Ti_3Ni_4 precipitates has considerable effects on the mechanical behavior of TiNi foams. The presence of these precipitates is hard to detect with SEM due to their sizes in nanometer range. Moreover, XRD analysis has not been sufficient to detect them since the concentration would be very low due to unaged condition of the foams. Accordingly, TEM samples were prepared from Ti-50.8 at%Ni foams, which have porosity content in the range of 39-58 vol%, by ion-milling technique to investigate the presence of precipitates.

Ti_3Ni_4 phase, which has a crystal structure similar to that of TiNi, is characterized by extra spots aligning on <123> direction of TiNi diffraction pattern as given in Figure 4.6 (a) and coherently precipitates with lenticular shape.
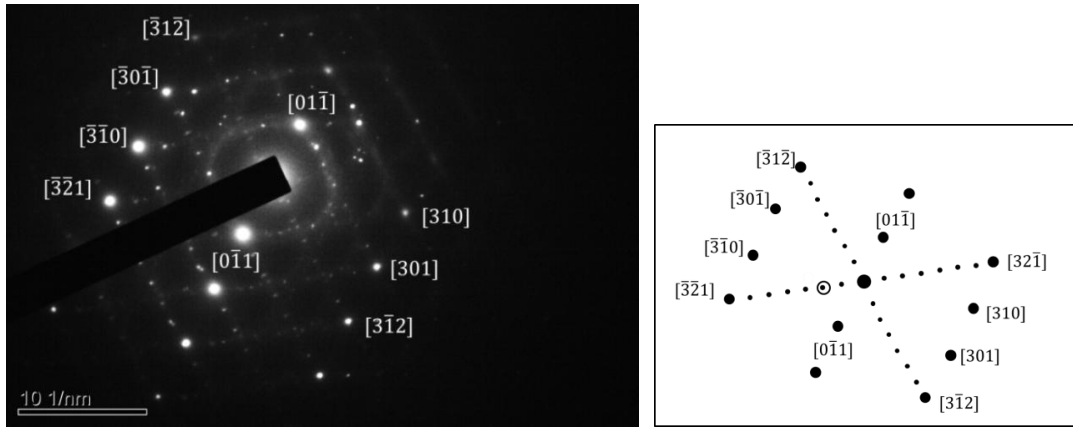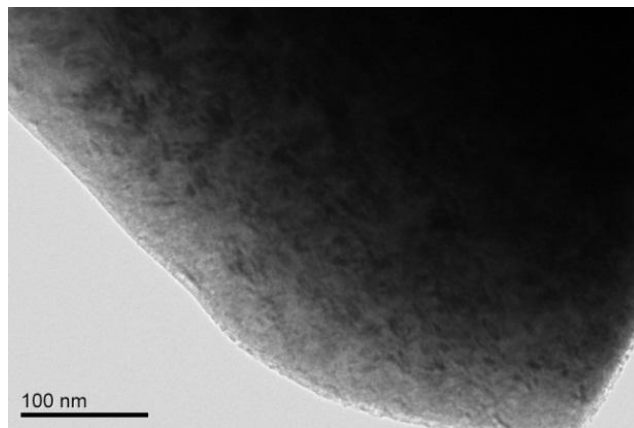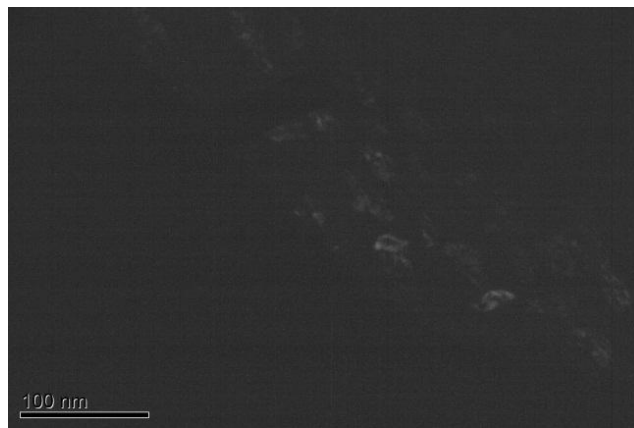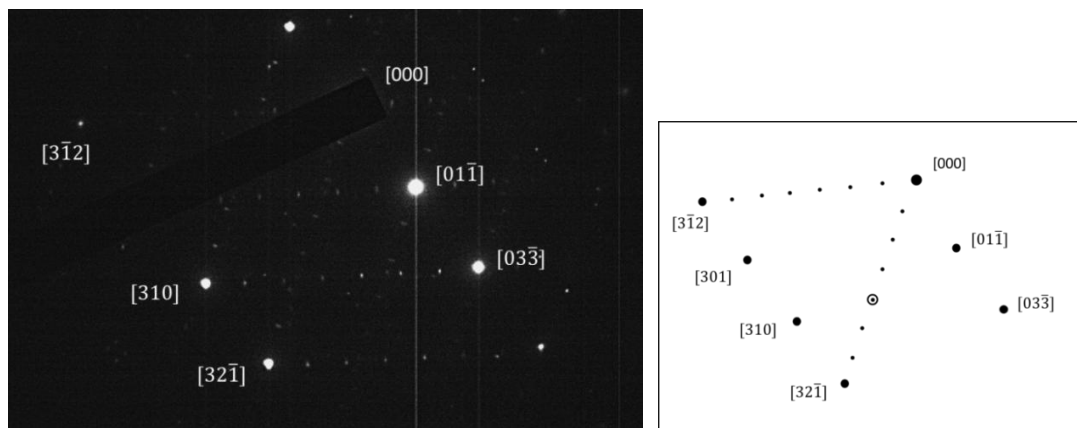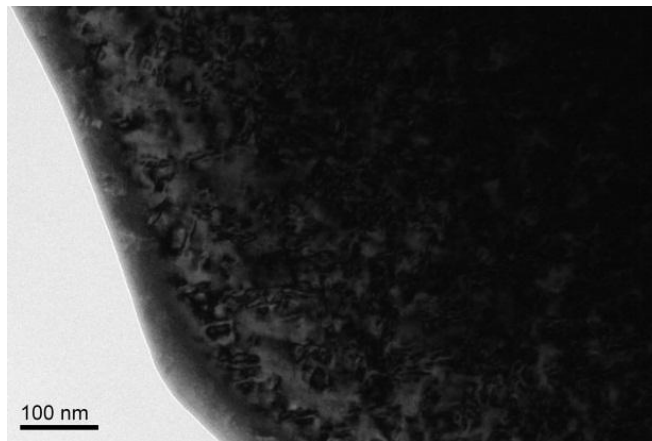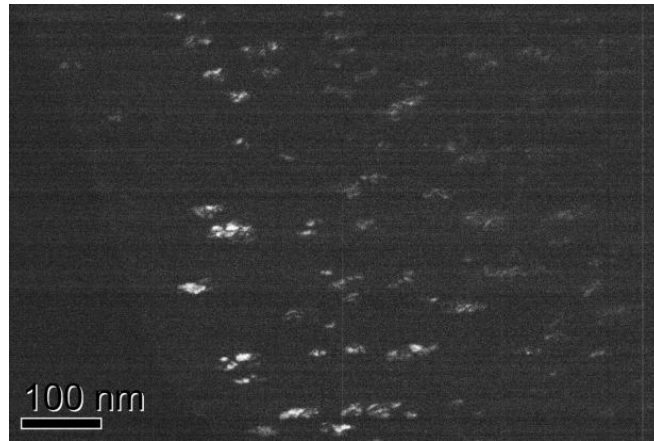
Figure 4.6 (a) Diffraction pattern taken from $[\bar{1}33]$ zone of sample prepared from TiNi foam, (b) bright field image, (c) on-axis dark field image taken from the diffraction spot labeled by drawn circle in (a).

77

The lens-like shaped dark regions with 10-20 nm length, which is given in Figure 4.6 (b), are believed to be due to the strain fields created by Ti_3Ni_4 precipitates. The diffraction pattern taken from this region, $[\bar{1}33]$ zone, indicated the presence of extra spots along $<\bar{3}1\bar{2}>$ direction. Although not being clear enough, the on-axis dark field taken from the precipitate diffraction spot labeled by drawn circle in Figure 4.6 (a) has shown the presence of Ti_3Ni_4 precipitates (Figure 4.6 (c)). In fact, Ti_3Ni_4 precipitates are also present in the darker regions but the thickness of the sample prevents their appearence.
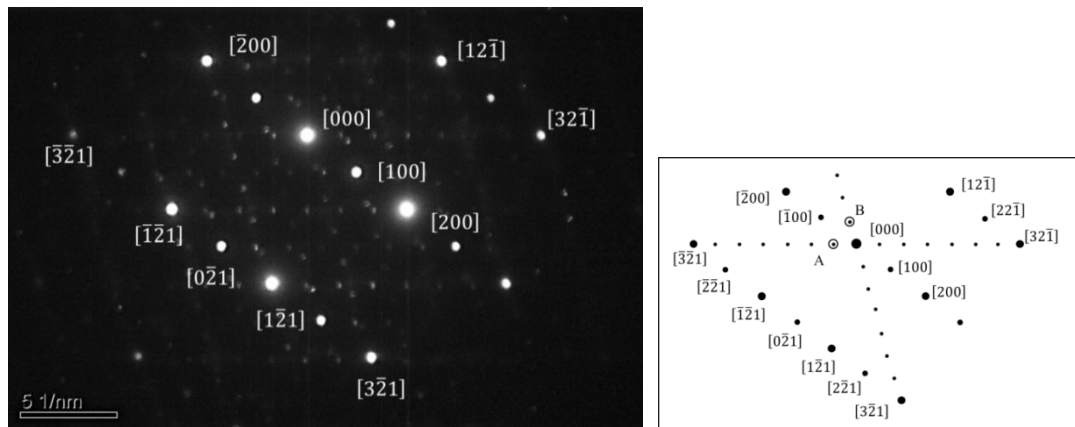

(a)

(b)

Figure 4.7 (a) Diffraction pattern taken from $[\bar{1}33]$ zone of sample prepared from TiNi foam, (b) bright field image.
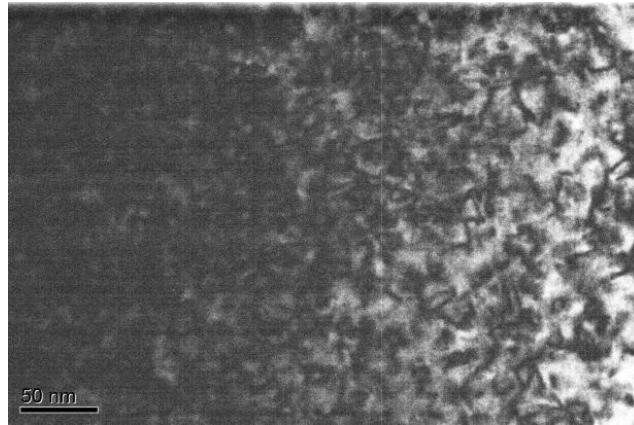
(c)

Figure 4.7 (Continued) (c) on-axis dark field image taken from the diffraction spot labeled by drawn circle in (a).

Another field of investigation with a diffraction pattern taken from $[\bar{1}33]$ zone was given in Figure 4.7. The on-axis dark field image (Figure 4.7 (c)) taken from the labeled spot in Figure 4.7 (a) has revealed the shape and size of precipitates more clearly.
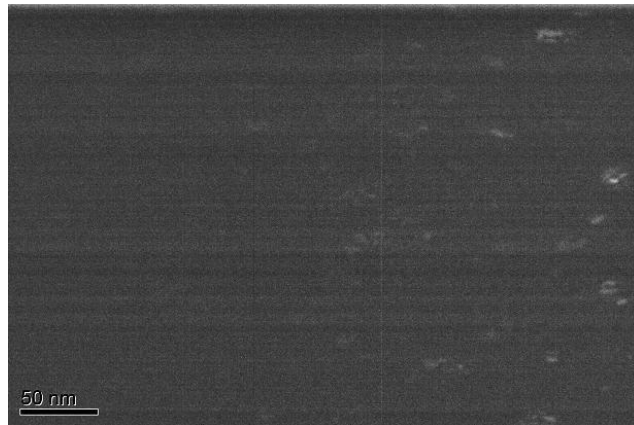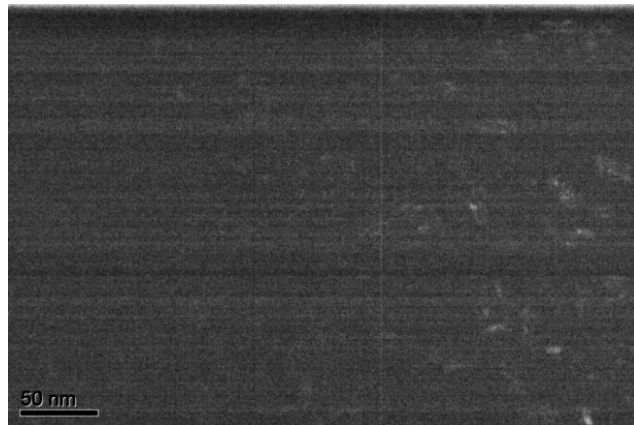

(a)

Figure 4.8 (a) Diffraction pattern taken from [012] zone of sample prepared from TiNi foam.

(b)

(c)

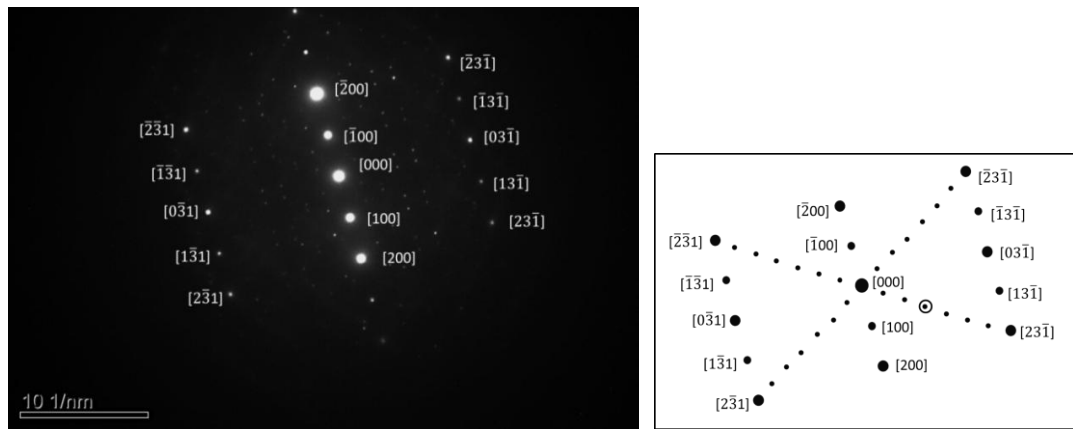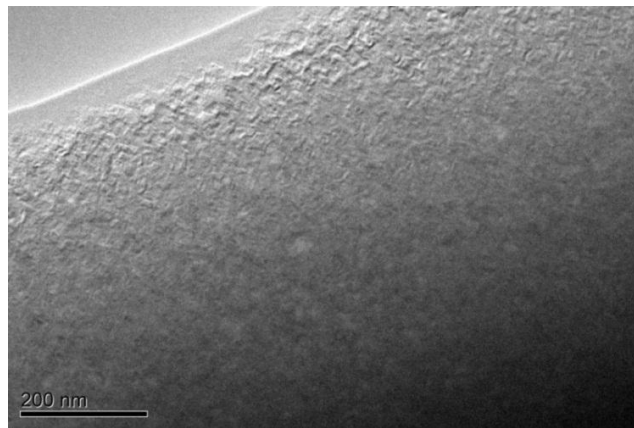**(d)**

Figure 4.8 (Continued) (b) bright field image, (c, d) on-axis dark field micrographs taken from the diffraction spots labeled as "A" and "B" respectively in (a).

Presence of Ti$_3$Ni$_4$ precipitates was also revealed at other zones such as [012], [013], [$\bar{1}$15], [$\bar{1}$12] as given in Figures 4.8 to 4.11, respectively.
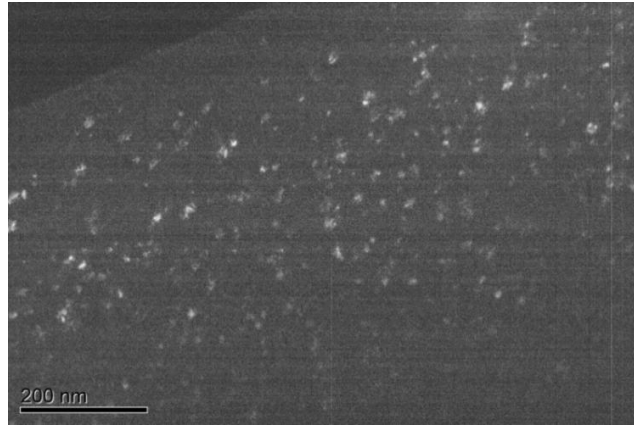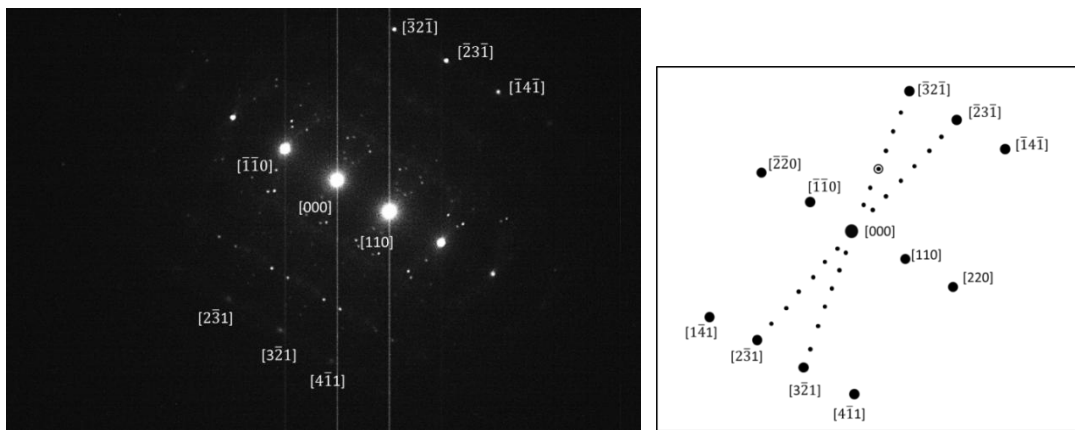

(a)

(b)

Figure 4.9 (a) Diffraction pattern taken from [013] zone of sample prepared from TiNi foam, (b) bright field image.
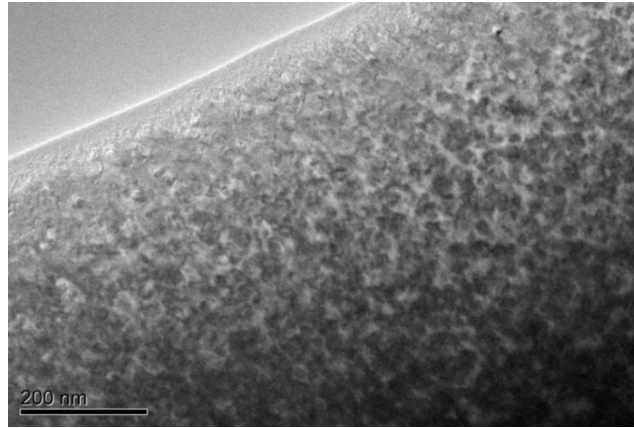
(c)

Figure 4.9 (Continued) (c) on-axis dark field micrographs taken from the from the diffraction spot labeled by drawn circle in (a).

(a)

Figure 4.10 (a) Diffraction pattern taken from $[\bar{1}15]$ zone of sample prepared from TiNi foam.

(b)

(c)

(d)

Figure 4.10 (Continued) (b) bright field image, (c) on-axis dark field micrograph taken from the diffraction spot labeled by drawn circle in (a), (d) high resolution micrograph taken from same region indicating presence of Ti_3Ni_4 precipitates.
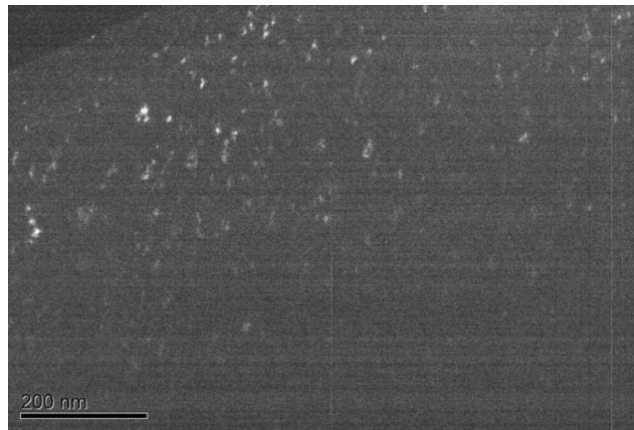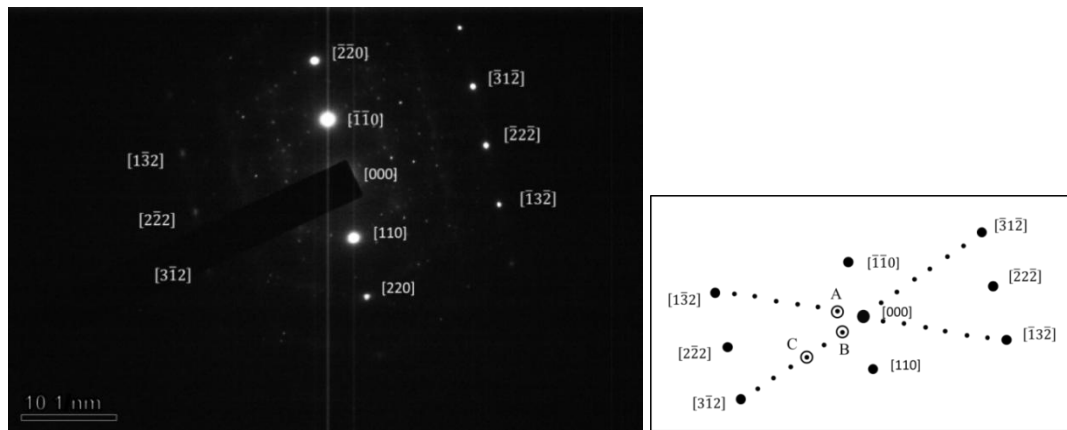
(a)
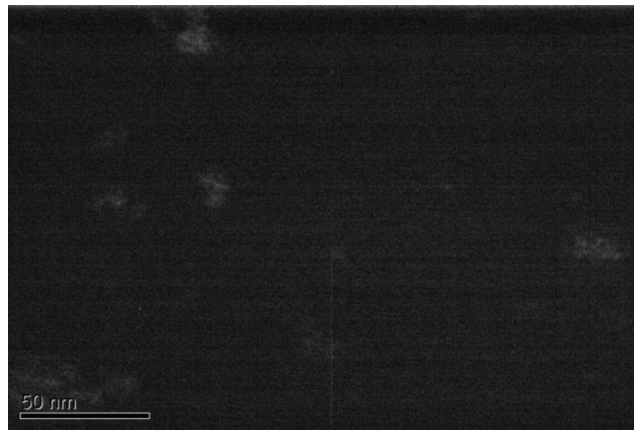
(b)
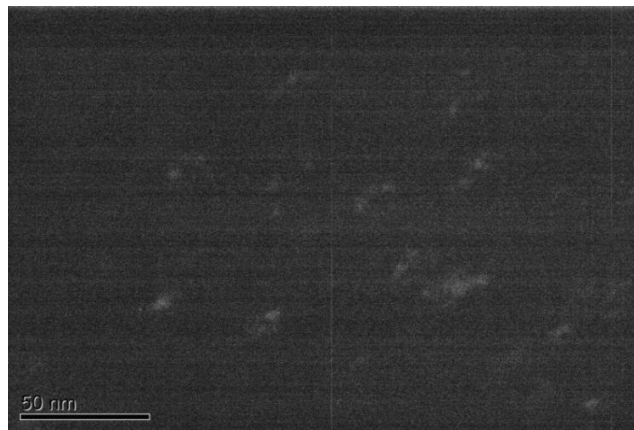
(c)

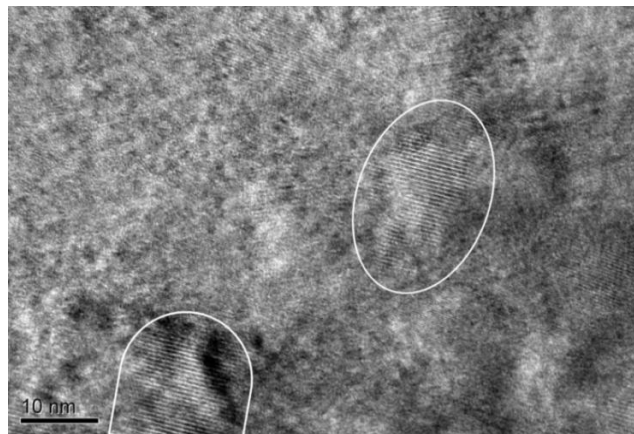**Figure 4.11** (a) Diffraction pattern taken from $[\bar{1}12]$ zone of sample prepared from TiNi foam, (b, c) on-axis dark field micrographs taken from the diffraction spots labeled as "A" and "B"respectively in (a).
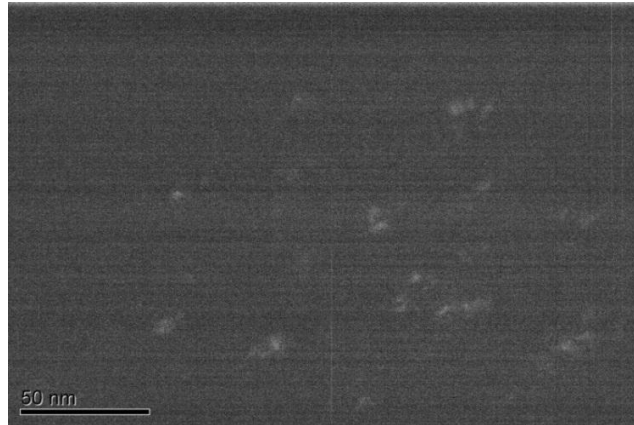
(d)

Figure 4.11 (Continued) (d) on-axis dark field micrograph taken from the diffraction spot labeled as "C" in (a).

It was observed from dark field micrographs that Ti_3Ni_4 precipitates have relatively homogeneous distribution. On the other hand, it was difficult to measure the size of the precipitates from dark field micrographs. Therefore high resolution micrographs, taken at different zones were used to measure the size of Ti_3Ni_4 precipitates. However, as it is obvious from Figure 4.12, high resolution micrographs were not also clear enough to reveal the size and shape of the precipitates due to the presence of surface defects that were inevitable during TEM specimen preparation from TiNi foams.
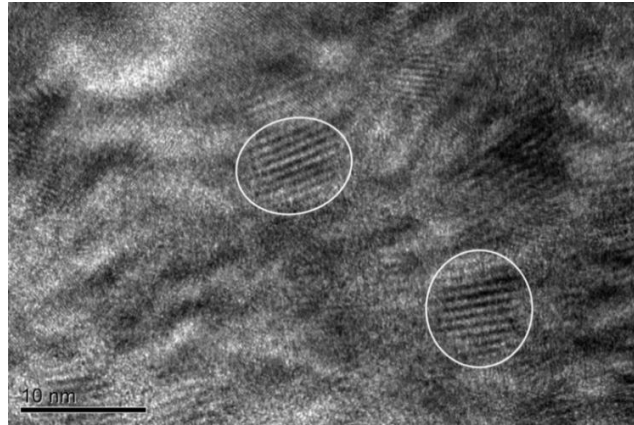
(a)
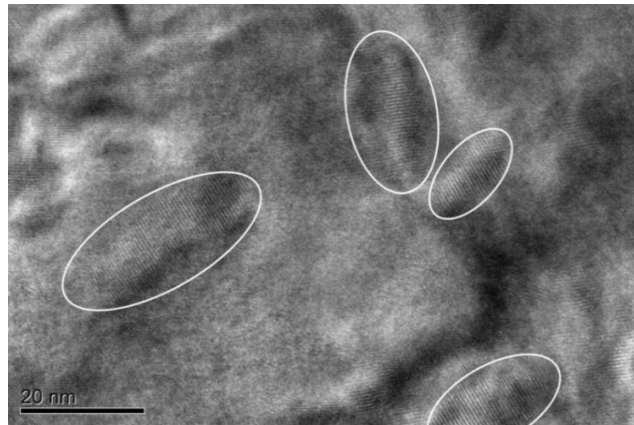
(b)

Figure 4.12 (a, b) High resolution images taken at [012] and [133] zones, respectively.

4.3. Mechanical Characterization of Processed TiNi Foams

The results of monotonic compression tests are summarized in Table 4.3 and Figure 4.13 for Ti-50.8 at%Ni foams, which were processed via sintering at 1200 °C for 2 hours, with varying porosity contents. It was observed that relatively uniform distribution of the pores with spherical shape resulted in high strength values enabling the use of specimens with higher porosity

Table 4.3 Mechanical properties of Ti-50.8 at%Ni foams tested in compression, where E is Young's modulus, σ_y is yield strength, σ_{max} is compressive strength.

Mg added (vol%)	Porosity (vol%)	E (GPa)	σ_y (MPa)	σ_{max} (MPa)	$\dfrac{\sigma_{max}}{\sigma_y}$
40	39	12.49 ± 0.12	154.85 ± 10.70	394.76 ± 17.85	2.55
50	49	8.71 ± 0.24	147.93 ± 12.10	273.45 ± 9.25	1.85
60	58	5.87 ± 0.31	91.50 ± 8.50	174.75 ± 10.75	1.91
70	64	2.93 ±0.03	44.12 ± 7.65	93.27 ± 5.30	2.11

The wide range of strength and elastic modulus values that may be achieved by changing the amount of porosity makes it possible to tailor the properties of the TiNi foams so that they can fulfill various requirements. The mentioned flexibility is important for biomedical applications, which is the main application field of porous TiNi alloys, since there is a huge difference between the elastic moduli of the cortical bone (4.4-28.8 GPa) and the cancellous bone (0.01-3.0 GPa) [87].
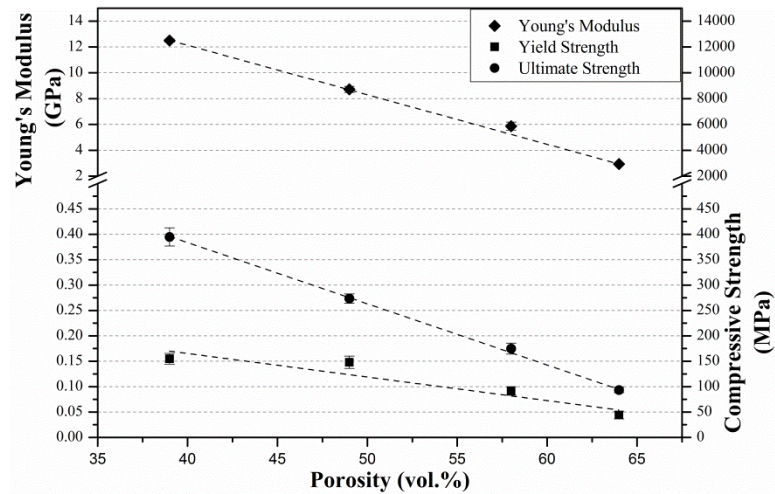
Figure 4.13 The change in mechanical properties with varying amount of porosity.
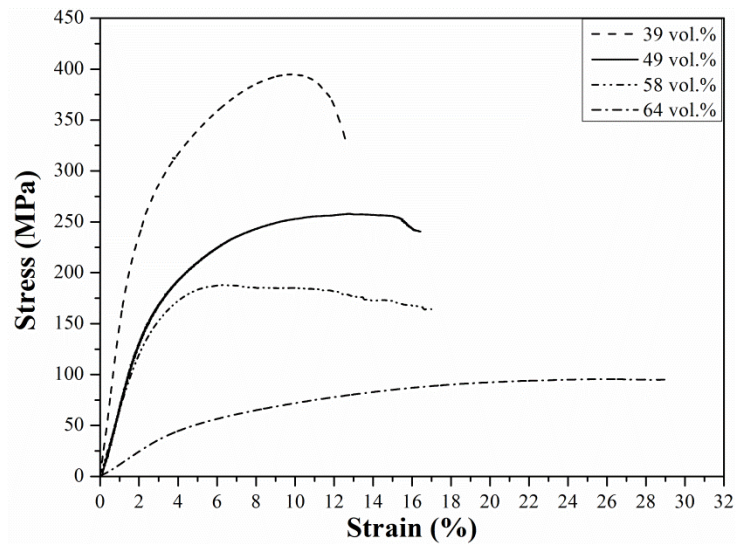
Figure 4.14 Compressive stress-strain curves for TiNi foams with varying porosity contents.

On the other hand, compression behavior was observed to differ for TiNi foams with different porosities as given in Figure 4.14. While TiNi foams with lower porosity was observed to fail shortly after attaining the ultimate compressive strength, strength of high porosity foams was reduced so gradually that it almost displays a plateau with an enhanced ductility. The reason of the change in failure behavior is believed to be due to the change in the mechanical response of the foam with porosity (Figure 4.15).

When the porosity level is low, deformation occurs homogeneously as if TiNi foam is a composite material, which consist of bulk TiNi as matrix and pores as the second phase. Accordingly, failure occurs as a result of combination of cracks that were initiated from the edge of pores. On the other hand, struts become effective during the deformation of TiNi foam with higher porosity content (64 vol%) since the aspect ratio of struts increases with increasing porosity content. As schematically shown in Figure 4.15 (b), the size and orientation of struts, which were shown as the gray regions, determine the deformation mode that is active during deformation of different parts of the compression sample. As the deformation proceeds, struts

and/or strut groups that exceed the ultimate strength due to their favorable orientation and/or size locally collapses, and after the failure of each such struts a small plateau region was reached with the transient stiffening of these regions with lower porosity up to the failure of another strut or strut group. Maximum compressive strength has achieved shortly after the yield point for TiNi foams having 64 vol% porosity content since increased porosity has led to more thinner and longer strut formation. The change in the geometrical distribution of the struts led to more homogeneous deformation behavior, which results in total collapse of the structure.

(a)

(b)
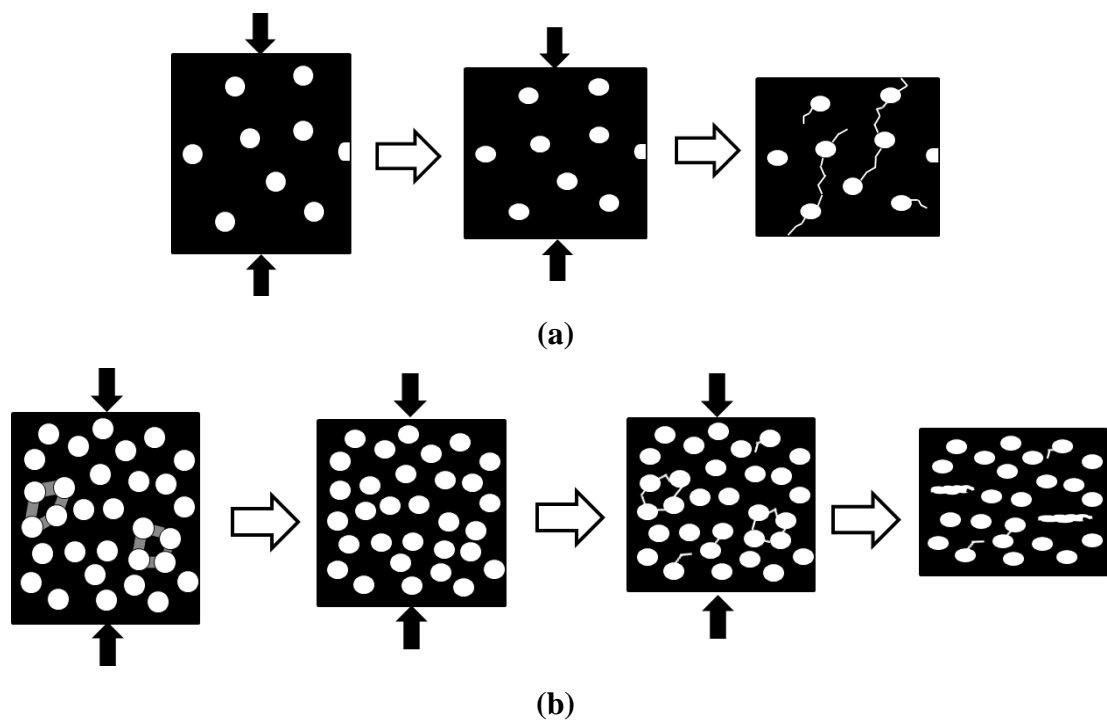
Figure 4.15 Schematical representation of compressive deformation mechanism of TiNi foams with (a) 39 vol% porosity, (b) 64 vol% porosity.

4.3.1. Characterization of Superelastic Behavior of TiNi Foams

As it was mentioned before, the superelasticity is one of the key properties that gave preference to the employment of TiNi for many applications. Accordingly, Ti-50.8

at%Ni foams were cyclically loaded up to a predefined stress level and unloaded to determine the amount of strain recovery and cycling was continued till full recovery of strain for that stress level was achieved. Following the attainment of full recovery, the level of stress was raised and the same procedure was repeated as given in Figure 4.16 (a).

The superelasticity tests conducted on TiNi foams with 58 vol% porosity has revealed that complete recovery of the applied strain could be achieved in single cycle when the applied stress is not much above the yield point, Figure 4.16. However, after deformation to higher stress levels, varying amounts of residual strain was observed upon unloading.

The first cycle of deformation to a maximum stress of 120 MPa was analyzed in detail in Figure 4.16 (b) to describe superelastic deformation characteristics of TiNi foams, where mainly four regions with different deformation characteristics were detected. Stage I, which corresponds to the elastic deformation of austenite, is followed by deviation from linearity in Stage II due to the martensitic transformation induced deformation as well as some plastic deformation of austenite. One of the reasons for this dual effect, i.e., deformation by two different mechanisms, can be attributed to the varying orientation of the sintering necks with respect to the applied loading direction. Since all of the struts will not be parallel to the loading direction, compression will not be the only deformation mode. Instead, different deformation modes including compression, bending and even tension will be active in different regions of the test sample depending on the cross-sectional area, height and relative orientation of sintering necks with respect to each other and loading direction.
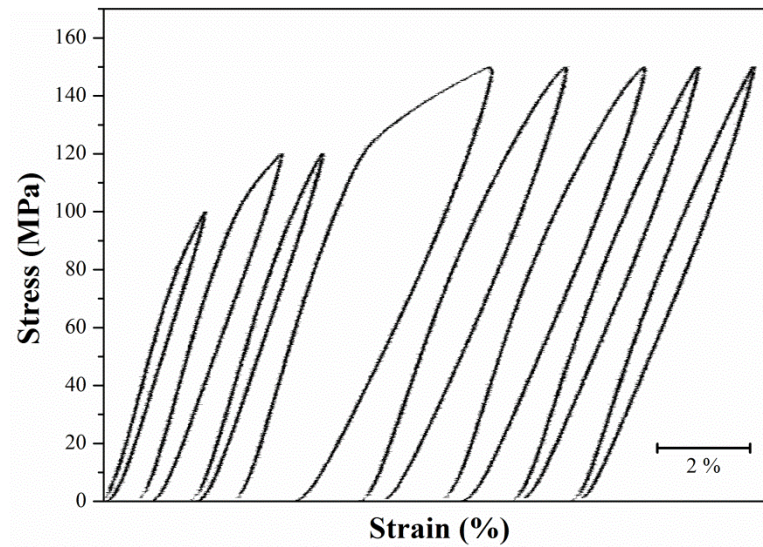
(a)
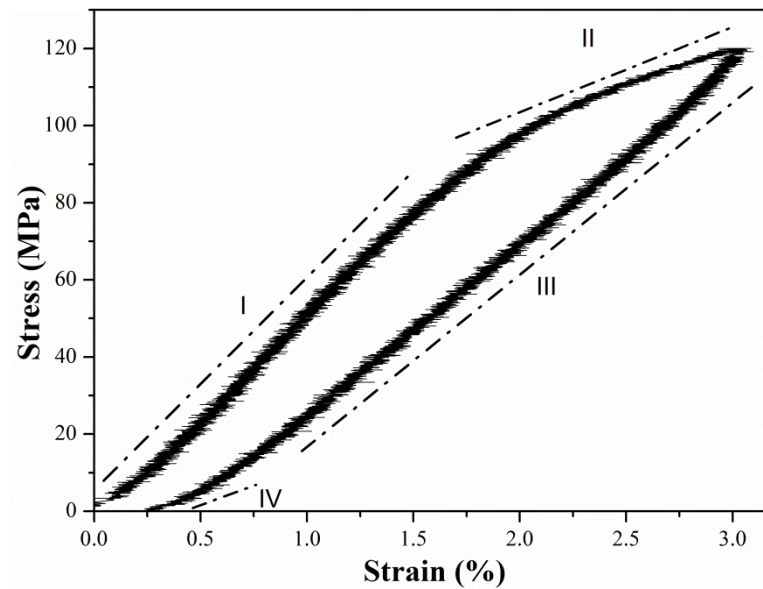
(b)

Figure 4.16 (a) The consecutive stress-strain curves of Ti-50.8 at%Ni foams with 58

vol% porosity indicating the role of training at120 and 150 MPa sequentially,

(b) first cycle of 120 MPa training that indicates the regions of different deformation

characteristics.

Furthermore, size and aspect ratio of the sintering necks should be considered, since

two sintering necks with same orientation but different heights will be subjected to

different amounts of strain even if the overall deformation of the foam is constant. Therefore, all of the foam could not be homogeneously transformed to martensite during the second stage, and the stress-strain curve follows an increasing trend instead of displaying a plateau region. On the other hand, higher stress levels required for the progress of martensitic transformation will result in the plastic deformation of the previously formed martensitic regions with increasing stress. As a consequence of martensite deformation and dislocations formed at the austenite/martensite interfaces, which lock the martensite plates against further sliding, will prevent the reverse transformation upon unloading. Presence of residual martensite after the deformation of TiNi foam with 58 vol% porosity was also confirmed with XRD analysis results as given in Figure 4.17.

Upon the removal of load (Stage III), elastic deformation in both austenite and martensite recovers first. As it is obvious from Figure 4.16 (b), the slope of the initial portion of the unloading curve is lower than that of the first region, although both are correlated to elastic deformation. The difference in the slope of stress-strain curve of the third region compared to that of the first region results from the recovery of the elastic deformation of martensite together with austenite instead of austenite only (Stage I), where the elastic modulus of martensite is lower than that of austenite [88-90]. This stage was followed by reverse transformation of stress-induced martensite that has not been plastically deformed (Stage IV). As the result of the slip of austenite and deformation of martensite, full recovery of strain could not be achieved after the first cycle, which can be actually achieved by a procedure called "training" [91, 92]. The training process is applied via deforming a specimen to the same level of stress for several times. At each step, irreversibly deformed regions of the specimen became inoperative so that remaining portions of the specimen exhibit only martensitic transformation upon loading at the last cycle without being obscured by the effect of former plastic deformation.
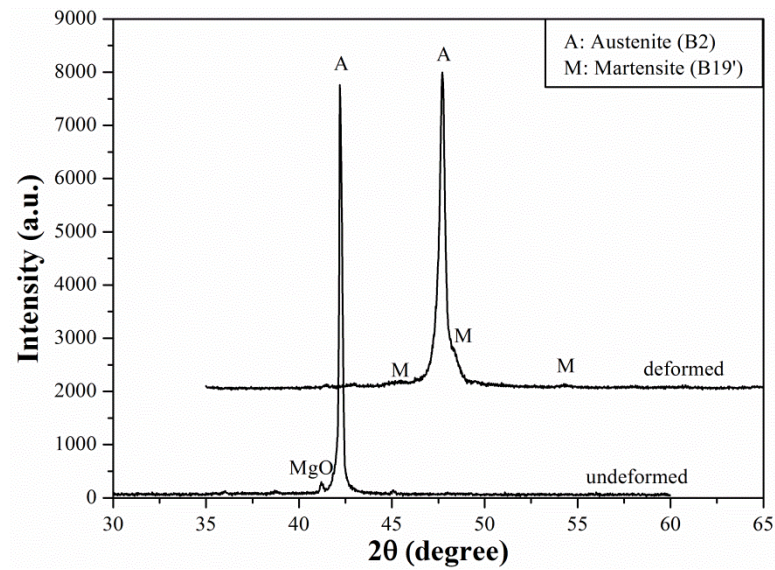
Figure 4.17 XRD analysis results for TiNi foams with 58 vol% porosity taken before and after the deformation.

The amount of maximum strain that can be achieved and hence the recovered strain, could be increased by increasing the applied stress or by decreasing the porosity content. However, if the training is conducted by stress increments, the effect of previous training cycles, applied at lower stress levels, on the response of TiNi foams to the applied deformation should also be considered. As presented in Figure 4.16 (a), stress-strain curve of TiNi foam starts to deviate from linearity at a higher stress level during its deformation up to 150 MPa after being trained at 120 MPa for two cycles. This implies the fact that after training at a certain stress level deformation becomes totally elastic and a higher stress level is required to trigger further martensitic transformation, only a part of which is recoverable because of dislocation deformation encountered.

Therefore, real contribution of each stress level on the maximum achievable strain should be analyzed seperately. To elucidate the superelasticity mechanism of TiNi foams, foams with 58 vol% porosity were also directly tested at 150 MPa to compare with those trained by stress increments as given in Figure 4.16 (a).
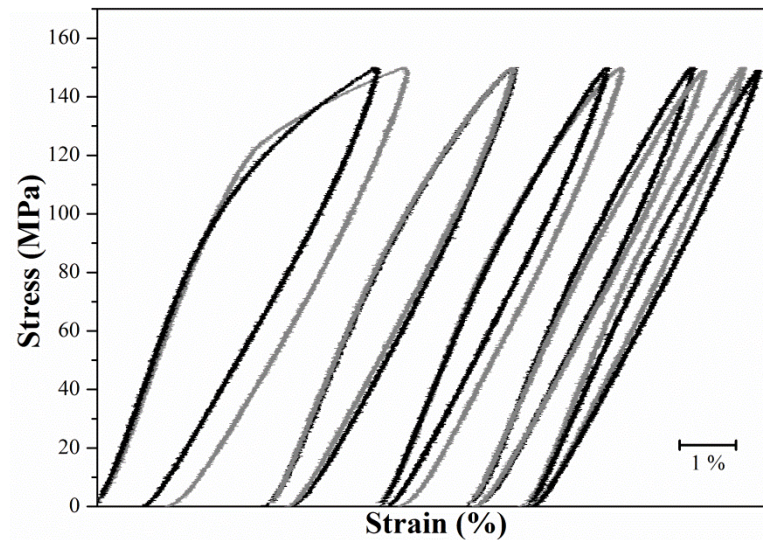
(a)
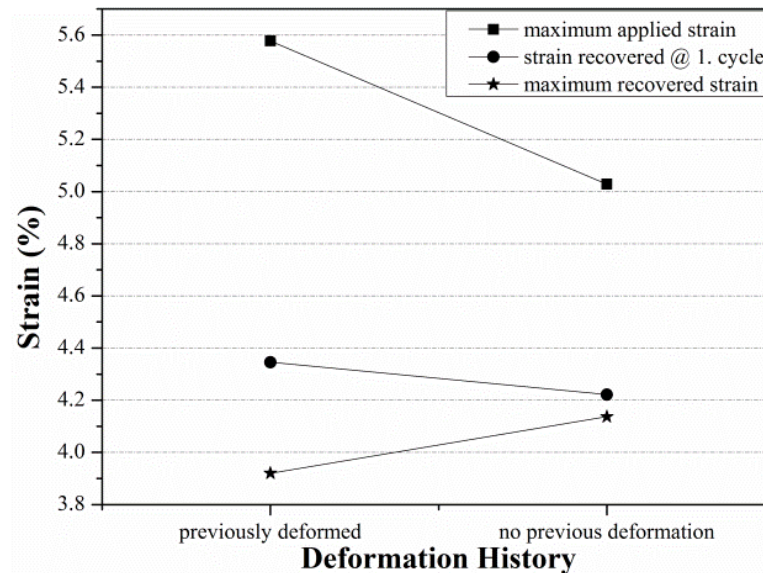
(b)

Figure 4.18 (a) Comparison of the response of TiNi foam with 58 vol% porosity with(grey lines) and without(dark lines) previous deformation to the applied stress, (b) the dependence of applied and recovered strain to the loading history.

Comparison of the two results obtained from superelasticity tests with and without previous deformation (Figure 4.18) has revealed that deviation of stress-strain curve from linearity (critical stress for the austenite to martensite transformation) at first cycle starts at a lower stress level for TiNi foam which has been directly tested up to

150 MPa. Moreover, for the directly tested foam, both the maximum reached and recovered strain values were found to be considerably less during the first cycle of deformation. These differences are not unexpected, because during loading of TiNi foam that was previously trained at 120 MPa, the struts which were deformed irreversibly due to either their orientation or size, do not contribute to further deformation and accordingly, deviation from linearty initiates at 120 MPa when the foam is deformed up to 150 MPa. Furthermore, the maximum strain and recovered strain achieved at the end of the first cycle was found to be higher due to the accumulation of internal stress, which enhances austenite-martensite transformation, during previous training cycles at 120 MPa since cyclic movement of austenite-martensite interfaces during loading-unloading results in creation of dislocations, which arranged so that to support the martensitic and reverse transformation. On the other hand, both the maximum achieved and recovered strain values was found to be higher for untrained (directly tested) foam during the last two cycles. These differences were attributed to the inhibition of the contribution of struts that were plastically deformed or irreversibly transformed into martensite during previous training cycles at 120 MPa, since the portion of the foam that can contribute to the transformation of austenite to martensite has decreased.

Another set of mechanical tests were also conducted on TiNi foams with a porosity range of 39-64 vol% to determine the effect of porosity on the superelastic behavior of the processed TiNi foams. For this purpose, TiNi foams were directly subjected to a stress level of 0.85 σ_{max}, which is the ultimate compressive strength of each foam with the corresponding porosity level. The reason for the selection of ultimate compressive strength instead of yield strength (σ_y) as the reference level is that the stress referred to as yield strength is in fact the critical stress for martensitic transformation rather than being a mechanical parameter. Furthermore, yield strength is highly sensitive to temperature, composition and microstructure, while ultimate compressive strength is a proper mechanical parameter.
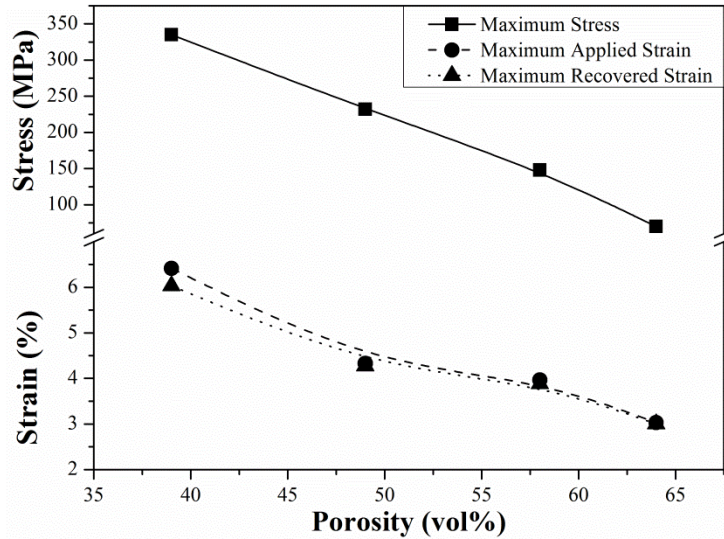
Figure 4.19 Results of superelasticity tests at a stress of 0.85 σ_{max} applied.

The results of the superelasticity tests obtained at the end of five cycles of training for different porosity contents were summarized in Figure 4.19. Maximum stress was 0.85 σ_{max} of the corresponding porosity while maximum strain and maximum recovered strain were measured at the end of fifth cycle. Maximum strain achieved and recovered strain values increase while the fraction of strain recovered at the end of fifth cycle decreases with decreasing porosity content. This trend can be related with the difference in the proportion between the ultimate and yield stresses (σ_{max} / σ_y) for the varying porosity levels. As it was given in Table 4.3, that ratio was similar for TiNi foams having 49 and 58 vol% porosity, whereas TiNi foams with 39 vol% porosity have remarkably higher σ_{max} / σ_y. This implies that maximum stress applied to TiNi foam with 39 vol% porosity during superelasticity tests was far more higher than the yield stress of leading to more plastic deformation to occur in this foam. On the other hand, TiNi foams with 64 vol% porosity were tested at maximum stress of 0.75 σ_{max} instead of 0.85 σ_{max} since these foams were failed during cycling at 0.85 σ_{max}. The collapse of these foams after three or four cycles at maximum stress of 0.85 σ_{max} was attributed to the combined effect of the struts with high aspect ratio and higher σ_{max} / σ_y ratio with respect to that of TiNi foams with 49 and 58 vol% porosity.

4.3.2. Fatigue Behaviour of TiNi foams

Another factor that should be taken into account during the optimization of the foam properties for structural applications is the fatigue life. Fatigue behavior was examined via load controlled compression-compression fatigue tests that were within the interval of $0.5\,\sigma_y \leq \sigma_{max} \leq \sigma_y$. The endurance limit of the tested foams was taken as the stress level at which the specimens sustain their integrity without showing any sign of failure beyond 10^6 cycles. The specimens that did not fail after this period were examined by SEM to determine whether a damage or structural change has occurred in their microstructure. As can be seen in Figure 4.20, neither a change in the spherical morphology of the pores nor an indication of a crack initiation was observed after the fatigue test of these foams.

(a)   **(b)**
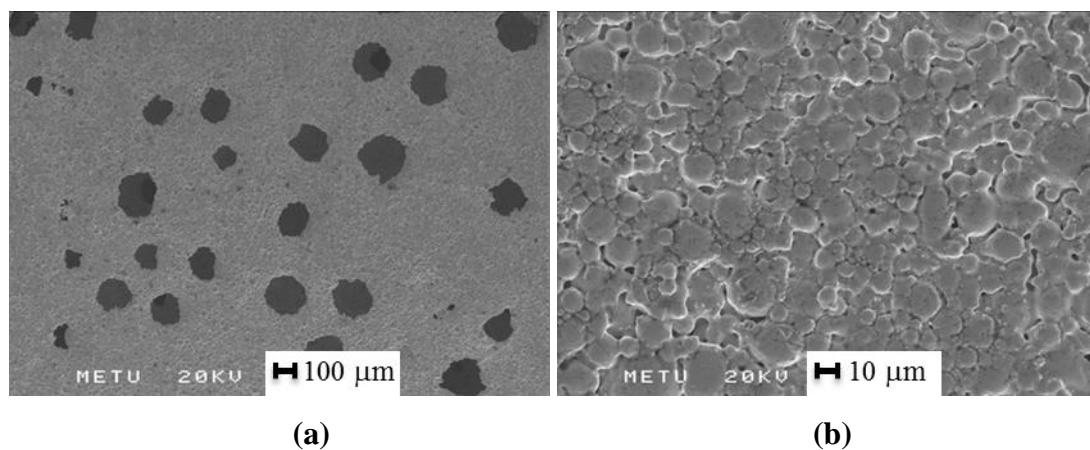
Figure 4.20 SEM micrographs showing (a) the general structure of the pores, (b) the neck region between two pores; in a TiNi foam that was endured the fatigue test for 10^6 cycles.

The fatigue tests that were performed with a frequency of 5 Hz resulted in strains varying in a range corresponding to the applied stress cycles with a ratio ($\sigma_{min}/\sigma_{max}$) of 0.1 (Figure 4.21). The general trend of the strain response has displayed all three stages of deformation (given as A, B, and C in Figure 4.21) generally reported in literature to be observed in cellular materials [77, 81, 93]. As expected, initially

observed inelastic strains were followed by the accumulation of the minimal strains leading to the sudden failure when critical number of cycles was reached. The so called inelastic strains observed at the first stage (stage A in Figure 4.21), which increase rapidly, are believed to have occurred due to the plastic deformation of the pore walls that were subjected to stresses higher than the yield point because of their favorable alignment with respect to the loading axis. The minimal strain accumulation that manifest itself as the smooth increase of the strain response with a constant slope at stage B in Figure 4.21, on the other hand, was attributed to the formation of the micro-cracks at the edges of the pores, which were subjected to higher stresses due to either their smaller cross-sectional area or their orientation. Finally those micro-cracks seem to have combined at the critical number of cycles and caused the ultimate failure of the foam (stage C in Figure 4.21).
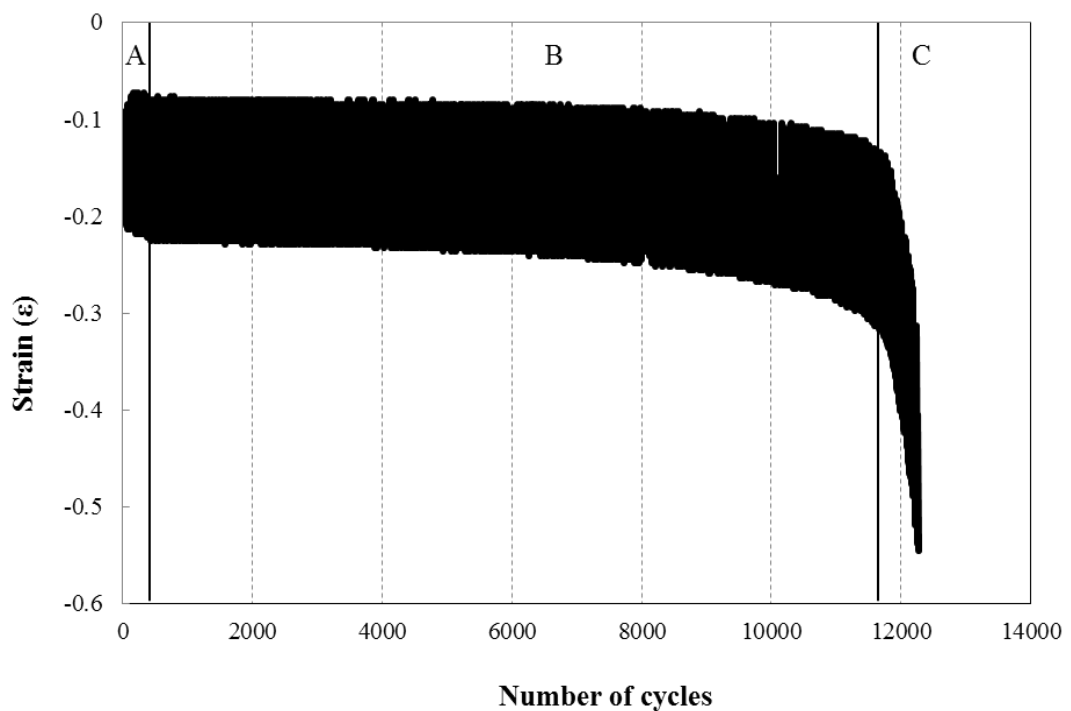
Figure 4.21 The result of the fatigue test performed at 0.9 σ_y maximum stress for the TiNi foam with 58 vol% porosity.

There are several criteria reported in literature to evaluate the fatigue life of porous metals as knee-formation point [77], the failure of the specimen [73], or the point where a certain percentage of overall deformation has been observed [82]. For the characterization of fatigue behavior of processed TiNi foams, the fatigue life was chosen as the number of cycles till the knee-formation, since it was considered to be more reasonable to evaluate the fatigue life as the reliable point after which sudden failure occurs. In addition, the knee-formation point is a more explicit criterion to compare the fatigue life of TiNi foams with different pore ratios. Moreover, the selection of the fatigue criterion did not have a significant effect in determining the fatigue life as it is obvious from Figure 4.22. The S-N curves obtained based on this criterion are given in Figure 4.23.
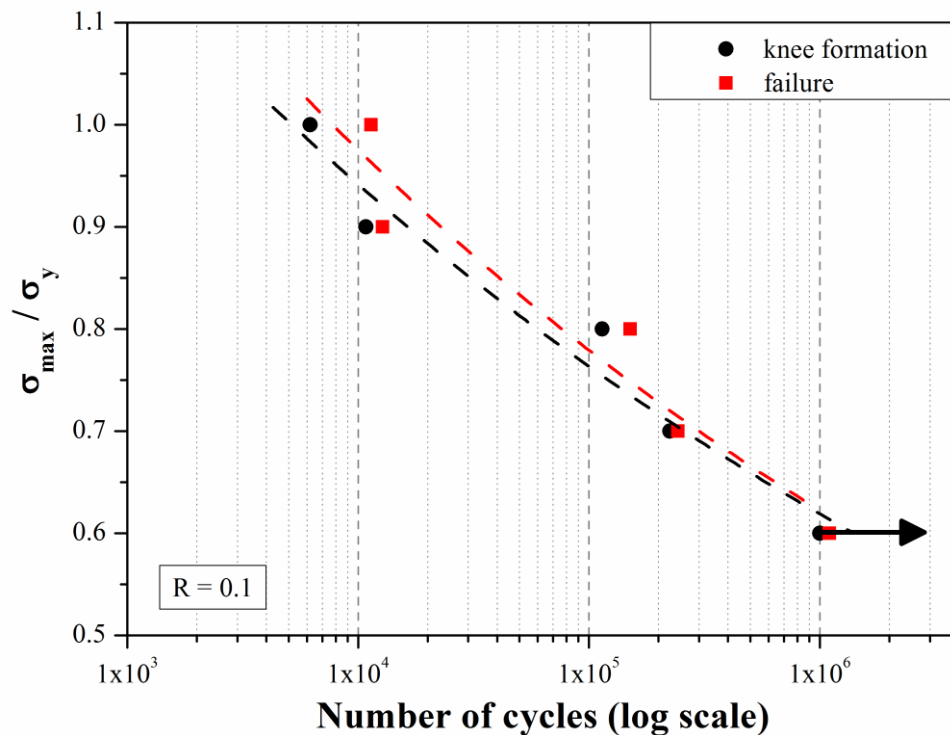
Figure 4.22 The S-N curves determined according to both criteria for TiNi foams with 58 vol% porosity.
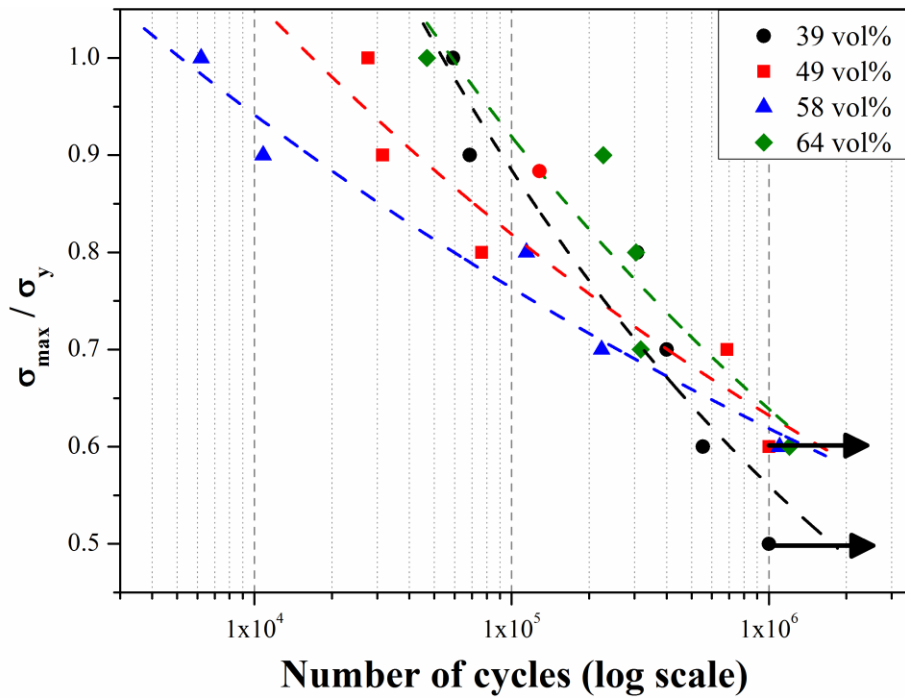
(a)
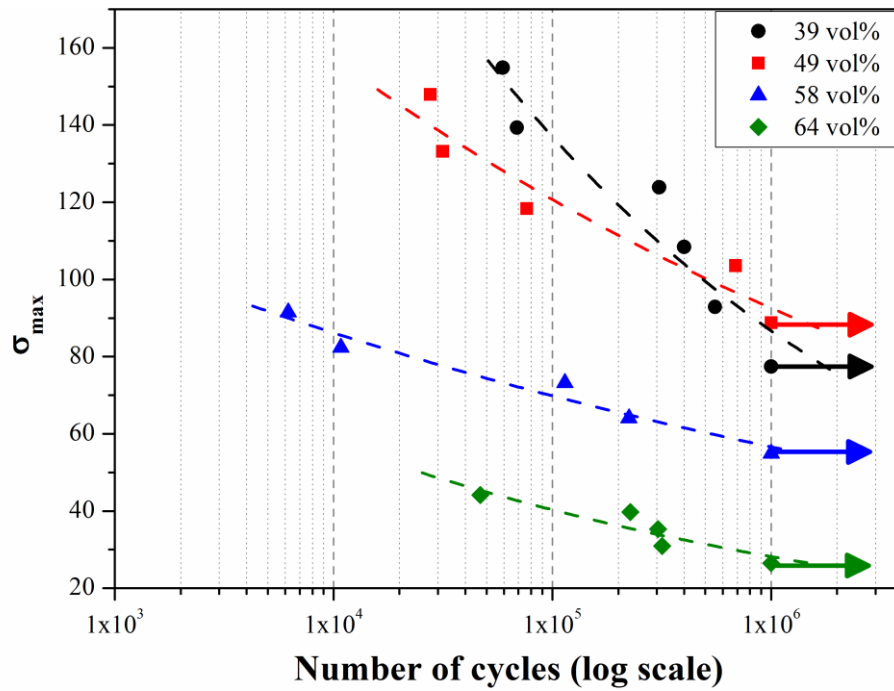
(b)

Figure 4.23 The S-N curves for different porosity contents given in terms of (a) maximum applied stress normalized to yield strength of each porosity content, (b) maximum applied stress.

The results of fatigue tests indicated that most of the fabricated TiNi foams have an endurance limit of 0.6 σ_y independent of the porosity except TiNi foams with 39 vol% porosity, which have an endurance limit of 0.5 σ_y. In addition, it was found that the fatigue lives of processed TiNi foams at any specific σ_{max} / σ_y value display scattering uncorrelated with the porosity content. The scattering was believed to occur due to the statistical nature of the fatigue tests, which would yield scattering in the number of cycles to failure as much as one log cycle even for bulk metals [94]. On the other hand, Dieter has mentioned that the fatigue limit of 95 % of specimens, which were prepared from the same forged and heat treated alloy steel, can vary in the range of 280-360 MPa. Moreover, Shigley mentioned that the endurance limit of several metals display a standard deviation in the range of 4-10% [95].
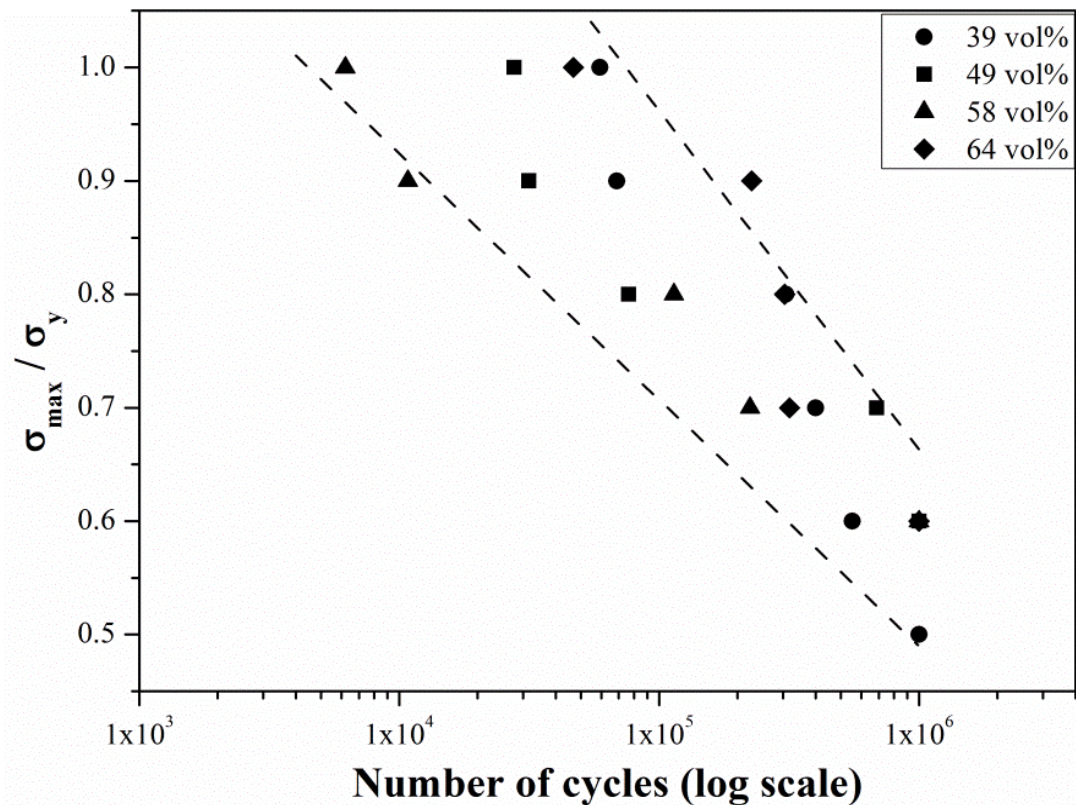
Figure 4.24 Fatigue life range of TiNi foams for different σ_{max} / σ_y ratios.

Accordingly, it can be said that the fatigue lives of the processed foams varies within a band (given as dashed lines in Figure 4.24), which has a width decreasing with decreasing σ_{max} / σ_y yielding an endurance limit ranging in between 26-89 MPa. The endurance limit of the processed foams were found to be much higher than that of TiNi foams processed by SHS [57], which is the only study that report actual fatigue data. On the other hand, for all porosity levels endurance limit values (Table 4.4) were found to be above the critical stress level range that an implant is usually subjected to [96].

Table 4.4 Endurance limits of TiNi foams with different pore ratios.

Porosity (%)	Endurance Limit (MPa)
39	77.42
49	88.76
58	54.90
64	26.47

The fracture surfaces 45° to the fatigue loading direction were examined and recorded so that the loading direction is vertical to the fractographs as given in Figure 4.25 (a). Failure of the fatigue tested foams was observed to occur by the formation of macro-cracks at the pore walls aligned at 45° along the specimen with respect to the loading axis ("A" in Figure 4.25 (a)). These macro-cracks were observed to form as a result of the coalescence of micro-cracks developed at the pore surfaces leading to the collapse of pore walls as shown with "B" in Figure 4.25 (b).

(a)   (b)
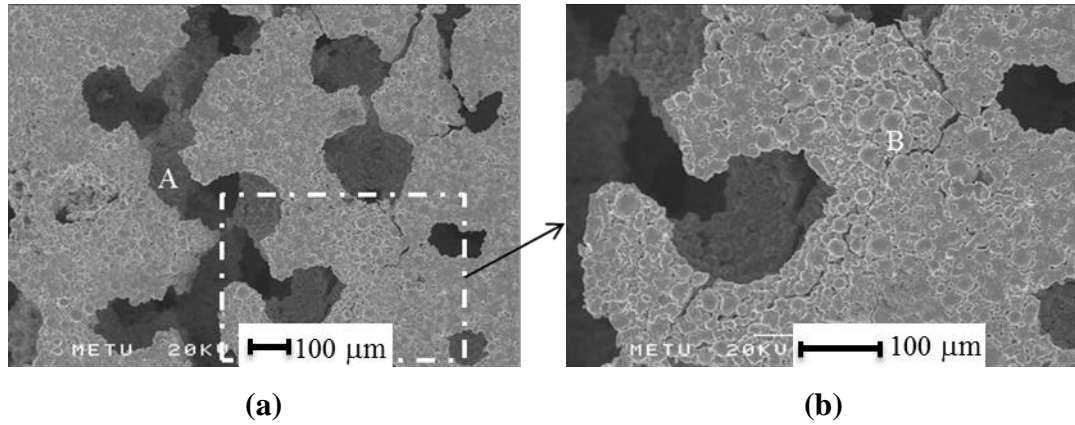
Figure 4.25 (a) Macro-crack formation (marked as "A") by the coalescence of the (b) micro-cracks (marked as "B") that are originated from the pore edges.

It was also observed that the initiated micro-crack generally prefers to propagate transversely across the necks formed between the TiNi powders (Frame A in Figure 4.26). However, it sometimes advances through the bulk of the powders cutting it up as shown in Figure 4.26 (Frame B).
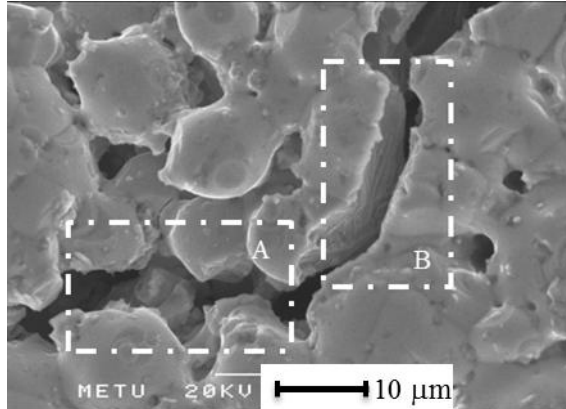
Figure 4.26 Variation of the path of a propagating micro-crack.

The variation in the micro-crack growth paths is reasonable considering the complex loading system that the fatigue test specimen was subjected to. The mechanical response of the porous TiNi alloys is different than their bulk counterparts, since the random orientation of the pore walls with respect to the main loading direction

changes the type of loading that is encountered. Therefore, the path of the advancing micro-crack also depends on the orientation of the sintering neck with respect to the loading direction.
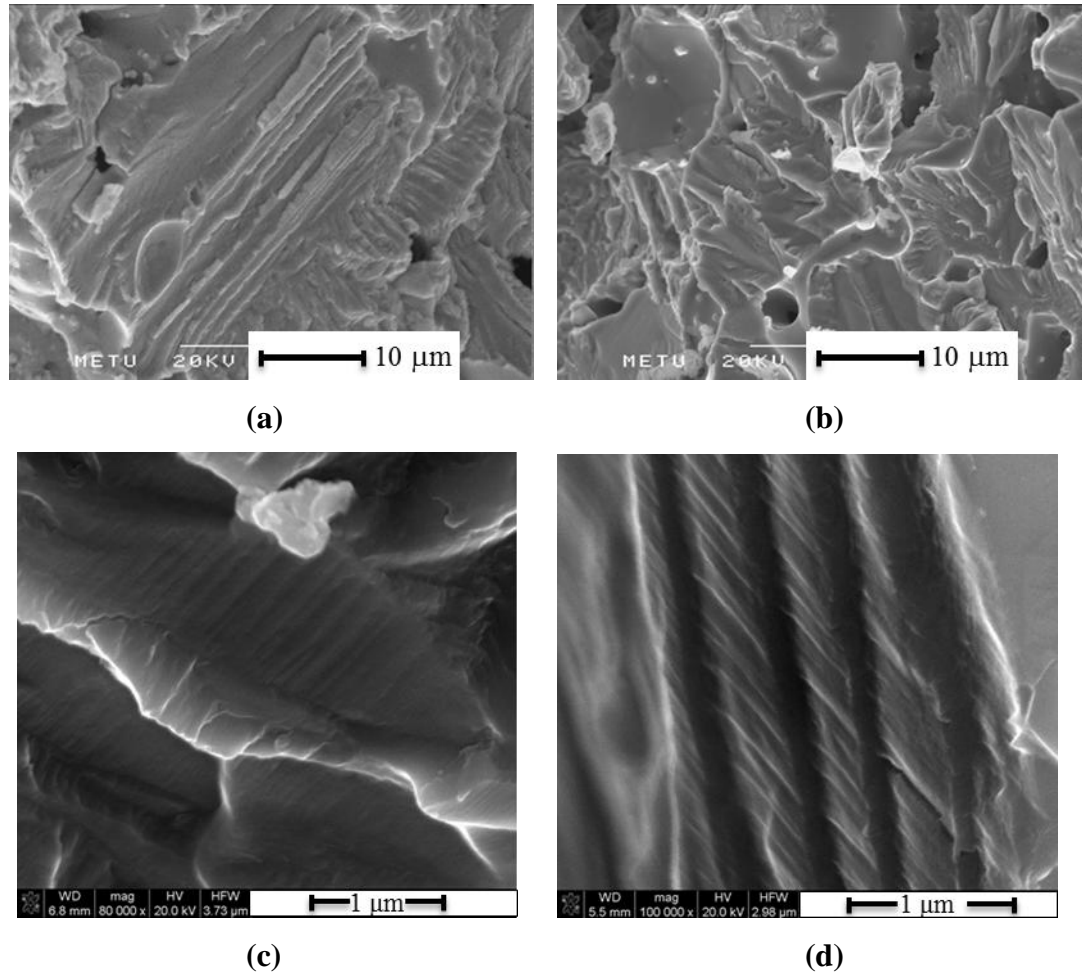
Figure 4.27 Fatigue fracture surfaces showing (a, c) parallel tear ridges, (b) tear ridges aligned in different directions, (d) striation marks.

Although there is a complex loading system composed of compression, bending and torsion modes operating on the individual necks during the fatigue tests, there was no indication of brittle fracture. According to the SEM investigations conducted both at low and high magnifications, the fracture surface generally consists of parallel tear ridges (Figure 4.27 (a), (b), (c)), showing also striation marks in some

regions (Figure 4.27 (d)). It was observed that there was more than one favorable direction for the alignment of tear ridges as shown in Figure 4.27 (b). Variation in the orientation of the tear ridges was attributed to the complexity of the loading modes operative on the necks with random alignment and varying cross-sectional area.

4.4. The Effects of Sintering Temperature and Time

Due to its diffusional nature, sintering ratio changes according to a power law t^n, where n is usually ½, with time whereas a logarithmic change was observed with temperature. Owing to this fact, sintering temperature increased to 1250 °C and microporosity was nearly eliminated with this alteration as it was confirmed by SEM analysis (Figure 4.28) and porosity measurements (Table 4.5).

(a)   (b)
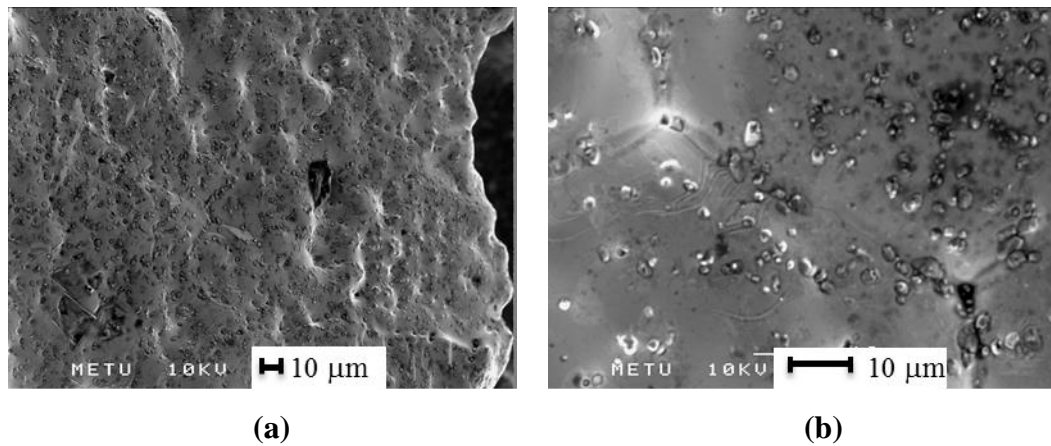
Figure 4.28 SEM images of: (a) The general view, (b) Detailed view indicating the boundaries of powders and microporosity for Ti-50.8 at%Ni foam sintered at 1250 ^{o}C for 2 hours.

Table 4.5 The change in porosity with the amount of Mg added for 50.8 at%Ni foam sintered at 1250°C for 2 hours.

% Mg added	Porosity (%)
50	46
60	55
70	61

The effect of the improvement achieved by increasing sintering temperature to 1250 °C on the mechanical properties was also evaluated by uniaxial compression tests. The results of two tests carried on Ti-50.8 at%Ni foams having the same Mg addition (60 vol%) but sintered with different procedures were given in Figure 4.29. It was observed that strength increased upon increasing the sintering temperature while maintaining the elastic modulus almost unchanged.
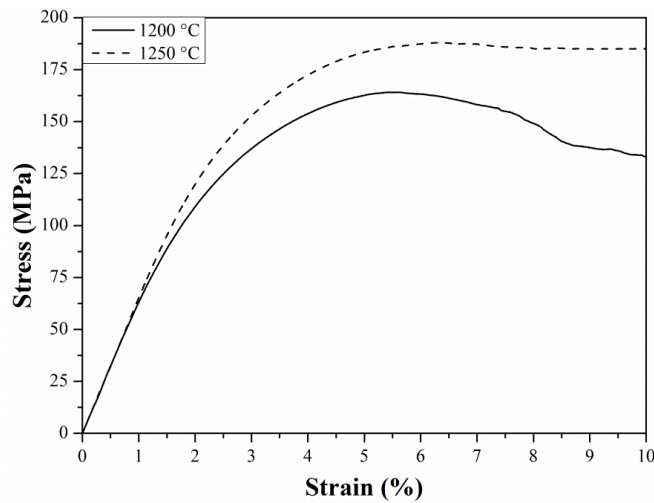
Figure 4.29 The effect of sintering temperature on the mechanical properties.

On the other hand, the effect of sintering time at elevated temperature on mechanical properties was investigated by processing porous Ti-50.8 at%Ni alloys (with 60 vol% Mg addition) via sintering at 1200°C for 4 hours. It was expected to observe a similar change in mechanical behavior as in the previous case although not being so

distinctive. However, it was observed that the ductility was decreased even though the strength was increased (Figure 4.30). That unexpected behavior was attributed to the oxidation of the TiNi foam due to the prolonged sintering time.
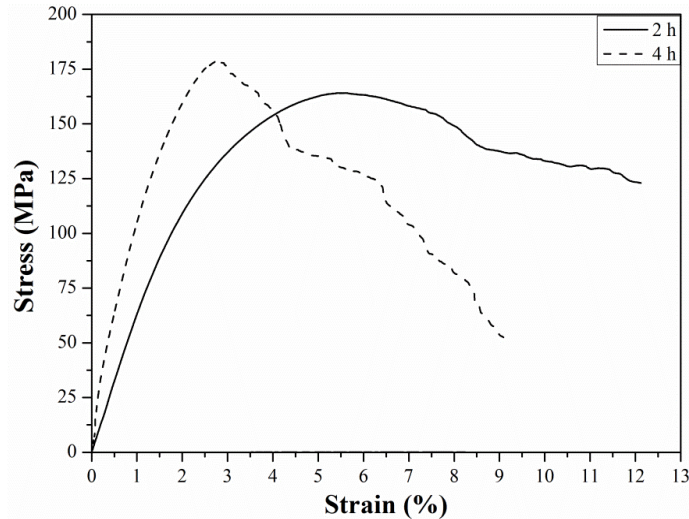
Figure 4.30 The effect of sintering time on the mechanical properties.

4.5. The Effects of Heat Treatment

The presence of Ti_3Ni_4 precipitates considerably affects the mechanical behavior of TiNi foams as mentioned before. Accordingly, heat treatment studies were conducted on processed TiNi foams. Homogenized TiNi foams with 49 vol% porosity were heat treated at four different routes and the increment of Ti_3Ni_4 content with increasing heat treatment time was observed at two different temperatures as revealed by XRD analysis (Figure 4.31). The results of XRD analyses did not give any distinguishable difference for Ti_3Ni_4 content with altering heat treatment temperature for the same duration. On the other hand, presence of Ti_4Ni_2O in small quantities was also detected after aging treatment of TiNi foams sealed in quartz tubes.
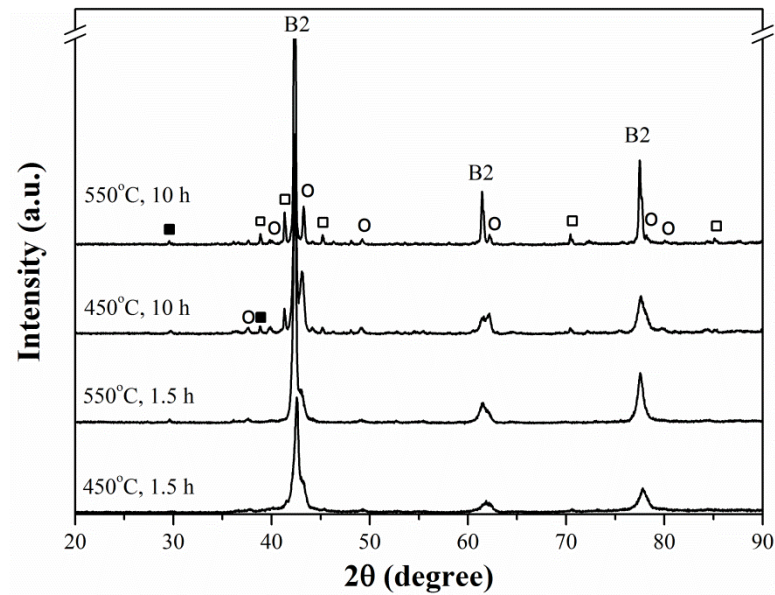
Figure 4.31 Results of XRD analysis for heat treated TiNi foams
(White circles: Ti_3Ni_4, white squares: Ti_4Ni_2O, and black squares: MgO)

The aged TiNi foams were also analyzed with SEM but Ti_3Ni_4 precipitates, which were formed as the result of aging at 450 °C for 1.5 h, cannot be observed due to their small size and selective oxidation during specimen preparation. However, it was observed that the size of the precipitates was increased by temperature enabling the detection of precipitate size and shape. It was revealed that Ti_3Ni_4 precipitates have uniform distribution in the matrix instead of localization at grain boundaries (Figure 4.32 (a)). In addition, Ti_3Ni_4 precipitates that were formed as the result of aging at 550 °C for 1.5 h were found to have sizes in the range of 300-600 nm (Figure 4.32 (b)).

(a)   **(b)**
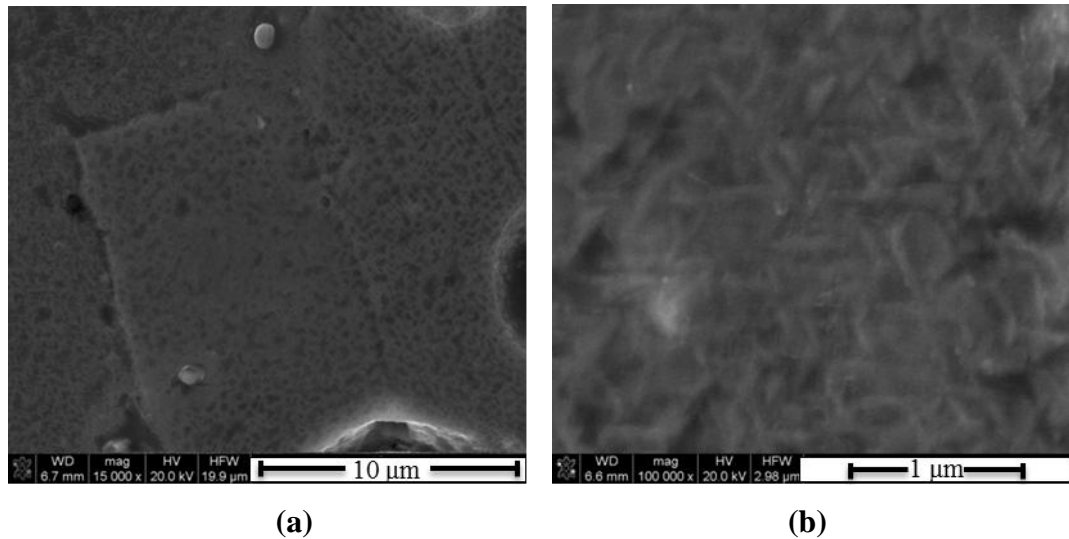
Figure 4.32 SEM micrographs representing(a) precipitate distribution, (b) size and shape of precipitates formed as the result of aging at 550 °C for 1.5 hours.

TiNi foams that were aged for 10 hours at 450 °C and 550 °C were also examined with SEM. It was observed that precipitate distribution was homogeneous (Figure 4.33 (a)) and precipitate size has increased to a range of 0.5-1.7 µm (Figure 4.33 (b)) for the foams aged at 550 °C for 10 hours. On the other hand, spherical second phase formation (Figure 4.33 (c)) was also observed in TiNi matrix after aging at 550 °C for 10 hours and according to the evaluation of EDS analysis (Figure 4.33 (d)) in combination with XRD results, this particle was presumed to be Ti_4Ni_2O phase. In addition, Ti_3Ni_4 precipitates became detectable after increasing sintering time from 1.5 to 10 h for aging at 450 °C and have a size range of 84-150 nm (Figure 4.33 (e)).
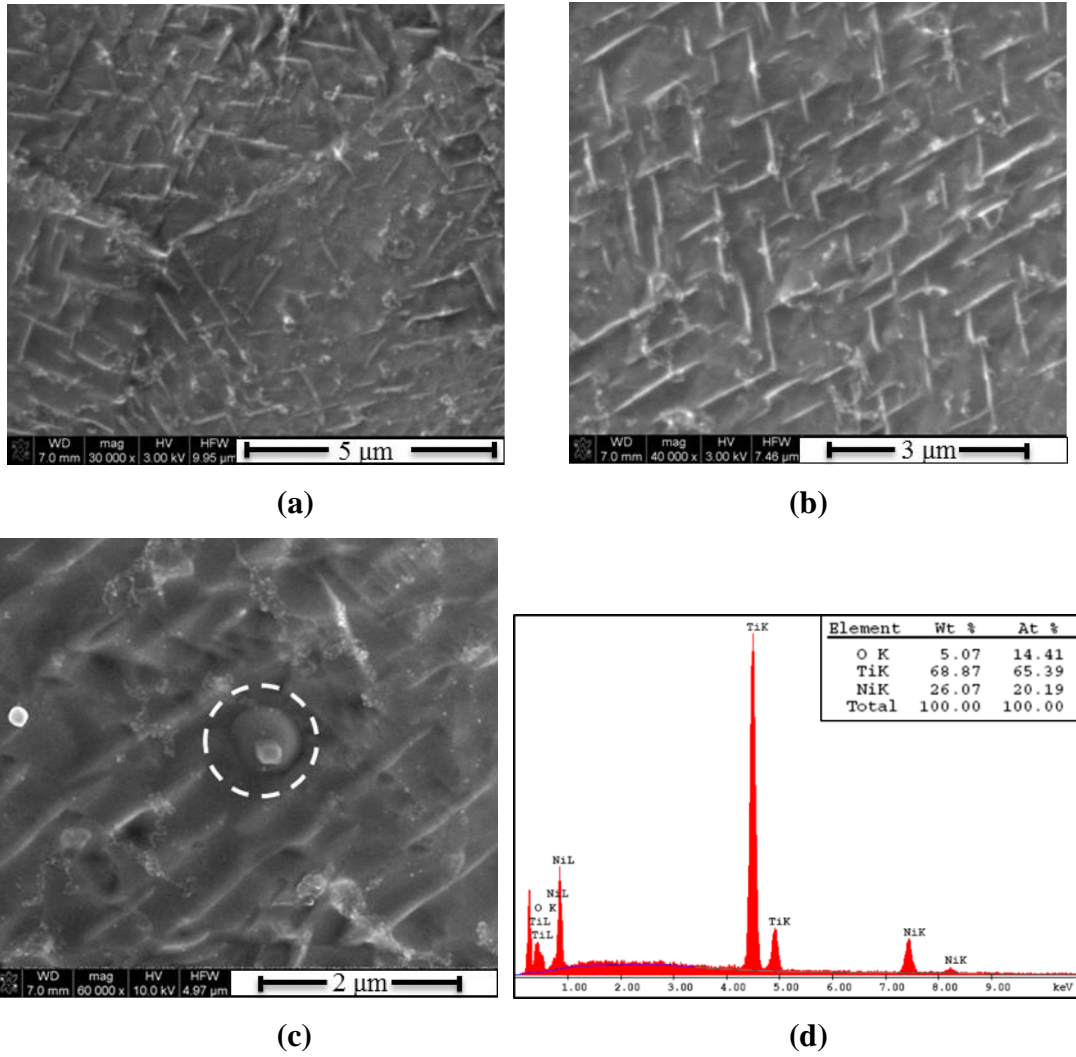
Figure 4.33 SEM micrographs representing (a) distribution, (b) size and shape of Ti_3Ni_4 precipitates after aging at 550 °C for 10 h, (c) shape of Ti_4Ni_2O precipitate formed as the result of aging at 550 °C for 10 h, (d) EDS analysis of precipitate indicated by drawn circle in (c).
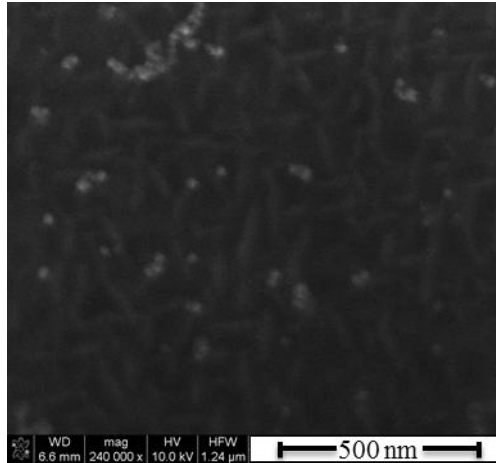
(e)

Figure 4.33 (Continued) SEM micrograph representing (e) size and shape of Ti_3Ni_4 precipitates for TiNi foams that were aged at 450 °C for 10 h.

TiNi foams with 49 vol% porosity, which were aged at 450 °C for 1.5 h, were mechanically characterized with monotonic compression and compression superelasticity tests in order to evaluate the effect of evenly distributed small precipitates. The monotonic compression behavior of aged TiNi foams were observed to be different from that of processed ones (Figure 4.34) and elastic modulus, yield strength and compressive strength values were measured as 5.85 GPa, 100 MPa and 263 MPa, respectively. When it was compared with as-processed TiNi foams with the same porosity content (49 vol%), the aging treatment has caused decrement in mechanical properties especially for yield strength while compressive strength was not so altered. Another major difference between the mechanical behavior of the as-processed and aged foams was the increased ductility after aging.
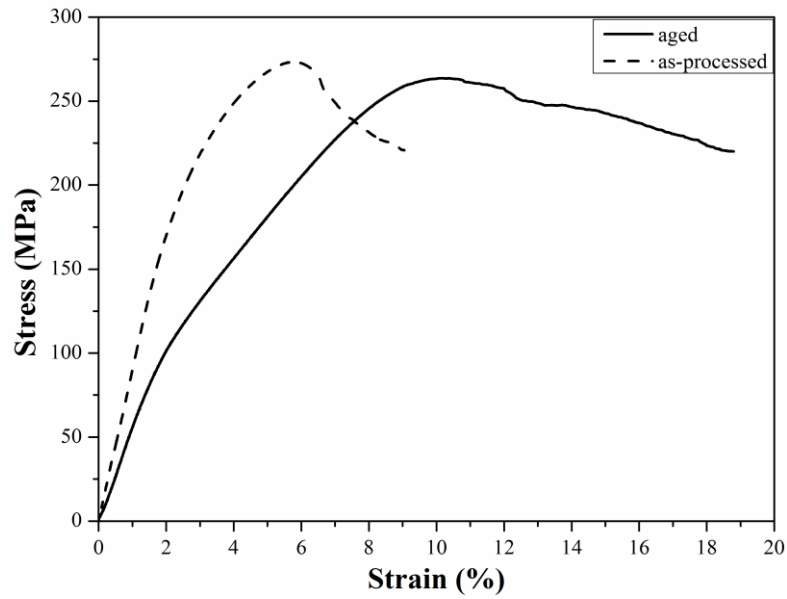
Figure 4.34 Compressive stress-strain curves of TiNi foams that were as-processed and aged at 450 °C for 1.5 h.

The superelasticity tests of aged TiNi foams with 49 vol% porosity were also conducted at 0.85 σ_{max}, which is 220 MPa while this value was 230 MPa for as-processed TiNi foams. As it is obvious from Figure 4.35, the superelasticity was improved by aging at 450 °C for 1.5 h. The four stages of deformation behavior during superelasticity tests, which were described for as-processed TiNi foams, were observed to be more distinguishable for the aged ones. In addition, the amount of recoverable strain at the end of fifth cycle, which was measured as 4.28% for as-processed TiNi foams, has increased to 5.41% by aging.
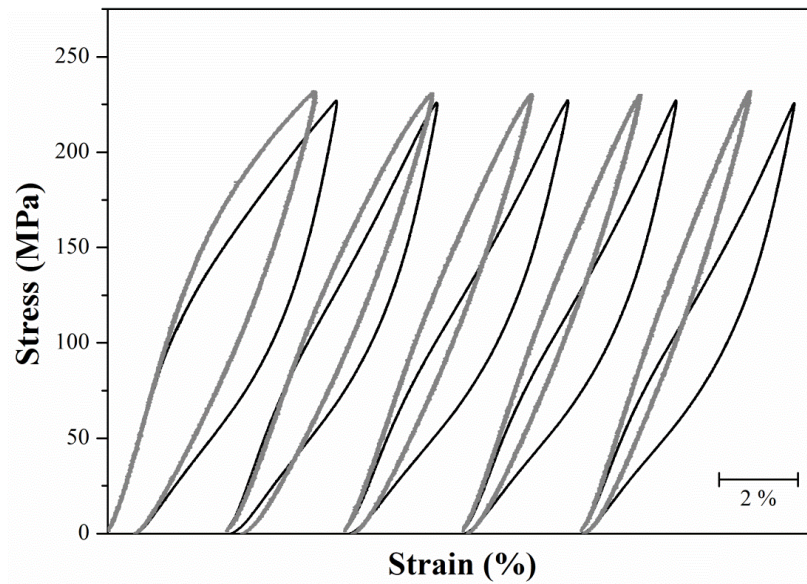
Figure 4.35 Superelasticity test results of TiNi foams with 49 vol% porosity (black lines indicated the results of aged foams while the gray lines are for as-processed ones).

To distinguish the effect of aging on mechanical behavior with that of homogenization, homogenized foams were also tested under both monotonic and superelastic compression. The results of monotonic compression tests of homogenized foams were given in Figure 4.36 together with that of as-processed and aged TiNi foams. As it is obvious from the figure, the monotonic compression behavior was similar for the as-processed and homogenized foams while aging has abruptly changed the mechanical parameters as given in Table 4.6. It can be said that homogenization resulted in increase of elastic modulus and yield strength. When the mechanical parameters of TiNi foams obtained at different conditions (as-processed, homogenized, aged) were compared with each other, it was observed that the elastic modulus and yield strength were highly sensitive to the presence and amount of precipitates while the compressive strength remain almost unaffected.
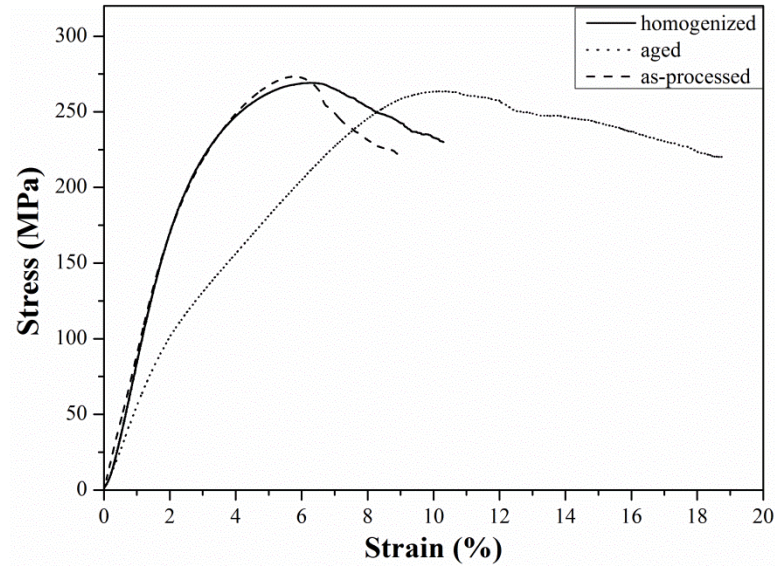
Figure 4.36 The compressive stress-strain curves of TiNi foams with 49 vol% porosity for different conditions.

Table 4.6 Mechanical properties of TiNi foams with 49 vol% porosity tested in compression, where E is Young's modulus, σ_y is yield strength, σ_{max} is compressive strength.

Condition	E (GPa)	σ_y (MPa)	σ_{max} (MPa)
As-processed	8.71	147.93	273.45
Homogenized	10.14	187.90	269.17
Aged	5.85	99.50	263.14

On the other hand, superelastic response was abruptly changed after homogenization as given in Figure 4.37. The shape of loading-unloading curves was similar to that of as-processed specimens while the full recovery was attained after only two cycles of training. However, the amount of maximum attainable strain at 0.85 σ_{max} and accordingly the recoverable strain was decreased after homogenization (Figure 4.38).
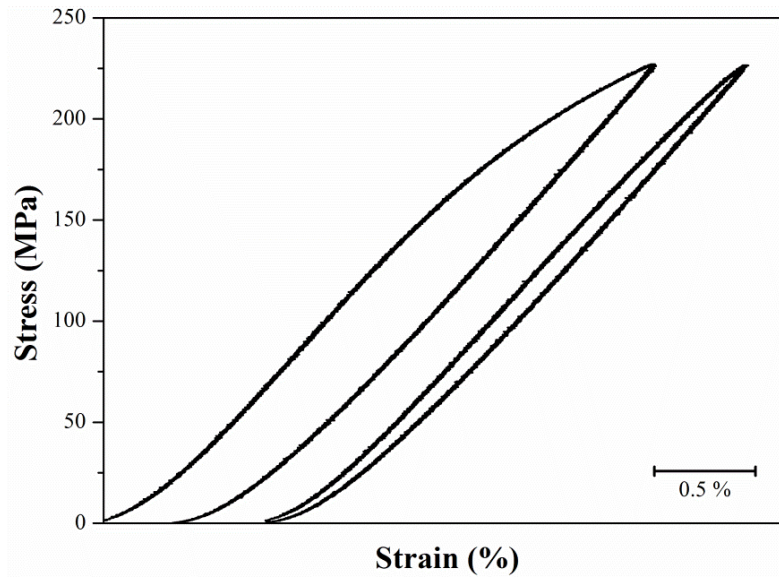
Figure 4.37 Superelastic response of homogenized TiNi foams.
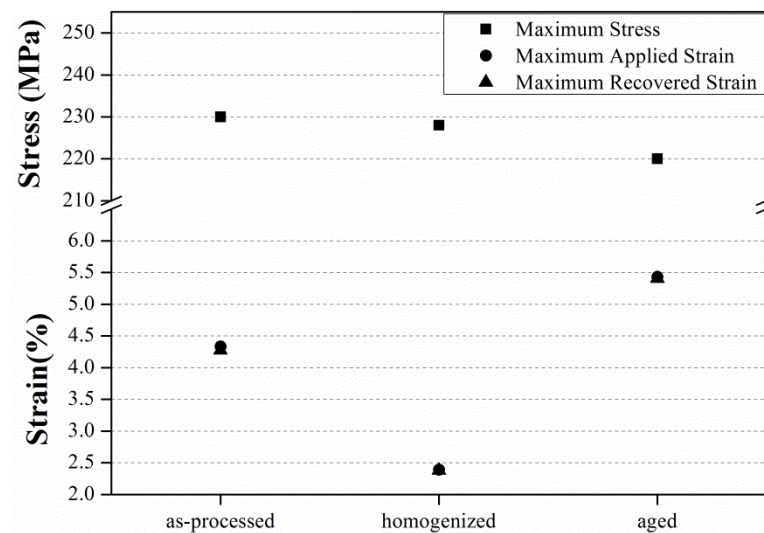
Figure 4.38 The change of maximum applied and recoverable strain after training at 0.85 σ_{max} for TiNi foams with different heat treatment histories.

When the superelasticity test results of homogenized TiNi foams were compared with the previously obtained results for as-processed and aged foams, it was concluded that the presence of Ti_3Ni_4 precipitates improves the superelastic response

although it increases the energy requirement of martensitic and reverse transformations (increase in hysteresis of loading-unloading curves).

When both the monotonic compression and superelasticity test results were compared with the given data in literature, it was observed that TiNi foams, which were processed by magnesium space holder technique, display higher mechanical properties under monotonic compression as well as better superelastic recovery values than most of TiNi foams with similar porosity content but were processed with other techniques reported in literature [10, 38, 39, 41, 44, 46, 51, 54, 60, 65]. Among different techniques, MIM and microwave sintering seemed to provide similar and even better superelastic response than TiNi foams processed in this study [49, 62]. However, the reported improvement was due to the small size of pores (<250 μm) obtained with these techniques. When it was considered that the main application field of TiNi foams is the biomedical applications such as implants, the pore size of TiNi foams processed with MIM and/or microwave sintering did not seem suitable even if the superelasticity was improved. On the other hand, processed TiNi foams with 64 vol% porosity displayed lower yield and compression strength than Actipore® although having higher ductility [57]. Moreover, higher superelasticity was reported for TiNi foams processed by some of the other space holder techniques [43, 68, 71]. However, the secondary intermetallic formation was the common drawback for the processed TiNi foams with the mentioned techniques.

CHAPTER 5

CONCLUSIONS

1. . Porous Ti-50.8 at%Ni alloys were processed with Mg space holder technique from prealloyed powder by sintering at 1200 °C for 2 h. Total porosity measured, which is the sum of macropores that created by evaporation of Mg and micropores that retained between powders, was found to be lower than amount of magnesium added. Moreover, Ti-50.8 at%Ni foams with four different porosity contents in the range of 39-64 vol% were found to contain less than 1 % closed porosity mainly due to the isolated micropores while the spherical macropores, which were created by evaporation of Mg during sintering, displayed homogeneous distribution with interconnections.

2. XRD and SEM analyses indicated that processed TiNi foams were in fully austenitic state at room temperature. However, TEM studies revealed the presence of Ti_3Ni_4 precipitates, which were formed due to insufficient cooling rate after sintering.

3. The processed TiNi foams were mechanically characterized by monotonic and superelasticity compression tests as well as fatigue tests. It was observed that stress required to trigger martensitic transformation was decreased with increasing porosity. Similarly, the elastic moduli and ultimate compressive strength were also inversely related to the porosity content as expected. It was observed that the foams behaved as a composite structure composed of TiNi and macropores when the porosity content was low. As the porosity content has increased, the struts became more effective and deformation proceeded by the collapse of favorable struts.

4. Superelasticity tests were conducted at 0.85 σ_{max}, ultimate compressive strength of each foam with the corresponding porosity level. It was concluded from superelasticity tests results that maximum reached and recovered strain values at the end of fifth cycle increase while the fraction of strain recovered at the end of fifth cycle decreases with decreasing porosity content.

5. The role of training during superelasticity tests was also analyzed on two TiNi foams with same porosity content: one with previously trained at a lower stress level (120 MPa) and the other did not. When the two foams were trained at 150 MPa for 5 cycles, it was observed that both the the maximum achieved and recovered strain values was higher for untrained (directly tested) foam.

6. The fatigue tests were performed with a frequency of 5 Hz and stress ratio (σ_{min}/ σ_{max}) of 0.1. The general trend of the strain response has displayed all three stages of deformation generally reported in literature to be observed in cellular materials. The endurance limit, which was determined as the stress level at which the specimens sustain their integrity without showing any sign of failure beyond 10^6 cycles, was found to range in between 26-89 MPa.

7. SEM analyses conducted on fracture surfaces indicated that failure of the fatigue tested foams occurred by the formation of macro-cracks at the pore walls aligned at 45° along the specimen with respect to the loading axis. These macro-cracks, on the other hand, were observed to form as a result of the coalescence of micro-cracks developed at the pore surfaces leading to the collapse of pore walls. Furthermore, the fracture surface was observed to consist of parallel tear ridges generally, showing also striation marks in some regions. Parallel tear ridges were observed to follow preferred directions, probably along the planes having higher resolved shear stress.

8. The effect of heat treatment on mechanical behavior was also analyzed and it was found that the homogenization has resulted in increase of elastic modulus and yield strength while aging has improved the superelastic response.

REFERENCES

[1] Z. Esen, Ş. Bor, Processing of Titanium Foams Using Magnesium Spacer Particles, Scripta Materialia. 56 (2007) 341-344.

[2] C. Leyens, M. Peters, Titanium and Titanium Alloys (2003).

[3] M.A. Iadicola, J.A. Shaw, The Effect of Uniaxial Cyclic Deformation on the Evolution of Phase Transformation Fronts in Pseudoelastic NiTi Wire, Journal of Intelligent Material Systems and Structures. 13 (2002) 143-155.

[4] A. Ishida, M. Sato, A. Takei, S. Miyazaki, Effect of Heat Treatment on Shape Memory Behavior of Ti-rich Ti-Ni Thin Films Materials Transactions, Transactions of the Japan Institute of Metals. 36 (1995) 1349-1355.

[5] D. Goldstein, A Source Manual for Information on NITINOL and TiNi, Naval Surface Weapons Center. NSWC/WOL/TR-78-26 (1978).

[6] K. Otsuka, X. Ren, Physical Metallurgy of Ti–Ni-Based Shape Memory Alloys, Progress in Materials Science. 50 (2005) 511-678.

[7] K. Otsuka, C.M. Wayman, Shape Memory Materials, (1998).

[8] T. Tadaki, Y. Nakata, K. Shimizu, K. Otsuka, Crystal Structure, Composition and Morphologyof a Precipitate in an Aged Ti-51 at%Ni Shape Memory Alloy, Transactions of the Japan Institute of Metals. 27 (1986) 731-740.

[9] A. Harte, N.A. Fleck, M.F. Ashby, Fatigue Failure of an Open Cell and a Closed Cell Aluminium Alloy Foam, Acta Materialia. 47 (1999) 2511-2524.

[10] D.S. Li, Y.P. Zhang, G. Eggeler, X.P. Zhang, High Porosity and High-Strength Porous NiTi Shape Memory Alloys with Controllable Pore Characteristics, Journal of Alloys and Compounds. 470 (2009) L1-L5.

[11] X. Huang, G.J. Ackland, K.M. Rabe, Crystal Structures and Shape-Memory Behaviour of NiTi, Nature Materials. 2 (2003) 307-311.

[12] H. Funakubo, Shape Memory Alloys, Gordon and Breach Science Publishers (1987).

[13] G. Lütjering, J.C. Williams, Titanium, Second ed., Springer, New York (2007).

[14] R.F. Hamilton, H. Sehitoglu, Y. Chumlyakov, H.J. Maier, Stress Dependence of the Hysteresis in Single Crystal NiTi Alloys, Acta Materialia. 52 (2004) 3383-3402.

[15] D. Stöckel, The Shape Memory Effect • Phenomenon, Alloys, Applications, Nitinol Devices & Components, Inc. (2000).

[16] K. Gall, H. Sehitoglu, R. Anderson, I. Karaman, Y.I. Chumlyakov, I.V. Kireeva, On the Mechanical Behavior of Single Crystal NiTi Shape Memory Alloys and Related Polycrystalline Phenomenon, Materials Science and Engineering: A. 317 (2001) 85-92.

[17] S. Miyazaki, K. Otsuka, Development of Shape Memory Alloys, Journal of Iron and Steel Institute of Japan. 29 (1989) 353-377.

[18] J.A. Shaw, Material Instabilities in a Nickel-Titanium Shape Memory Alloy, Ph.D. Thesis (2007).

[19] H. Sehitoglu, I. Karaman, R. Anderson, X. Zhang, K. Gall, H.J. Maier, Y. Chumlyakov, Compressive Response of NiTi Single Crystals, Acta Materialia. 48 (2000) 3311-3326.

[20] K. Gall, H. Sehitoglu, The Role of Texture in Tension–Compression Asymmetry in Polycrystalline NiTi, International. Journal of Plasticity. 15 (1999) 69-92.

[21] S. Miyazaki, T. Imai, Y. Igo, K. Otsuka, Effect of Cyclic Deformation on the Pseudoelasticity Characteristics of Ti-Ni Alloys, Metallurgical and Materials Transactions A. 17 (1986) 115-120.

[22] H. Sehitoglu, R. Anderson, I. Karaman, K. Gall, Y. Chumlyakov, Cyclic Deformation Behavior of Single Crystal NiTi, Materials Science and Engineering: A. 314 (2001) 67-74.

[23] J.A. Shaw, Simulations of Localized Thermo-Mechanical Behavior in a NiTi Shape Memory Alloy, International. Journal of Plasticity. 16 (2000) 541-562.

[24] S. Nemat-Nasser, J. Choi, W. Guo, J.B. Isaacs, Very High Strain-Rate Response of a NiTi Shape-Memory Alloy, Mechanics of Materials. 37 (2005) 287-298.

[25] X.W. Huang, G.N. Dong, Z.R. Zhou, Y.B. Xie, Mechanical Behavior of TiNi Shape Memory Alloy under Axial Dynamic Compression, Journal of Materials Science. 40 (2005) 1059-1061.

[26] T. Saburi, S. Nenno, Y. Nishimoto, M. Zeniya, Effects of Thermo-Mechanical Treatment on the Shape Memory Effect and the Pseudoelasticity of Ti--50.2Ni and Ti-47.5Ni--2.5Fe Alloys , Journal of Iron and Steel Institute of Japan. 72 (1986) 571-578.

[27] J. Beyer, Recent Advances in the Martensitic Transformations of Ti-Ni Alloys, Journal de Physique IV. 5 (1995) 433-442.

[28] X. Huang, Y. Liu, Effect of Annealing on the Transformation Behavior and Superelasticity of NiTi Shape Memory Alloy, Scripta Materialia. 45 (2001) 153-160.

[29] Y. Chumlyakov, S. Efimenko, I. Kireeva, E. Panchenko, H. Sehitogly, K. Gall, H. Yahia, Effects of Shape Memory and Superelasticity in Aged TiNi Single Crystals, Doklady Physics. 46 (2001) 849-852.

[30] K. Gall, N. Yang, H. Sehitoglu, Y.I. Chumlyakov, Fracture of Precipitated NiTi Shape Memory Alloys, International Journal of Fracture. 109 (2001) 189-207.

[31] G. Fan, W. Chen, S. Yang, J. Zhu, X. Ren, K. Otsuka, Origin of Abnormal Multi-Stage Martensitic Transformation Behavior in Aged Ni-rich Ti–Ni Shape Memory Alloys, Acta Materialia. 52 (2004) 4351-4362.

[32] A. Dlouhy, J. Khalil-Allafi, G. Eggeler, Multiple-Step Martensitic Transformations in Ni-Rich NiTi Alloys--an in-situ Transmission Electron Microscopy Investigation, Philosophical Magazine. 83 (2003) 339-363.

[33] C. Eijk, Z. Zhang, O.M. Akselsen, Seismic Dampers Based On Shape Memory Alloys: Metallurgical Background And Modelling, Proceedings of the Third European Conference on Structural Control, 3ECSC (2004).

[34] H. Kahn, M.A. Huff, A.H. Heuer, The TiNi Shape-Memory Alloy and its Applications for MEMS, Journal of Micromechanics and Microengineering. 8 (1998) 213-221.

[35] Y. Fu, H. Du, W. Huang, S. Zhang, M. Hu, TiNi-based Thin Films in MEMS Applications: a Review, Sensors and Actuators A: Physical. 112 (2004) 395-408.

[36] S.A. Shabalovskaya, Surface, Corrosion and Biocompatibility Aspects of Nitinol as an Implant Material, Bio-Medical Materials and Engineering. 12 (2002) 69-109.

[37] L. Petrini, F. Migliavacca, Biomedical Applications of Shape Memory Alloys, Journal of Metallurgy. (2011) Article ID 501483.

[38] S. Wu, C.Y. Chung, X. Liu, P.K. Chu, J.P.Y. Ho, C.L. Chu, Y.L. Chan, K.W.K. Yeung, W.W. Lu, K.M.C. Cheung, K.D.K. Luk, Pore Formation Mechanism and Characterization of Porous NiTi Shape Memory Alloys Synthesized by Capsule-Free Hot Isostatic Pressing, Acta Materialia. 55 (2007) 3437-3451.

[39] B. Yuan, C.Y. Chung, P. Huang, M. Zhu, Superelastic Properties of Porous Tini Shape Memory Alloys Prepared by Hot Isostatic Pressing, Materials Science and Engineering: A. 438–440 (2006) 657-660.

[40] P. Bassani, P. Giuliani, A. Tuissi, C. Zanotti, Thermomechanical Properties of Porous NiTi Alloy Produced by SHS, Journal of Materials Engineering and Performance. 18 (2009) 594-599.

[41] S. Wisutmethangoon, N. Denmud, L. Sikong, Characteristics and Compressive Properties of Porous NiTi Alloy Synthesized by SHS Technique, Materials Science and Engineering: A. 515 (2009) 93-97.

[42] Y. Zhao, M. Taya, Y. Kang, A. Kawasaki, Compression Behavior of Porous NiTi Shape Memory Alloy, Acta Materialia. 53 (2005) 337-343.

[43] M. Bram, M. Köhl, H. Buchkremer, D. Stöver, Mechanical Properties of Highly Porous NiTi Alloys, Journal of Materials Engineering and Performance. 20 (2011) 522-528.

[44] H. Li, B. Yuan, Y. Gao, C. Chung, M. Zhu, High-Porosity NiTi Superelastic Alloys Fabricated by Low-Pressure Sintering using Titanium Hydride as Pore-Forming Agent, Journal of Materials Science. 44 (2009) 875-881.

[45] B. Yuan, M. Zhu, Y. Gao, X. Li, C.Y. Chung, Forming and Control of Pores by Capsule-Free Hot Isostatic Pressing in NiTi Shape Memory Alloys, Smart Materails and Structures. 17 (2008) 025013.

[46] D.C. Lagoudas, E.L. Vandygriff, Processing and Characterization of NiTi Porous SMA by Elevated Pressure Sintering, Journal of Intelligent Material Systems and Structures. 13 (2002) 837-850.

[47] G. Tosun, L. Ozler, M. Kaya, N. Orhan, A Study on Microstructure and Porosity of NiTi Alloy Implants Produced by SHS, Journal of Alloys and Compounds. 487 (2009) 605-611.

[48] B.Y. Li, L.J. Rong, Y.Y. Li, V.E. Gjunter, Synthesis of porous Ni–Ti shape-memory alloys by self-propagating high-temperature synthesis: reaction mechanism and anisotropy in pore structure, Acta Materialia. 48 (2000) 3895-3904.

[49] H. Guoxin, Z. Lixiang, F. Yunliang, L. Yanhong, Fabrication of high porous NiTi shape memory alloy by metal injection molding, Journal of Materials Processing Technology. 206 (2008) 395-399.

[50] L. Krone, J. Mentz, M. Bram, H.-. Buchkremer, D. Stöver, M. Wagner, G. Eggeler, D. Christ, S. Reese, D. Bogdanski, M. Köller, S. Esenwein, G. Muhr, O. Prymak, M. Epple, The Potential of Powder Metallurgy for the Fabrication of Biomaterials on the Basis of Nickel-Titanium: A Case Study with a Staple Showing Shape Memory Behaviour, Advanced Engineering Materials. 7 (2005) 613-619.

[51] B. Yuan, X. Zhang, M. Zhu, M. Zeng, C. Chung, A Comparative Study of the Porous TiNi Shape-Memory Alloys Fabricated by Three Different Processes, Metallurgical and Materials Transactions A. 37 (2006) 755-761.

[52] S.L. Zhu, X.J. Yang, F. Hu, S.H. Deng, Z.D. Cui, Processing of Porous TiNi Shape Memory Alloy from Elemental Powders by Ar-Sintering, Materials Letters. 58 (2004) 2369-2373.

[53] B. Bertheville, M. Neudenberger, J.-. Bidaux, Powder Sintering and Shape-Memory Behaviour of NiTi Compacts Synthesized from Ni and TiH$_2$, Materials Science and Engineering A. 384 (2004) 143-150.

[54] A. Bansiddhi, D.C. Dunand, Shape-Memory NiTi Foams Produced by Solid-State Replication with NaF, Intermetallics. 15 (2007) 1612-1622.

[55] T. Aydogmus, S. Bor, Processing of Porous TiNi Alloys using Magnesium as Space Holder, Journal of Alloys and Compounds. 478 (2009) 705-710.

[56] C. Greiner, S.M. Oppenheimer, D.C. Dunand, High Strength, Low Stiffness, Porous NiTi with Superelastic Properties, Acta Biomaterialia. 1 (2005) 705-716.

[57] P. Sevilla, C. Aparicio, J.A. Planell, F.J. Gil, Comparison of the Mechanical Properties between Tantalum and Nickel–Titanium Foams Implant Materials for Bone Ingrowth Applications, Journal of Alloys and Compounds. 439 (2007) 67-73.

[58] X.P. Zhang, H.Y. Liu, B. Yuan, Y.P. Zhang, Superelasticity Decay of Porous NiTi Shape Memory Alloys under Cyclic Strain-Controlled Fatigue Conditions, Materials Science and Engineering: A. 481–482 (2008) 170-173.

[59] M.D. McNeese, D.C. Lagoudas, T.C. Pollock, Processing of TiNi from Elemental Powders by Hot Isostatic Pressing, Materials Science and Engineering: A. 280 (2000) 334-348.

[70] Y. Li, L. Rong, Y. Li, Compressive Property of Porous NiTi Alloy Synthesized by Combustion Synthesis, Journal of Alloys and Compounds. 345 (2002) 271-274.

[61] Z. Guo, H. Xie, F. Dai, H. Qiang, L. Rong, P. Chen, F. Huang, Compressive Behavior of 64% Porosity NiTi Alloy: An Experimental Study, Materials Science and Engineering: A. 515 (2009) 117-130.

[62] M.H. Ismail, R. Goodall, H.A. Davies, I. Todd, Formation of Microporous NiTi by Transient Liquid Phase Sintering of Elemental Powders, Materials Science and Engineering: C. 32 (2012) 1480-1485.

[63] B. Bertheville, Porous Single-Phase NiTi Processed under Ca Reducing Vapor for Use as a Bone Graft Substitute, Biomaterials. 27 (2006) 1246-1250.

[64] C.Y. Tang, L.N. Zhang, C.T. Wong, K.C. Chan, T.M. Yue, Fabrication and Characteristics of Porous NiTi Shape Memory Alloy Synthesized by Microwave Sintering, Materials Science and Engineering: A. 528 (2011) 6006-6011.

[65] D.S. Li, Y.P. Zhang, X. Ma, X.P. Zhang, Space-Holder Engineered Porous NiTi Shape Memory Alloys with Improved Pore Characteristics and Mechanical Properties, Journal of Alloys and Compounds. 474 (2009) L1-L5.

[66] B. Li, L. Rong, X. Luo, Y. Li, Transformation Behavior of Sintered Porous NiTi Alloys, Metallurgical and Materials Transactions A. 30 (1999) 2753-2756.

[67] A. Bansiddhi, D.C. Dunand, Shape-Memory NiTi Foams Produced by Solid-State Replication with NaF, Intermetallics. 15 (2007) 1612-1622.

[68] A. Ghasemi, S.R. Hosseini, S.K. Sadrnezhaad, Pore Control in SMA NiTi Scaffolds via Space Holder Usage, Materials Science and Engineering: C. 32 (2012) 1266-1270.

[69] B. Li, L. Rong, Y. Li, Stress–Strain Behavior of Porous Ni–Ti Shape Memory İntermetallics Synthesized from Powder Sintering, Intermetallics. 8 (2000) 643-646.

[70] A.J. Neurohr, D.C. Dunand, Shape-Memory NiTi with Two-Dimensional Networks of Micro-Channels, Acta Biomaterialia. 7 (2011) 1862-1872.

[71] J.Y. Xiong, Y.C. Li, X.J. Wang, P.D. Hodgson, C.E. Wen, Titanium–Nickel Shape Memory Alloy Foams for Bone Tissue Engineering, Journal of the Mechanical Behavior of Biomedical Materials. 1 (2008) 269-273.

[72] G.İ. Nakaş, A.F. Dericioglu, Ş. Bor, Fatigue Behavior of TiNi Foams Processed by the Magnesium Space Holder Technique, Journal of the Mechanical Behavior of Biomedical Materials. 4 (2011) 2017-2023.

[73] G. Eggeler, E. Hornbogen, A. Yawny, A. Heckmann, M. Wagner, Structural and Functional Fatigue of NiTi Shape Memory Alloys, Materials Science and Engineering A. 378 (2004) 24-33.

[74] A.M. Figueiredo, P. Modenesi, V. Buono, Low-Cycle Fatigue Life of Superelastic NiTi Wires, Int. J. Fatigue. 31 (2009) 751-758.

[75] H. Tobushi, T. Hachisuka, S. Yamada, P. Lin, Rotating-Bending Fatigue of a TiNi Shape-Memory Alloy Wire, Mechanics of Materials. 26 (1997) 35-42.

[76] Y. Sugimura, A. Rabiei, A.G. Evans, A.M. Harte, N.A. Fleck, Compression Fatigue of a Cellular Al Alloy, Materials Science and Engineering: A. 269 (1999) 38-48.

[77] J. Zhou, W.O. Soboyejo, Compression–Compression Fatigue of Open Cell Aluminum Foams: Macro-/Micro- Mechanisms and the Effects of Heat Treatment, Materials Science and Engineering A. 369 (2004) 23-35.

[78] B. Zettl, H. Mayer, S.E. Stanzl-Tschegg, H.P. Degischer, Fatigue Properties of Aluminium Foams at High Numbers of Cycles, Materials Science and Engineering A. 292 (2000) 1-7.

[79] F. McCullough, The Stress–Life Fatigue Behaviour of Aluminium Alloy Foams, Fatigue & Fracture of Engineering Materials & Structures. 23 (2000) 199-208.

[80] L.J. Gibson, Mechanical Behavior of Metallic Foams, Annual Review of Materials Science. 30 (2000) 191-227.

[81] M.F. Ashby, A.G. Evans, N.A. Fleck, L.J. Gibson, J.W. Hutchinson, H.N.G. Wadley, Metal Foams: A Design Guide, Butterworth-Heinemann (2000).

[82] M. Barrabés, P. Sevilla, J.A. Planell, F.J. Gil, Mechanical Properties of Nickel–Titanium Foams for Reconstructive Orthopaedics, Materials Science and Engineering: C. 28 (2008) 23-27.

[83] P. Sevilla, C. Aparicio, J.A. Planell, F.J. Gil, Comparison of the Mechanical Properties between Tantalum and Nickel–Titanium Foams Implant Materials for Bone Ingrowth Applications, Journal of Alloys and Compounds. 439 (2007) 67-73.

[84] ASTM F2004 – 05, Standard Test Method for Transformation Temperature of Nickel-Titanium Alloys byThermal Analysis (2010).

[85] G.S. Firstov, R.G. Vitchev, H. Kumar, B. Blanpain, J. van Humbeeck, Surface Oxidation of NiTi Shape Memory Alloy, Biomaterials. 23 (2002) 4863-4871.

[86] C.H. Xu, X.Q. Ma, S.Q. Shi, C.H. Woo, Oxidation Behavior of TiNi Shape Memory Alloy at 450–750 °C, Materials Science and Engineering: A. 371 (2004) 45-50.

[87] M. Geetha, A.K. Singh, R. Asokamani, A.K. Gogia, Ti Based Biomaterials, the Ultimate Choice for Orthopaedic Implants – A Review, Progress in Materials Science. 54 (2009) 397-425.

[88] H. Lin, S. Wu, M. Yeh, Damping Characteristics of TiNi Shape Memory Alloys, Metallurgical and Materials Transactions A. 24 (1993) 2189-2194.

[89] A. Paradis, P. Terriault, V. Brailovski, Modeling of Residual Strain Accumulation of NiTi Shape Memory Alloys under Uniaxial Cyclic Loading, Computational Materials Science. 47 (2009) 373-383.

[90] X. Wang, B. Xu, Z. Yue, X. Tong, Fracture Behavior of the Compact Tension Specimens in NiTi Shape Memory Alloys, Materials Science and Engineering: A. 485 (2008) 14-19.

[91] H. Tobushi, Y. Shimeno, T. Hachisuka, K. Tanaka, Influence of Strain Rate on Superelastic Properties of TiNi Shape Memory Alloy, Mechanics of Materials. 30 (1998) 141-150.

[92] R. Lahoz, J.A. Puértolas, Training and Two-Way Shape Memory in NiTi Alloys: Influence on Thermal Parameters, Journal of Alloys and Compounds. 381 (2004) 130-136.

[93] Y. Sugimura, A. Rabiei, A.G. Evans, A.M. Harte, N.A. Fleck, Compression Fatigue of a Cellular Al Alloy, Materials Science and Engineering: A. 269 (1999) 38-48.

[94] G.E. Dieter, Mechanical Metllurgy, SI Metric ed., McGraw-Hili Book Co., London (1988).

[95] J.E. Shigley, Mechanical Engineering Design, Third ed., McGraw-Hill Kogusha Ltd., Tokyo, Japan (1977).

[96] J.S. Kim, J.H. Song, M.G. Changa, Y.J. Yuma, J-K. Leeb, Y.S. Kwon, The Effect of Heating Schedule and the Size of the Powder Compact on the Pore Structure, Mechanical and Fatigue Properties of Porous TiNi Produced by a Self-Propagating High-Temperature Synthesis Method, Journal of Ceramic Processing Research. 8 (2007) 70-73.

CIRRICULUM VITAE

PERSONAL INFORMATION

Surname, Name: Nakaş, Gül İpek
Nationality: Turkish (TC)
Date and Place of Birth: 23 May 1981, Ankara
Phone: +90 312 210 59 18
Fax: +90 312 210 25 18
email: inakas@metu.edu.tr

EXPERIENCE

Middle East Technical University, Ankara
May 2007 – August 2012
Research and Teaching Assistant

5th Main Maintenance Center, Turkish Land Forces Command, Ankara
Dec 2004 – May 2007
Chief of Non-Destructive Testing Department

EDUCATION

Middle East Technical University
Sept 2012
    Ph.D. in Metallurgical and Materials Engineering
    Thesis: The Processing of Porous Ni-Rich TiNi Alloys via Powder
    Metallurgy and Their Characterization

Middle East Technical University
Dec 2006
    M.Sc. in Metallurgical and Materials Engineering
    Thesis: Surface Modification of Resadiye Layered Silicates to be Used in
    Polymer Nanocomposites

Middle East Technical University
Jun 2003
    B.Sc. in Department of Metallurgical and Materials Engineering

LANGUAGES

English (Fluent), German (Beginner)

CERTIFICATIONS

- Liquid penetrant inspection method – Level II
- Magnetic particle inspection method – Level II
- Eddy-current inspection method – Level II
- Ultrasonic inspection method – Level II
- Radiographic (X-ray and gamma ray) inspection method – Level II